



University of  
**Southern  
Queensland**

**CHARACTERISING EXOPLANETS USING GROUND-BASED  
& SPACE-BASED FACILITIES**

A Thesis submitted by

**Natalia Lowson**

(B. Sc. Hons.)

For the award of

Doctor of Philosophy

2023

# ABSTRACT

EXOPLANETS ARE DIVERSE AND COMPLEX, with the components such as planetary formation, orbital dynamics, and atmospheric compositions being detectable through primary transiting events. This thesis embraces a multifaceted approach towards exoplanet characterisation, commencing with the atmospheric analysis of an ultra-hot Jupiter using archival data obtained from 1.5 m ground-based telescope. We recover strong detections of Fe I, Fe II, and Mg I while also modelling a peculiar H $\alpha$  transit. Subsequently we detect and confirm two new sub-Neptunes around an adolescent K-star using photometry from *TESS* and *CHEOPS*. Our analysis evaluates that inner planet resides in the sparsely populated radius gap, indicating that it could be undergoing significant atmospheric evaporation. Lastly, we present the preliminary target preparation for the upcoming *Twinkle Space Mission*, focusing on ephemerides refinement and monitoring for transit timing variations. Overall, this work contributes towards understanding exoplanets using a diverse range of analysis techniques from ground and space-based facilities.

# CERTIFICATION OF THESIS

I, Natalia Lowson, declare that the Ph. D. thesis entitled “Characterising Exoplanets Using Ground-based & Space-based Facilities” is not more than 100 000 words in length including quotes and exclusive of tables, figures, appendices, bibliography, references, and footnotes.

This thesis is the work of Natalia Lowson except where otherwise acknowledged, with the majority of the contribution to the papers presented as a thesis by publication undertaken by the student. The work is original and has not previously been submitted for any other award, except where acknowledged.

Date: October 20, 2023

Endorsed by:

A. Prof. Duncan J. Wright  
Principal Supervisor

Dr. George Zhou  
Associate Supervisor

Dr. Chelsea X. Huang  
Associate Supervisor

Student and supervisors' signatures of endorsement are held at UniSQ.

# STATEMENT OF CONTRIBUTION

This section details contributions by the various authors for each of the peer-reviewed or in preparation papers presented in this thesis by publication.

Chapter 3, Lawson et al. (2023b):

Author	Percent Contribution	Tasks Performed
Lawson, N.	80	Combined the observations and isolated the atmosphere signatures of the transit, performed the Bayesian statistical analysis, generated the H $\alpha$ light curve, came up and modelled the tail model concept, and wrote all drafts of the manuscript.
Zhou, G. Wright, D. J. Huang, C. X. Mendonça, J. M. Cabot, S. H. C. Pudmenzky, C. Wittenmyer, R. A. Latham, D. W. Bieryla, A. Esquerdo, G. A. Berlind, P Calkins, M. L.	} <sup>20</sup>	Provided the observations, the model spectra, the Rossiter-McLaughlin subtraction, the tail model code, assisted with coding, and suggested edits to the manuscript.

---

Chapter 4, Lawson et al. (2023a):

Author	Percent Contribution	Tasks Performed
Lowson, N.	80	Preformed the global fit, led the <i>CHEOPS</i> proposal, preformed the atmospheric simulations, modelled for TTVs, and wrote all drafts of the manuscript.
Zhou, G. Huang, C. X. Wright, D. J. Edwards, B. Nabbie, E. Venner, A. Quinn, S. N. Collins, K. A. Gillen, E. Battley, M. Triaud, A. Hellier, C. Seager, S. Winn, J. N. Jenkins, J. M. ...	} 20	First identified the HIP 113103 system of having two planet candidates, age and rotation estimations of HIP 113103, ground-based follow up observations, assistance with coding, and suggested edits to the manuscript.

Author	Percent Contribution	Tasks Performed
... Wohler, B. Shporer, A. Schwarz, R. P. Murgas, F. Pallé, E. Anderson, D. R. West, R. G. Wittenmyer, R. A. Bowler, B. P. Horner, J. Kane, S. R. Kielkopf, J. Plavchan, P. Zhang, H. Fairnington, T. Okumura, J. Mengel, M. W. Addison, B. C.	} 20	First identified the HIP 113103 system of having two planet candidates, age and rotation estimations of HIP 113103, ground-based follow up observations, assistance with coding, and suggested edits to the manuscript.

Chapter 5, Lawson et al. (prep):

Author	Percent Contribution	Tasks Performed
Lowson, N.	80	Obtained the <i>TESS</i> observations, performed the ephemerides refinement, TTV analysis, and wrote all drafts of the manuscript.
Wright, D. J. Huang, C. X. Zhou, G.	} 20	Provided the target list, assisted with coding, and suggested edits to the manuscript.

# ACKNOWLEDGMENTS

*But still try,  
for who knows what is possible*  
– Michael Faraday

THE WORK PRESENTED IN THIS THESIS was a labour of love that would not have been achieved without the support of my supervisory panel. To A. Prof. Duncan Wright, Dr. George Zhou, and Dr. Chelsea Huang, thank you for being on my supervisory panel throughout the course of my candidature. Your mentorship has had a profound impact on my professional career and I cannot thank you enough for the patience, guidance, and support you have provided. Although your specialisations do not fall under exoplanet atmosphere analysis, you took the time to learn about the field and provide project ideas that would intersect with your specialties. As a result, I have had the pleasure of learning how to characterise exoplanets through a number of techniques while also garnering experience into exoplanet atmosphere research. I know it can be a challenge to design a project that incorporates your interests with the aspirations of the student, and for that I will be forever grateful. To Prof. Brad Carter, Dr. Christa Pudmenzky, and Prof. Rob Wittenmyer, who resided as past mentors on my supervisory panel, thank you. Although brief, I appreciate the time you put aside to mentor me during my candidature. In particular, I want to thank Brad who as the Director of the department, accepted my admission into the UniSQ Centre for Astrophysics Ph.D. program to pursue this Candidature. I would also like to say a big thank you to my ex-

ternal collaborators who assisted me with these papers.

IN ADDITION TO RESEARCH MENTORING, there are a number of people that extend beyond this degree whose encouragement has contributed towards the success of this milestone. To my parents Andrew and Christine Lowson, thank you for supporting me from the moment I told you I wanted to pursue astronomy as a career, especially when it wasn't easy. To my sister Annabelle Lowson, thank you for being my number one fan who has always believed in my ability to achieve this, even when I didn't. To Dylan Prendergast, my now legally wed partner for life, thank you for your unconditional support throughout this long journey which has been too many years in the making. Although the path has not always been smooth, the sacrifices you've made alongside me has undoubtedly had the most profound impact towards this moment becoming a reality, and I will never forget it. To Dr. David Baker, Ms. Susan Scott, and Dr. Karen Humphrey, who were my teachers in the last two years of secondary college, thank you. In those vital educational years, you taught me that learning physics, maths, and chemistry is about hard work not inherent skill, and as a teenage girl looking to pursue a tertiary education in STEM, that meant everything. Lastly to my non-uni friends, my now in-law family, the UniSQ students, my external uni friends/colleagues, and my fur baby Fantasma, thank you, thank you, thank you! A particular shout out to The Coven (if you know, you know), Dr. Jake Clark, Dr. Alexis Heitzmann, and my work spouse Emma Nabbie.

THIS RESEARCH HAS BEEN DIRECTLY SUPPORTED by an Australian Government Research Training Program Scholarship and indirectly supported through the Australian Research Council Discovery Early Career Research Award programs DE210101893 and DE200101840. I also acknowledge Australia's Aboriginal and Torres Strait Islander peoples, who are the traditional custodians of the lands, the waterways, and the skies all across Australia. In particular, I pay my deepest respects to all Elders, ancestors, and descendants of the Giabal, Jarowair, and Yuggera nations, upon which the majority of the work for this Candidature was undertaken.

# TABLE OF CONTENTS

ABSTRACT .....	i
CERTIFICATION OF THESIS .....	i
STATEMENT OF CONTRIBUTION .....	ii
ACKNOWLEDGMENTS .....	vii
TABLE OF CONTENTS .....	ix
LIST OF FIGURES .....	xiii
LIST OF ABBREVIATIONS .....	xiv
CHAPTER 1: INTRODUCTION .....	1
1.1 Thesis Objectives and Research Questions .....	1
1.2 Thesis Overview .....	2
CHAPTER 2: LITERATURE REVIEW .....	4
2.1 Exploring Exoplanets Both Big and Small .....	4
2.1.1 Finding Planets in a Sea of Stars .....	6
2.1.2 Unveiling Their Mysteries via Atmosphere Characterisation .	10
2.2 The Telescopes That Carry the Field .....	13
2.2.1 Current Instrument Capabilities .....	13
2.2.2 Future Missions .....	18
CHAPTER 3: PAPER 1: MULTIEPOCH DETECTIONS OF THE EX- TENDED ATMOSPHERE AND TRANSMISSION SPECTRA OF KELT-9B WITH A 1.5M TELESCOPE. ....	19
3.1 Introduction .....	19
3.2 Links and Implications .....	37

CHAPTER 4: PAPER 2: TWO MINI-NEPTUNES TRANSITING THE ADOLESCENT K-STAR HIP 113103 CONFIRMED WITH <i>TESS</i> AND <i>CHEOPS</i> .....	38
4.1 Introduction .....	38
4.2 Links and Implications .....	57
CHAPTER 5: PAPER 3: TARGET PREPARATION FOR THE <i>TWINKLE</i> <i>SPACE MISSION</i> .....	58
5.1 Introduction .....	58
5.2 Links and Implications .....	71
CHAPTER 6: DISCUSSION AND CONCLUSIONS .....	72
6.1 Discussion .....	72
6.1.1 Paper-by-Paper Analysis .....	72
6.1.2 Synthesis, Contributions, and Significance .....	74
6.1.3 Future Directions .....	77
6.2 Conclusions .....	77
REFERENCES .....	79
APPENDIX A: OTHER PUBLISHED WORKS.....	91
A.1 Evidence for Low-Level Dynamical Excitation in Near-Resonant Exoplanet Systems.....	91
A.2 Characterising a World Within the Hot Neptune Desert: Transit Observations of LTT 9779 b with <i>HST</i> WFC3 .....	92
A.3 Invisible Women: Gender Representation in High School Science Courses Across Australia .....	93
A.4 A Mini-Neptune from <i>TESS</i> and <i>CHEOPS</i> Around the 120 Myr Old AB Dor member HIP 94235 .....	94
A.5 Twinkle: a small satellite spectroscopy mission for the next phase of exoplanet science .....	95
A.6 Around the hybrid conference world in the COVID-19 era .....	96
A.7 TOI-1842b: A Transiting Warm Saturn Undergoing Re-Inflation around an Evolving Subgiant .....	97

# LIST OF FIGURES

(EXCLUDING PUBLICATIONS INCLUDED IN CHAPTERS 3 TO 5)

2.1	Phase folded observations from HARPS illustrating the Doppler motion of a planet orbiting HD 85512. Image credit: (Pepe et al., 2011). . . . .	7
2.2	A schematic of a planet with radius $R_p$ completing a primary transit across its host star with radius $R_s$ , and the corresponding light curve caused by a change in flux, $\Delta F$ , illustrated underneath. This diagram also demonstrates some of the orbital parameters (in this case, the semi-major axis, $a$ , inclination, $i$ , and impact parameter, $b$ ) we can infer from observing a primary transit. Image credit: (Deeg & Alonso, 2018). . . . .	9
2.3	The Doppler motion of a simulated planet with carbon monoxide in its atmosphere as observed using the high resolution spectroscopy technique. The <b>top panel</b> illustrates the orbital position of the planet as it moves around its host star while the <b>bottom panel</b> displays the corresponding phase curve. Telluric features (black horizontal lines) from the Earth's atmosphere and the spectral features of the host star (grey horizontal lines) appear almost stationary in comparison to the planet. Image credit: (Birkby, 2018). . . . .	11

2.4	<p><b>Top left:</b> A cross-correlation function (CCF) of high-resolution spectra from a simulated hot Jupiter against a model template. The dark diagonal line is the atmosphere signal of the planet as a function of orbital phase over orbital velocity, and is displayed by stacking the exposures (represented by the horizontal lines). <b>Top right:</b> The CCF once the exposures have been shifted from the rest-frame of the host-star, to the rest frame of the planet. <b>Bottom:</b> A generated CCF map using the simulated data in the top panel. This shifts and sums the exposures for different <math>v_{sys}</math> and <math>K_p</math> values, with the largest signal-to-noise, <math>\sigma</math>, on the map representing the true <math>v_{sys}</math> and <math>K_p</math> values for this planet (as indicated by the plus symbol). Image credits: (Birkby, 2018). . . . .</p>	12
2.5	<p>A primary transit measures the light from the star travelling through the terminator region of a planet's atmosphere as it passes in front of the star (also known as the atmospheric annulus). A secondary transit (labelled here as an eclipse) measures light reflected off the surface of a planet just before it orbits behind the star. This spectrum presented illustrates the general measurement output from the transit. Image credit: (Deming &amp; Seager, 2017). . . . .</p>	14

2.6 Observations from different wavelengths reveal chemical and physical features of an atmosphere unique to that region. We can infer the optical features of an exoplanet atmosphere using ground-based telescopes, but the full ultraviolet and infrared wavelength regions can only be observed from space, where observations are free from interference caused by the Earth’s atmosphere. While observations in all regions are important, infrared is particularly valuable because it provides information on the deeper layers where cloud dynamics and molecules associated with biosignatures are detectable. The P-T profiles on the left represent a highly irradiated planet with thermal inversion (red), an irradiated planet without thermal inversion (cyan), and poorly irradiated planet (grey dashed). Image credit: (Madhusudhan, 2019). . . . . 16

## LIST OF ABBREVIATIONS

<i>CHEOPS</i> <i>CHaracterising ExOPlanets Satellite</i> . . . . .	i, iv, x, 3, 15, 38, 73, 94
<i>HST</i> <i>Hubble Space Telescope</i> . . . . .	x, 17, 39, 73, 92, 93
<i>HWO</i> <i>Habitable Worlds Observatory</i> . . . . .	18
<i>JWST</i> <i>James Webb Space Telescope</i> . . . . .	17, 39, 58, 73, 76
<i>PLATO</i> <i>PLANetary Transits and Oscillation of stars</i> . . . . .	18
<i>TESS</i> <i>Transit Exoplanet Survey Satellite</i> . . . . .	i, vi, x, 3, 5, 15, 18, 38, 58, 73, 74, 77, 93–95, 97
<b>CCF</b> <b>Cross-Correlation Function</b> . . . . .	xii, 10–12, 20, 72, 75
<b>CoRoT</b> <b>Convection, Rotation and planetary Transits</b> . . . . .	15
<b>CRIRES</b> <b>CRyogenic high-resolution InfraRed Echelle Spectrograph</b> . . . . .	17
<b>ELTs</b> <b>Extremely Large Telescopes</b> . . . . .	18
<b>ESO</b> <b>European Southern Observatory</b> . . . . .	16
<b>ESPRESSO</b> <b>Echelle SPectrograph for Rocky Exoplanets and Stable Spectroscopic Observations</b> . . . . .	14, 17, 77
<b>EUV</b> <b>Extreme Ultraviolet</b> . . . . .	5
<b>EXPRES</b> <b>EXtreme PREcision Spectrometer</b> . . . . .	14

<b>FLWO</b> Fred Lawrence Whipple Observatory . . . . .	72, 75
<b>GTC</b> Gran Telescopio Canarias . . . . .	16
<b>H<math>\alpha</math></b> Hydrogen- $\alpha$ . . . . .	i, 20, 72, 73, 75
<b>HARPS</b> High Accuracy Radial velocity Planet Searcher . . . . .	xi, 7, 14, 16
<b>HATNet</b> Hungarian Automated Telescope Network . . . . .	14
<b>HIRES</b> High Resolution Echelle Spectrometer . . . . .	14
<b>HRS</b> High-Resolution Spectroscopy . . . . .	3, 10–13, 15, 75
<b>KELT</b> Kilodegree Extremely Little Telescope . . . . .	15
<b>KPF</b> Keck Planet Finder . . . . .	14
<b>Ly<math>\alpha</math></b> Lyman- $\alpha$ . . . . .	20, 75
<b>NIR</b> Near Infrared . . . . .	17, 75
<b>PFS</b> Planet Finder Spectrograph . . . . .	92
<b>SOLES</b> Stellar Obliquities in Long-period Exoplanet Systems . . . . .	92
<b>STEM</b> Science, Technology, Engineering, and Maths . . . . .	viii, 94
<b>TOI</b> <i>TESS</i> Object of Interest . . . . .	x, 92, 94, 97
<b>TRES</b> Tillinghast Reflector Echelle Spectrograph . . . . .	19
<b>TTV</b> Transit Timing Variation . . . . .	iv, vi, 3, 8, 74, 76, 77
<b>UniSQ</b> University of Southern Queensland . . . . .	ii, vii, viii, 58, 59
<b>UV</b> Ultraviolet . . . . .	17, 75
<b>VLT</b> Very Large Telescope . . . . .	16, 17, 75, 77

<b>WASP</b> Wide Angle Search for Planets . . . . .	14
<b>WFC3</b> Wide Field Camera 3 . . . . .	x, 17, 92, 93

# CHAPTER 1: INTRODUCTION

After the discovery of 51 Peg b almost 30 years ago, exoplanet research has become one of the fastest growing fields in astronomy (Mayor & Queloz, 1995). Since then, there have been numerous detection and analysis techniques constructed for identifying exoplanets, with the majority revealing sub-classes outside of the Solar System analogues. Depending on the method used and the wavelength region observed, astronomers can reveal different physical and chemical parameters of exoplanets, particularly when it comes to atmosphere characterisation. For a more detailed discussion on how these detection and characterisation techniques are implemented on exoplanet observations, please refer to the literature review in Chapter 2.

## 1.1 THESIS OBJECTIVES AND RESEARCH QUESTIONS

The 2020 Decadal Survey on Astronomy and Astrophysics recommended a scientific priority and investment towards searching and detecting potentially habitable worlds (National Academies of Sciences & Medicine, 2023). Therefore, it is now vital more than ever before to understand how we conduct exoplanet research so that we can build upon current methodologies to properly prepare and execute this priority in the Decadal Survey. The work outlined in this Thesis therefore aims to answer the following science case:

## **1. How can we characterise exoplanets using facilities on the ground and in space?**

We achieve this science case through various techniques, including atmosphere analysis of an exoplanet using a metre-class ground-based facility, identifying a previously unknown multi-planet system using telescope satellites, and searching for unseen companions in known planetary systems. Each approach provides context on how we can use established exoplanet knowledge to contribute towards new discoveries within the field.

The methods used to achieve our science case primarily focus on interpreting primary transit observations of exoplanets (see Section 2.1.1 for a formal definition), which to date, is the most prolific detection method employed throughout the field. The technique also enables astronomers to extract both photometric and spectroscopic information, providing insight on important features such as planetary mass, radius, and atmospheric composition. While Direct Imaging is another important detection method for exoplanets (particularly towards atmosphere analysis), current instrumentation capabilities remain confined to the detection of young, large, internally hot planets. Our science case therefore will not be focusing on this sub-class, however we do acknowledge that this technique will eventually play a crucial role in the search for potentially habitable worlds once instrumentation improvements enable for the detection of small, cool planets.

### **1.2 THESIS OVERVIEW**

In Chapter 2, we delve into greater detail regarding the exoplanet detection and characterisation techniques that have been implemented throughout the field. We also introduce prominent telescopes that have been used to make

these discoveries, while highlighting future facilities capable of reshaping the field. In Chapter 3, we explore our science case by detecting and analysing the atmosphere of the ultra-hot Jupiter KELT-9b using the High-Resolution Spectroscopy (HRS) technique on a 1.5 m ground-based telescope. In Chapter 4, we present the first detection of two sub-Neptunes, HIP 113103 b and HIP 113103 c around the adolescent K-star HIP 113103 using the transit method via space-based facilities through the *Transiting Exoplanet Survey Satellite* (*TESS*, Ricker et al., 2015) and the *CHaracterising ExOPlanets Satellite* (*CHEOPS*, Benz et al., 2021) missions. In Chapter 5, we present the preliminary survey preparation for the *Twinkle Space Mission* (*Twinkle*, Tessenyi et al., 2017), evaluating the ephemerides for targets of interest while also monitoring for Transit Timing Variation (TTV) signals. Our discussion and conclusion of these three papers is then outlined in Chapter 6.

# CHAPTER 2: LITERATURE REVIEW

## 2.1 EXPLORING EXOPLANETS BOTH BIG AND SMALL

The fast-growing field of exoplanet research has shown that in addition to there being a plethora of planets within our Galaxy ( $\sim 5,500$  confirmed on the Exoplanet Archive<sup>1</sup> as of October 20 2023), the architecture of such systems can vary extensively from Solar System analogues. Of these architectures, hot Jupiters and sub-Neptunes particularly continue to garner notable importance within the community.

Hot Jupiters are defined as having a radii  $R_p \gtrsim 1 R_J$ , and orbit their host star on the order of days, or hours in the case of ultra-hot Jupiters (Fortney et al., 2008). Their discovery has prompted various studies on the formation pathways of gas giants during planet formation (e.g. Lin et al., 1996; Trilling et al., 1998; Wu & Murray, 2003; Mordasini et al., 2009; Boley et al., 2016; Dawson & Johnson, 2018; Fortney et al., 2021). Approximately 500 have been identified from the total 5,500 exoplanet sample, with the combination of a large radii and short orbital period ( $P \leq 10$  days) making them easily detectable. Their occurrence rate is estimated to be relatively low across all star types (e.g. an occurrence rate of  $0.43 \pm 0.05\%$  for FGK stars from Fressin et al. (2013) using *Kepler* observations and  $0.194 \pm 0.072\%$  for M dwarfs from

---

<sup>1</sup><https://exoplanetarchive.ipac.caltech.edu/>

Bryant et al. (2023) using *TESS*), thus providing a glimpse into the rare planet system extremes that exist (e.g. Johnson et al., 2010; Winn & Fabrycky, 2015; Petigura et al., 2018).

Sub-Neptunes are a sub-class of exoplanets intermediate of Earth and Neptune. They have a bimodal radius distribution between  $1.5 R_{\oplus} < R_p \leq 4.0 R_{\oplus}$ , with a decrease in planet numbers between  $1.7$  and  $2.0 R_{\oplus}$ . Conversely to hot Jupiters, super-Earths ( $1 R_{\oplus} < R_p \leq 1.5 R_{\oplus}$ ) and sub-Neptunes constitute  $\sim 50\%$  of planets situated around FGK stars hosting close-in planets, a result that was not initially predicted from planet formation theories (e.g. Howard et al., 2012; Fressin et al., 2013). One predominantly active area of research for sub-Neptunes is analysing planets situated in what is known as the Radius Gap. This is a region for close-in sub-Neptunes where there is a dearth of planets whose radii lie within  $1.5 R_{\oplus} < R_p \leq 2.0 R_{\oplus}$  (Fulton et al., 2017; Kunimoto & Matthews, 2020). Its existence is hypothesised to be a transition region between the H/He dominated primary atmospheres of mini-Neptunes to heavier-element secondary atmospheres we affiliate with the rocky planets in our Solar System, or in some cases, no atmosphere at all (e.g. Lopez et al., 2012; Ginzburg et al., 2018; Kite et al., 2020). Processes that could invoke atmosphere stripping include evaporation due to extreme ultraviolet (EUV) radiation from the host star and core-powered mass loss from the interior of the planet, with both scenarios occurring over different timescales of a planet's early evolution (with exact timescales being heavily dependent on various factors, such as planetary mass and stellar activity) (Owen & Jackson, 2012; Ginzburg et al., 2018).

### 2.1.1 FINDING PLANETS IN A SEA OF STARS

Before analysing sub-classes like hot-Jupiters and sub-Neptunes, their existence around respective star systems has to first be identified and confirmed. To date, there are five primary techniques used to identify exoplanets: Radial Velocity, Transits, Direct Imaging, Microlensing, and Astrometry. The radial velocity and transit techniques are historically the most successful at identifying planets, and will therefore be discussed in greater detail. For a review of the other techniques, see Fischer et al. (2014).

Radial velocity (also called the Doppler technique) identifies planet candidates by monitoring the motion of the host stars along our line-of-sight (e.g. Butler et al., 1999; Henry et al., 2000; Charbonneau et al., 2000). If a star has no companions, it will appear stationary when observed. In the scenario that it does have a companion (whether it be another star or a planet), it will orbit around a common centre of mass. If the unseen companion is orbiting the star within/near the line-of-sight to our telescope, the star will appear to move away from the telescope when the unseen companion is approaching inferior conjunction, and towards when approaching the superior conjunction (for more information, see Lovis & Fischer, 2010). This motion is detectable using high-resolution spectrographs, which observe the spectral features of the host star shifting from red to blue wavelengths in a periodic manner. If false positives (such as a binary companion, stellar rotation, or stellar variability indicators) can be ruled out as the source of the signal (see Figure 2.1), it is identified as a planet (e.g. Henry et al., 2000; Butler et al., 2004). Radial velocity can provide constraints on various physical and observational parameters of the planet, including its minimum mass,  $M_p \sin i$ , orbital period,  $P$ , the eccentricity,  $e$ , and argument of periapsis,  $\omega$ . The true

mass of the planet requires the orbital inclination,  $i$ , to be evaluated, which cannot be constrained from radial velocity observations. The radial velocity technique is currently restricted to ground-based observatories. The cost to construct high-resolution spectrographs with equivalent precision for space along with the observing limitations they introduce makes Doppler velocity space missions inefficient, especially when compared against the science output achievable for alternative planet detection techniques in space.

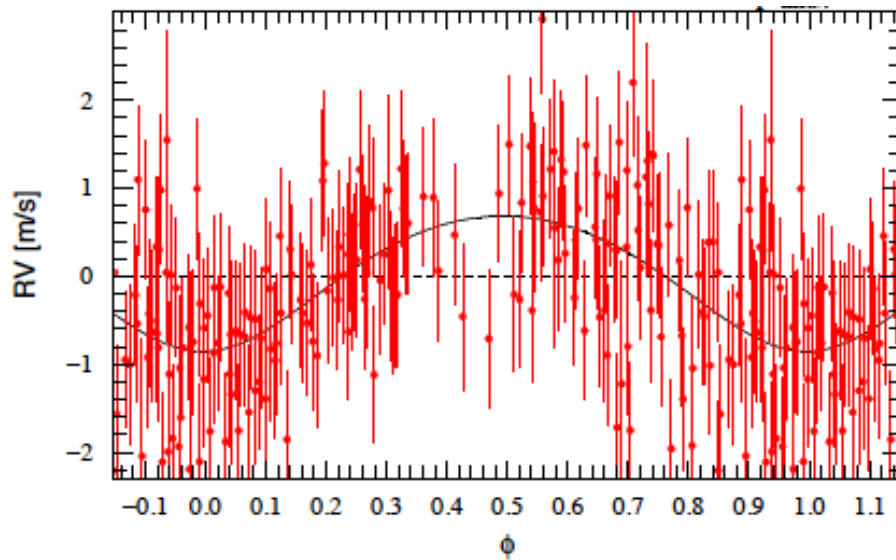


Figure 2.1: Phase folded observations from HARPS illustrating the Doppler motion of a planet orbiting HD 85512. Image credit: (Pepe et al., 2011).

The transit technique also monitors for changes in a host star along a telescope line-of-sight, but instead of detecting motion, the transit technique identifies periodic changes in brightness. When a planet crosses the inferior conjunction (commonly referred to as a primary transit), it causes a momentary decrease in the observed flux (e.g. Charbonneau et al., 2000). A smaller-scale event also occurs when the planet is about to cross the superior conjunction, which is commonly called the secondary transit (e.g. Charbonneau

et al., 2005; Alonso, 2018). A transit event can be due to a number of observables (see Bryant et al., 2023, for more information), but the instrumentation required to identify them is more readily accessible in comparison to high-resolution spectrographs (due to smaller instrumentation which makes it achievable on both ground and space-based observatories). Only after these false positives have been ruled out can the candidate then be identified as a planet (Seager & Mallén-Ornelas, 2003). Physical and observational parameter constraints from transiting planets include its radius,  $R_p$ , inclination,  $i$ , orbital semi-major axis,  $a$ , orbital eccentricity,  $e$ , argument of periapsis,  $\omega$ , and orbital period,  $P$ . Additionally, if the transit ingress and egress events occur at earlier/later times than originally observed, this can be indicative of unseen companions within the system (e.g. Holman & Murray, 2005). This additional transiting method of planet detection is called Transit Timing Variation (TTV), and can be understood in further detail via Agol & Fabrycky (2018).

Both the radial velocity and transit detection techniques are most sensitive to large planets residing close-in to their host star, making hot Jupiters a predominant sub-class to detect using these methods (e.g. Bouchy et al., 2004, 2005; Wilson et al., 2008; Hellier et al., 2009, 2011; Maxted et al., 2011; Johnson et al., 2012; Becker et al., 2015; Delrez et al., 2016). Although sub-Neptune and Earth-sized planets have been identified around FGK stars, efforts have been focused around M-dwarfs due to the larger  $R_p/R_\star$  ratio enabling for an easier detection (e.g. Gillon et al., 2017; Dittmann et al., 2017; Crossfield et al., 2019; Günther et al., 2019; Gan et al., 2022). When combining observations from both techniques, we can evaluate additional physical parameters such as the true mass,  $M_p$ , and density,  $\rho_p$ , of the planet (e.g. Bakos et al., 2007; Barge et al., 2008; Southworth et al., 2011; Deleuil et al., 2012;

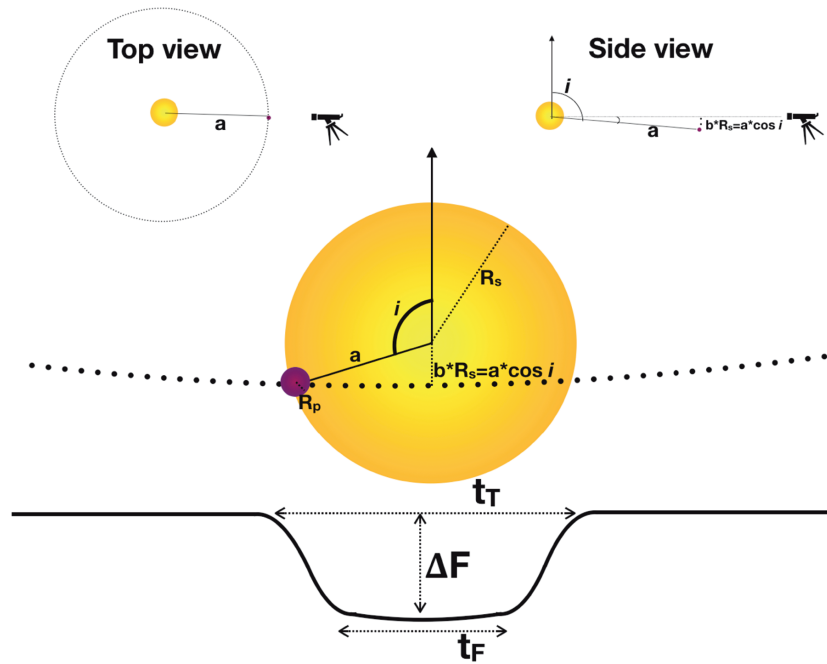


Figure 2.2: A schematic of a planet with radius  $R_p$  completing a primary transit across its host star with radius  $R_s$ , and the corresponding light curve caused by a change in flux,  $\Delta F$ , illustrated underneath. This diagram also demonstrates some of the orbital parameters (in this case, the semi-major axis,  $a$ , inclination,  $i$ , and impact parameter,  $b$ ) we can infer from observing a primary transit. Image credit: (Deeg & Alonso, 2018).

Díaz et al., 2020; Nava et al., 2022). It also important to monitor exoplanets and refine their orbital period,  $P$ , and time of conjunction,  $T_0$  (sometimes denoted as  $T_c$ ), so we can accurately predict future transit times for the planet. This process is known as Ephemerides refinement, and these values decay over time due to long-term physical effects within the planetary system (e.g. Rabus et al., 2009; Nascimbeni et al., 2011; Biddle et al., 2014; Maciejewski et al., 2016).

### 2.1.2 UNVEILING THEIR MYSTERIES VIA ATMOSPHERE CHARACTERIZATION

Once a planet system has been identified through the radial velocity or transit techniques, follow-up observations can be conducted to understand the planet in greater detail via their atmosphere analysis. Characterising an atmosphere can provide insight into the planet's formation history, weather, chemical composition, and the presence of biosignatures. High-Resolution Spectroscopy and Transit Spectroscopy are two of the most common ways to identify an atmosphere, which build upon the radial velocity and transit techniques outlined in Section 2.1.1. Other important techniques such as secondary eclipse spectroscopy, phase curves, eclipse mapping, and photometric analysis will not be discussed in this chapter, but the reader can refer to Deming et al. (2019) for a comprehensive overview.

High-resolution spectroscopy (HRS) is the atmosphere analysis component of the radial velocity technique. This technique uses a high-resolution spectrograph ( $R \geq 25,000$ ) to observe the difference in Doppler shift of spectral features from the orbital motion of the planet and its host star. As mentioned in Section 2.1.1, the spectral lines of the planet will move at a far greater velocity when compared to the host star, with the signal from the host star and telluric lines from the Earth's atmosphere, appearing almost stationary in comparison (Figure 2.3). Once the signal from the Earth's atmosphere and the host star has been removed, the remaining signal of the planet is compared against a template planetary spectrum containing expected prominent ions and molecules. The exposures are then shifted to be in the rest frame of the planet and summed to determine the strength of the signal (Figure 2.4, top panel). This process produces cross-correlation function (CCF) maps

which in addition to determining the strength of the signal, also evaluate the systemic velocity,  $v_{sys}$ , and the orbital velocity amplitude,  $K_p$  (also called the radial velocity semi-amplitude), with  $K_p$  being able to determine the true mass of the planet without the assistance of the transit technique (Figure 2.4, bottom panel) (e.g. Snellen et al., 2008; Brogi et al., 2012; Wyttenbach et al., 2015). The majority of the atmosphere detections via the HRS technique come from planets as they undergo a primary transit, however there have been notable atmosphere detections using HRS for planets that do not transit their host star (e.g. Redfield et al., 2008; Barman et al., 2011; Konopacky et al., 2013; Brogi et al., 2014). For primary transit HRS observations, a phenomenon known as the Rossiter-McLaughlin effect must be removed before evaluating the CCF maps (see Triaud (2018) for more information).

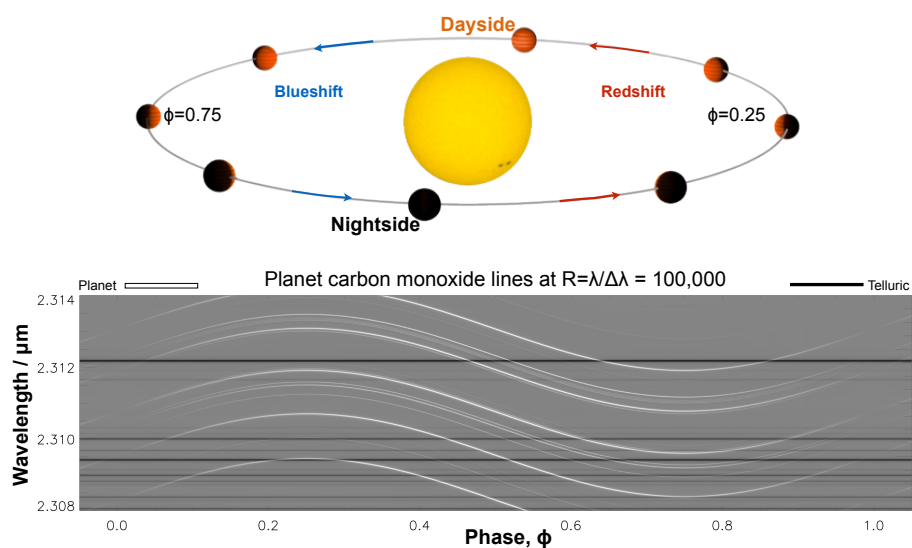


Figure 2.3: The Doppler motion of a simulated planet with carbon monoxide in its atmosphere as observed using the high resolution spectroscopy technique. The **top panel** illustrates the orbital position of the planet as it moves around its host star while the **bottom panel** displays the corresponding phase curve. Telluric features (black horizontal lines) from the Earth's atmosphere and the spectral features of the host star (grey horizontal lines) appear almost stationary in comparison to the planet. Image credit: (Birkby, 2018).

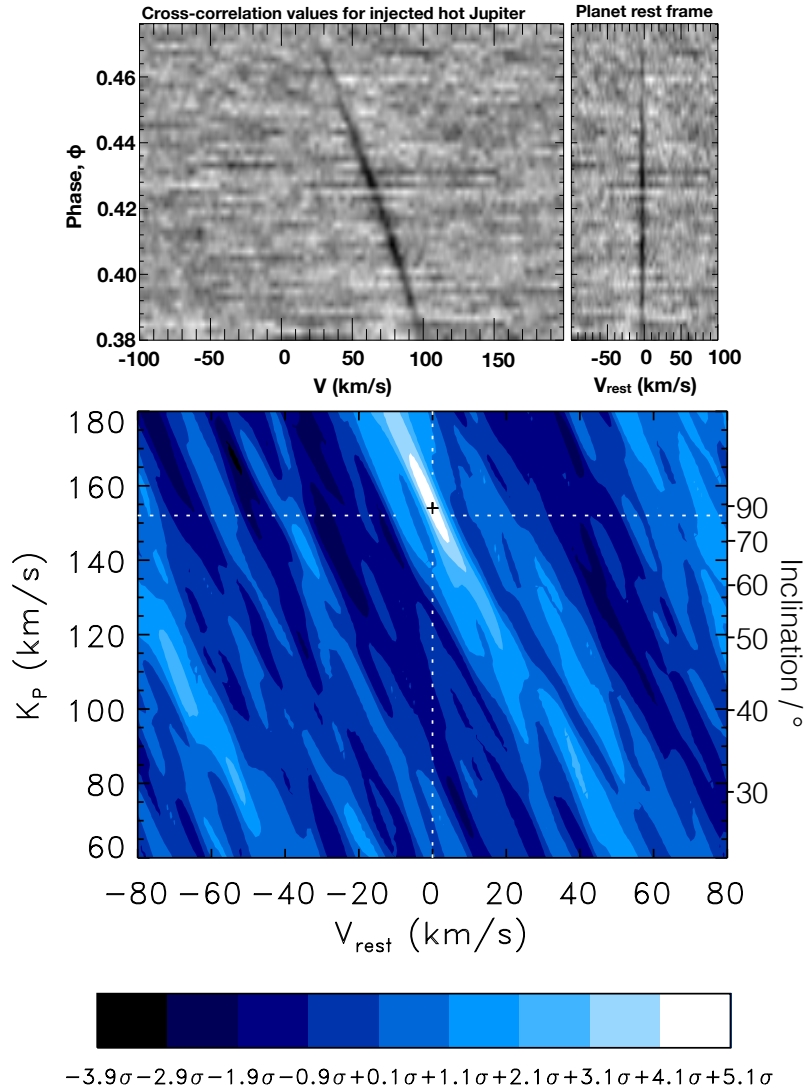


Figure 2.4: **Top left:** A cross-correlation function (CCF) of high-resolution spectra from a simulated hot Jupiter against a model template. The dark diagonal line is the atmosphere signal of the planet as a function of orbital phase over orbital velocity, and is displayed by stacking the exposures (represented by the horizontal lines). **Top right:** The CCF once the exposures have been shifted from the rest-frame of the host-star, to the rest frame of the planet. **Bottom:** A generated CCF map using the simulated data in the top panel. This shifts and sums the exposures for different  $v_{sys}$  and  $K_p$  values, with the largest signal-to-noise,  $\sigma$ , on the map representing the true  $v_{sys}$  and  $K_p$  values for this planet (as indicated by the plus symbol). Image credits: (Birkby, 2018).

Transmission spectroscopy is the low-resolution counterpart for HRS at-

mosphere detection and focuses on atmosphere signals during a primary transit. This technique builds upon the transit technique outlined in Section 2.1.1, but instead of observing the photometric change in flux over a single band during a primary transit, it observes the changes over a variety of spectral wavelengths. When a planet is not transiting, only the spectral signal from the host star (also known as a baseline signal) is observed, however as the planet transits, we obtain a combined spectral signal of the host star and planet. Using the baseline to remove the stellar signal, we can uncover the transmission spectral signal contribution from the planet. This arises from the host star emitting light through the atmospheric annulus of the planet, unveiling its day-to-night terminator atmosphere region (as illustrated in Figure 2.5).

Similar to the HRS technique, the transmission spectrum is compared against a template planetary spectrum in a technique known as atmospheric retrieval to identify molecular absorption and constrain additional features of the atmosphere including clouds, haze, temperature profiles, Rayleigh scattering, and Mie scattering. Transmission spectroscopy is primarily observed using space-based facilities, as the low resolution spectra combined with the spectral signals from Earth's atmosphere make it challenging to extract from ground-based observatories.

## 2.2 THE TELESCOPES THAT CARRY THE FIELD

### 2.2.1 CURRENT INSTRUMENT CAPABILITIES

Exoplanet detections from the radial velocity and transit methods have been made with several ground and space-based telescopes, however efficiency coincided with detection-dedicated facilities. Notable ground-based radial ve-

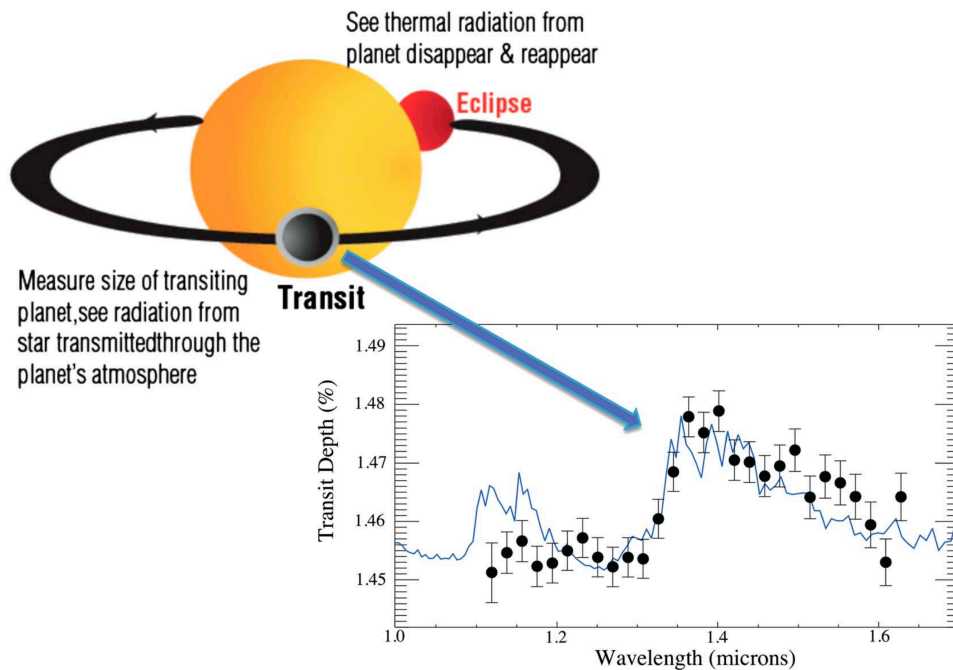


Figure 2.5: A primary transit measures the light from the star travelling through the terminator region of a planet's atmosphere as it passes in front of the star (also known as the atmospheric annulus). A secondary transit (labelled here as an eclipse) measures light reflected off the surface of a planet just before it orbits behind the star. This spectrum presented illustrates the general measurement output from the transit. Image credit: (Deming & Seager, 2017).

velocity facilities that have either had a large historical influence or currently lead the field include CORALIE (Queloz et al., 2000), the Echelle Spectrograph for Rocky Exoplanets and Stable Spectroscopic Observations (ESPRESSO, Pepe et al., 2021), the High Accuracy Radial velocity Planet Searcher (HARPS, Pepe et al., 2002), the High Resolution Echelle Spectrometer (HIRES, Vogt et al., 1994), the NEID Spectrograph (Schwab et al., 2016), the Keck Planet Finder (KPF, Gibson et al., 2016), and the EXtreme PREcision Spectrometer (EXPRES, Zhao et al., 2022). For the transit method, ground-based facilities such as the Hungarian Automated Telescope Network (HATNet, Bakos, 2018), the Wide Angle Search for Planets (WASP, Pollacco et al., 2006), and

the Kilodegree Extremely Little Telescope (KELT, Pepper et al., 2007) contributed a number of transit detections, however the majority of transiting exoplanets have been identified using space-based facilities such as the *Convection, Rotation and planetary Transits (CoRoT)*, (Deleuil & Fridlund, 2018) telescope, the *Kepler Space Telescope* (which led the *Kepler* and *K2* missions, Borucki et al., 2010; Howell et al., 2014) and *TESS*. *CHEOPS* has also been instrumental at providing high-precision follow up photometry for transiting exoplanetary systems, primarily focusing on the radius refinement of super-Earths and sub-Neptunes around bright stars.

As outlined in 2.1.2, obtaining a spectrum to analyse the atmosphere of an exoplanet is a challenging process, but astronomers have made remarkable progress with our current instrument capabilities. While it is important that techniques such as HRS and transmission spectroscopy can recover the atmospheric signal from a planet, what we learn from these signals is dependent on what bandpass we observe in. Figure 2.6 illustrates that looking at an atmosphere in different regions of the electromagnetic spectrum will uncover different physical and chemical processes. Therefore, while a larger telescope aperture could be capable of detecting smaller Earth-sized exoplanets, information remains limited depending on the wavelength region available on a given spectrograph. Ground-based exoplanet facilities remain limited to optical, and some regions of the infrared, as all other regions of the electromagnetic spectrum become scattered by the Earth's atmosphere. Therefore, with respect to atmospheric composition, ground-based telescopes are largely limited to only detecting some atomic and molecular species. The full chemical composition of an exoplanet's atmosphere can be best understood by observing from ultraviolet (where most atomic species absorb) through to infrared

(where most molecular species absorb).

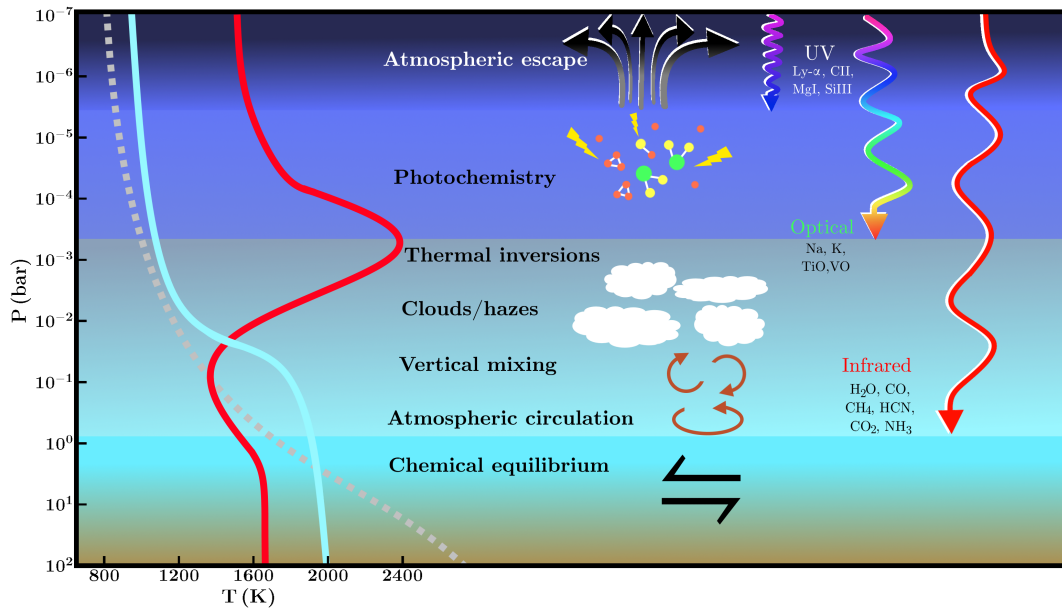


Figure 2.6: Observations from different wavelengths reveal chemical and physical features of an atmosphere unique to that region. We can infer the optical features of an exoplanet atmosphere using ground-based telescopes, but the full ultraviolet and infrared wavelength regions can only be observed from space, where observations are free from interference caused by the Earth’s atmosphere. While observations in all regions are important, infrared is particularly valuable because it provides information on the deeper layers where cloud dynamics and molecules associated with biosignatures are detectable. The P-T profiles on the left represent a highly irradiated planet with thermal inversion (red), an irradiated planet without thermal inversion (cyan), and poorly irradiated planet (grey dashed). Image credit: (Madhusudhan, 2019).

Large ground-based telescopes such as the Very Large Telescope (VLT, Wiedemann, 1996) and the Gran Telescopio Canarias (GTC, Alvarez et al., 1998) have provided both low-resolution and high-resolution transit spectroscopy observations, in particular identifying Na, K, TiO and He in exoplanet atmospheres (Sedaghati et al., 2017; Nikolov et al., 2018). Additionally, high-resolution Doppler spectroscopy using HARPS on the ESO 3.6 m telescope,

and instruments on the VLT such as ESPRESSO and the Cryogenic high-resolution InfraRed Echelle Spectrograph (CRIRES, Wiedemann, 1998), have provided strong detections of H<sub>2</sub>O, CO, TiO and HCN in several hot Jupiters (Brogi et al., 2017). ESPRESSO is currently the most precise spectrograph for ground-based atmosphere characterisation, successfully retrieving spectral signals from smaller planets such as hot Neptunes.

When observing atmospheres from space, the 0.85 m *Spitzer* (3.6 – 160  $\mu$ m) telescope contributed to infrared analysis immensely until its decommission in January 2020, despite its initial science case not being constructed for transiting exoplanet research (Deming & Knutson, 2020). Most contributions have come from the 2.4 m *Hubble Space Telescope* (*HST*, van den Bergh, 1985), which can observe transiting atmospheres from the ultra-violet through to the near-infrared using the UVIS (200 – 1000 nm) and NIR (850 – 1700 nm) channels on its Wide Field Camera 3 (WFC3, Cheng et al., 2000) instrument. *HST* is responsible for numerous atmosphere discoveries, including the first exoplanet atmosphere detection and the first evaporating atmosphere detection using the UV absorption line of Lyman- $\alpha$  (Vidal-Madjar et al., 2003). Since the 2021 launch of the *James Webb Space Telescope* (*JWST*, Gardner et al., 2006), exoplanet atmosphere analysis from space has experienced an evolutionary leap (e.g. Greene et al., 2023; Kempton et al., 2023; Lustig-Yaeger et al., 2023; Madhusudhan et al., 2023; Tsai et al., 2023; Zieba et al., 2023). The various *JWST* optical to infrared instruments suitable for atmosphere analysis combined with its 6.5 m aperture is resolving exoplanets to a high sensitivity previously unattainable with *HST*.

### 2.2.2 FUTURE MISSIONS

While the next-generation of Extremely Large Telescopes (ELTs) set to begin operation as early as the 2030s will transform ground-based exoplanet characterisation, atmosphere analysis will continue to predominantly come from space-based facilities. Planned missions such as the *PLANetary Transits and Oscillation of stars (PLATO)*, Catala & Plato Team, 2006) and *Ariel* (which was initially known as the *Atmospheric Remote-sensing Infrared Exoplanet Large-survey*, Tinetti et al., 2016) will insure dedicated exoplanet detection and characterisation. *PLATO*, which is planned to launch in 2026, will specialise in the detection of Earth-sized planets in habitable zone (HZ) regions, while *Ariel*, which is planned to launch in 2029, will conduct a population survey on the atmospheres of exoplanets discovered through from the *Kepler*, *K2*, and *TESS* missions. Prior to these large surveys, the *Twinkle Space Mission* will be the precursor to *Ariel*, which is expected to launch in 2025. *Twinkle* is a low earth orbit 0.45 m optical to infrared (0.5 – 4.5  $\mu$ m) telescope that will provide on-demand observations of a wide variety of exosolar and Solar System targets that are inaccessible using other space telescopes or accessible only to already oversubscribed observatories. The University of Southern Queensland is founding member of the *Twinkle Space Mission*, and is providing ground-based preparation on selected targets that will be observed in the exosolar component of the survey. Beyond 2030, the *Habitable Worlds Observatory (HWO)*, Gaudi et al., 2020) space mission will lead the next era of exoplanet characterisation.

# CHAPTER 3: PAPER 1: MULTIEPOCH DETECTIONS OF THE EXTENDED ATMOSPHERE AND TRANSMISSION SPECTRA OF KELT-9B WITH A 1.5 M TELESCOPE.

## 3.1 INTRODUCTION

THE CHARACTERISATION OF EXOPLANET ATMOSPHERES enables us to understand exoplanets in greater detail, with its physical chemistry providing insight on current and past evolution. The ultra-hot Jupiter KELT-9b is a particularly unique case study. As the hottest exoplanet discovered on record, it demonstrates the limits of what an exoplanet can be. In this study, we pushed the boundaries on how atmosphere characterisation could be conducted with high resolution spectroscopy, by presenting atmosphere detections using a 1.5 m telescope. We analysed archival transmission spectra of the ultra-hot Jupiter KELT-9b ( $P = 1.4811235$  days and  $T_{eq} = 4050$  K) over two primary transit epochs using the Tillinghast Reflector Echelle Spectrograph (TRES),

a high resolution spectrograph ( $R = 44,000$ ) on the 1.5 m reflector at the Fred Lawrence Whipple Observatory.

THE CCF MAPPING REVEALED atomic detections of Fe I, Fe II, Mg I, and H $\alpha$  at a significance of  $6\sigma$ ,  $6\sigma$ ,  $4\sigma$ , and  $4\sigma$  respectively. In addition to our atomic detections and mass calculations, we also modelled the transit light curve of the H $\alpha$  signal, which presents an unusual ‘W’-shape across each transit, deviating from the expected box shape of a standard white light transit. Given H $\alpha$  is an associated secondary tracer of atmosphere evaporation (with Ly $\alpha$  and He I 10830 being notable examples of primary tracers), we presented a simple ‘cometary tail’ model which replicates the temporal variability of the observed transit shape over both epochs. In order for H $\alpha$  to extend beyond the exosphere, the planet atmosphere must maintain a large population of neutral hydrogen at the metastable  $n = 2$  state. Since extended atmospheres are dominated by ionised hydrogen (which provides little absorption within the H $\alpha$  line region) it is unlikely that our model is a physical representation of the mechanisms we observe. Therefore, we propose this model be used as a way to monitor temporal variability observed amongst epoch observations of ‘W’-shaped light curves.



# Multiepoch Detections of the Extended Atmosphere and Transmission Spectra of KELT-9b with a 1.5 m Telescope

Nataliea Lowson<sup>1</sup>, George Zhou<sup>1</sup>, Duncan J. Wright<sup>1</sup>, Chelsea X. Huang<sup>1</sup>, João M. Mendonça<sup>2</sup>, Samuel H. C. Cabot<sup>3</sup>, Christa Pudmenzky<sup>4</sup>, Robert A. Wittenmyer<sup>5</sup>, David W. Latham<sup>5</sup>, Allyson Bieryla<sup>5</sup>, Gilbert A. Esquerdo<sup>5</sup>, Perry Berlind<sup>5</sup>, and Michael L. Calkins<sup>5</sup>

<sup>1</sup> Centre for Astrophysics, University of Southern Queensland, 499-565 West Street, Toowoomba, QLD 4350, Australia; [nataliea.lowson@usq.edu.au](mailto:nataliea.lowson@usq.edu.au)

<sup>2</sup> National Space Institute, Technical University of Denmark, Elektrovej, DK-2800 Kgs. Lyngby, Denmark

<sup>3</sup> Yale University, 52 Hillhouse Avenue, New Haven, CT 06511, USA

<sup>4</sup> Centre for Applied Climate Sciences, University of Southern Queensland, 499-565 West Street, Toowoomba, QLD 4350, Australia

<sup>5</sup> Center for Astrophysics | Harvard & Smithsonian, 60 Garden St., Cambridge, MA 02138, USA

Received 2022 May 23; revised 2022 December 16; accepted 2022 December 16; published 2023 February 13

## Abstract

Irradiated Jovian atmospheres are complex and dynamic and can undergo temporal variations due to the close proximity of their parent stars. Of the Jovian planets that have been cataloged to date, KELT-9b is the hottest gas giant known, with an equilibrium temperature of 4050 K. We probe the temporal variability of transmission spectroscopic signatures from KELT-9b via a set of archival multiyear ground-based transit observations, performed with the TRES facility on the 1.5 m reflector at the Fred Lawrence Whipple Observatory. Our observations confirm past detections of Fe I, Fe II, and Mg I over multiple epochs, in addition to excess absorption at H $\alpha$ , which is an indicator for ongoing mass loss. From our multiyear data set, the H $\alpha$  light curve consistently deviates from a standard transit and follows a “W” shape that is deeper near ingress and egress and shallower midtransit. To search for and quantify any seasonal variations that may be present, we parameterize a “cometary tail” model to fit the H $\alpha$  transit. We find no detectable variations between the different observed epochs. Though a “cometary tail” describes the H $\alpha$  flux variations well, we note that such a scenario requires a high density of neutral hydrogen in the  $n = 2$  excited state far beyond the planetary atmosphere. Other scenarios, such as center-to-limb variations larger than that expected from 1D atmosphere models, may also contribute to the observed H $\alpha$  transit shape. These multipepoch observations highlight the capabilities of small telescopes to provide temporal monitoring of the dynamics of exoplanet atmospheres.

*Unified Astronomy Thesaurus concepts:* Exoplanets (498); Hot Jupiters (753); Exoplanet atmospheric composition (2021); Exoplanet atmospheric variability (2020); Exoplanet evolution (491)

## 1. Introduction

Deciphering an exoplanet atmosphere signal from that of its host star has historically been a difficult endeavor, initially being restricted to either space-based telescopes (e.g., HST and Spitzer) or large-aperture ( $\geq 8$  m) ground-based telescopes (see reviews by Seager & Deming 2010; Madhusudhan 2019). Thanks to advances in our techniques for probing exoplanet atmospheres and the efforts by ground- and space-based surveys to identify new transiting planets suitable for characterization (Knutson et al. 2009; Stevenson et al. 2014; Birkby 2018), we can now demonstrate that meter-class facilities are also capable of characterizing exoplanet atmospheres, as presented in this publication.

Many exoplanet atmosphere observations focus around the primary transit, where we analyze light from the host star that travels through the day–night terminator region of the planet as it transits in front of its host star. One of the observational techniques that captures these transits is known as the high-resolution spectroscopy technique. This involves using a high-resolution spectrograph,  $R \geq 25,000$ , to detect the Doppler shift of the planet as it travels along its orbit over the course of the transit. For close-in planets, this is achievable owing to the

motion of the planet moving at a larger velocity in comparison to the simultaneously observed stellar spectra of the host star, varying as per the barycentric velocity shift and the near-stationary telluric absorption features (see review by Birkby 2018). Chemical composition is determined by comparing the detected spectral lines to high-resolution spectra generated from modeling codes with the same physical parameters (such as temperature) that are calculated for the observed planet. In addition to chemical composition, this technique can decipher additional physical parameters of an exoplanet, including true planetary mass (e.g., de Kok et al. 2013), temperature profiles (e.g., Snellen et al. 2010), the presence of clouds (when optical spectra are used in conjunction with low-resolution near-infrared transmission spectra; e.g., Žák et al. 2019; Allart et al. 2020), day-to-night winds (e.g., Snellen et al. 2010; Louden & Wheatley 2015), and the rotation period of the planet (e.g., Brogi et al. 2016).

Analyzing the chemical composition of an exoplanet atmosphere through high-resolution spectroscopy not only tells us what atoms are in the atmosphere but also can reveal which ones are escaping it. For exoplanets that reside close to their host stars, the exposure to extreme levels of irradiation enables active atmospheric evaporation from the planet (e.g., Lammer et al. 2003; Yelle 2004; García Muñoz 2007; Murray-Clay et al. 2009; Owen & Jackson 2012; King & Wheatley 2021; Kubyshkina 2022). Mass loss through evaporation of a primordial atmosphere is one of the dominant evolutionary

 Original content from this work may be used under the terms of the [Creative Commons Attribution 4.0 licence](https://creativecommons.org/licenses/by/4.0/). Any further distribution of this work must maintain attribution to the author(s) and the title of the work, journal citation and DOI.

drivers for atmospheres, often occurring within the first billion years after formation (e.g., Owen 2019; Howe et al. 2020; Bean et al. 2021).

Atmospheric escape can be identified via absorption lines by atoms with a planetary radius beyond the Roche limit (a region where the gravity of the planet equals that of the parent star). Absorption by species close to the Roche limit, and at high velocities with respect to the planet, can also be tracers of ongoing escape. The most successful observational tracer for atmosphere evaporation involves searching for excess Ly $\alpha$  (e.g., Vidal-Madjar et al. 2003; Lecavelier Des Etangs et al. 2010; Ehrenreich et al. 2015; Bourrier et al. 2018; Odert et al. 2020), while He I  $\lambda$ 10830 has also been identified as invaluable (e.g., Allart et al. 2018; Mansfield et al. 2018; Salz et al. 2018; Spake et al. 2018; Alonso-Floriano et al. 2019; Kirk et al. 2020; Ninan et al. 2020; Kirk et al. 2022). However, with the Ly $\alpha$  absorption line occurring in UV (1215.67 Å) and He I  $\lambda$ 10830 occurring in the near-infrared, detection of these species is mostly limited to space-based telescopes or large ground-based telescopes. Fortunately, the optical transmission absorption line of H $\alpha$  has also been identified as a potential indirect probe for ongoing atmosphere evaporation, enabling this process to be observed with ground-based high-resolution spectroscopic facilities (e.g., Cauley et al. 2017; Casasayas-Barris et al. 2018; Cabot et al. 2020; Yan et al. 2021; Czesla et al. 2022). Observing absorption lines alluding to planetary mass loss will help resolve exoplanet evolutionary enigmas, such as the hot Neptune “desert” and the radius valley, both of which have been proposed to be the product of atmosphere evaporation during the late stages of planet formation (e.g., Beaugé & Nesvorný 2013; Lundkvist et al. 2016; Mazeh et al. 2016; Fulton et al. 2017; Fulton & Petigura 2018; Van Eylen et al. 2018; Venturini et al. 2020; Rogers & Owen 2021).

One of the notable exoplanets where ongoing detections of H $\alpha$  have been observed in its upper atmosphere is the ultrahot Jupiter KELT-9b (Yan & Henning 2018). With  $T_{\text{eq}} = 4050 \pm 180$  K, KELT-9b is the hottest Jovian exoplanet discovered thus far, having a dayside temperature ( $\sim 4900$  K) equivalent to the photospheric temperature of K stars (Gaudi et al. 2017; Hooton et al. 2018). A number of chemical elements have been detected in both primary and secondary transit observations of KELT-9b (Cauley et al. 2019; Hoeijmakers et al. 2019; Yan et al. 2019; Turner et al. 2020; Pino et al. 2020; Changeat & Edwards 2021), including Fe II, which had never been observed in an exoplanet atmosphere prior to KELT-9b (Hoeijmakers et al. 2018; Bello-Arufe et al. 2022). Detections of excess H $\alpha$  absorption in the atmosphere of KELT-9b have been repeatedly linked to atmosphere evaporation (Yan & Henning 2018; Cauley et al. 2019; Wyttenbach et al. 2020), which has been proposed to be the product of thermal dissociation and recombination of H $_2$  in the upper atmosphere of the planet in the presence of strong UV irradiation (Kitzmann et al. 2018; Yan & Henning 2018; García Muñoz & Schneider 2019; Mansfield et al. 2020). Cauley et al. (2019) pointed out significant substructure in the absorption time series of metal and Balmer lines for their 2019 transit using the PEPsi instrument on the Large Binocular Telescope. They especially noted the blueshifted absorption extending to  $\sim 100$  km s $^{-1}$  in the line profile during egress, and they hypothesized it to be due to a wind-like geometry where material is being accelerated away from the planet toward the observer. They proposed that this wind is due to a temporal

spike in the planet’s mass-loss rate caused by a stellar flare. Such phenomena were not present in the two H $\alpha$  absorption time series observed in Yan & Henning (2018) using CARMENES; however, the signal-to-noise ratio (S/N) in their data set prohibited them from resolving and measuring velocity centroids of individual transmission spectra.

In this paper, we use two epochs of archival observations of KELT-9b taken on a 1.5 m telescope to characterize its atmosphere. We also debut a geometric model to monitor temporal variability between epochs, which is derived using the “W” profile displayed in the H $\alpha$  transit photometry. In Section 2, we outline how the observations were taken and our method for telluric subtraction. Section 3 details the extraction of the H $\alpha$  absorption, construction of our geometric model, and comparison of it against our photometric data sets. Section 4 presents our additional detections of metals and our mass estimations for KELT-9 and KELT-9b, followed by our discussion and conclusion in Sections 5 and 6, respectively.

## 2. Observations and Telluric Subtraction

We used archival observations available for KELT-9 from the Tillinghast Reflector Echelle Spectrograph (TRES) on the 1.5 m reflector at the Fred Lawrence Whipple Observatory (FLWO; Mount Hopkins, Arizona, USA). TRES is a fiber-fed echelle with a resolving power of  $\lambda/\Delta\lambda \equiv R = 44,000$ , covering the spectral range of 3850–9100 Å over 51 echelle orders (Szentgyorgyi & Furész 2007).

These archival observations are the same data set presented in the KELT-9b discovery paper (Gaudi et al. 2017), with a total of 75 spectra being observed over three separate transit epochs (UT: 2014 November 15, 2015 November 6, 2016 June 12). Observations on 2014 November 15 were obtained at an exposure time of 720 s, achieving S/N  $\approx 300$  per resolution element over the Mg *b* lines. Observations on 2015 November 06 had an exposure time of 540 s, achieving S/N  $\approx 140$ . Observations on 2016 June 12 yielded far lower S/N spectra and were subsequently not used in the remainder of this analysis.

Ground-based observations are always contaminated by telluric absorption through Earth’s atmosphere. These absorbing species within Earth’s atmosphere (H $_2$ O and Na in particular) interact with the incoming light from the host star prior to reaching our detectors. These features contaminate the minute absorption signatures we are attempting to retrieve. We follow the general techniques adopted by similar previous analyses (e.g., Cabot et al. 2019) and remove these telluric features via a set of synthetic models. In this paper, we make use of the `telFit` module (Gullikson et al. 2014) to model the atmosphere via the Line-by-Line Radiative Transfer Model (Clough et al. 1992).

To fit the observed telluric lines, we produced a set of  $\sim 10,000$  models to sufficiently explore a parameter space varying for humidity, oxygen mixing ratio, zenith angle, and instrument resolution. This library is interpolated using a gradient boosting regressor via the `scikit-learn` package (Grisel et al. 2021). The best-fitting telluric model is identified via a least-squares fit between the observations and the telluric library. Despite the telluric corrections, we still discard spectral orders severely influenced by the telluric O $_2$  absorption bands at 7534–7682 Å and 8922–9097 Å. A portion of the telluric-corrected spectrum is presented in Figure 1.

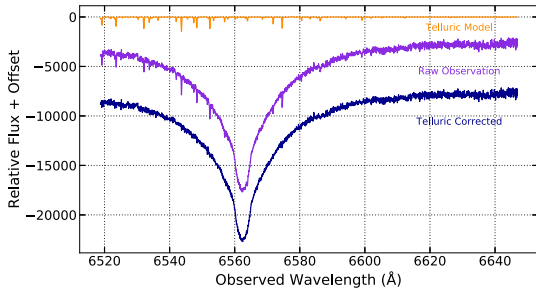


**Figure 1.** Example telluric correction over the  $H\alpha$  wavelengths for the 2014 KELT-9b observations. We generate a library of synthetic telluric spectra using the `telfit` implementation of the Line-by-Line Radiative Transfer Model. The observations are then matched against the interpolated library. The resulting corrected spectrum is shown at the bottom.

### 3. An Extended $H\alpha$ Atmosphere

Highly irradiated gas giants are expected to undergo atmospheric escape throughout their lifetimes (see review by Owen 2019). Excess absorption in Ly $\alpha$  has been a predominant tracer for atmosphere escape (e.g., Vidal-Madjar et al. 2003), with “photoevaporation” and core-powered mass loss being the widely accepted models used to explain this process (Owen et al. 2023). Likewise for optical band observations, excess absorption of  $H\alpha$  is being increasingly reported near the Roche radius for numerous highly irradiated hot Jupiters (Casasayas-Barris et al. 2019; Chen et al. 2020; Cauley et al. 2021; Yan et al. 2021; Czesla et al. 2022), including KELT-9b (Yan & Henning 2018; Cauley et al. 2019; Wyttenbach et al. 2020). While the detection of  $H\alpha$  in KELT-9b has been interpreted as a signature of active mass loss by some (e.g., Yan & Henning 2018; García Muñoz & Schneider 2019), it has been contested by others (e.g., Turner et al. 2020; Fossati et al. 2020).

PEPSI observations in 2018 by Cauley et al. (2019) showed that KELT-9b exhibits a strong  $H\alpha$  absorption in transit, with a “W”-shaped transit light curve. We describe below our efforts to recover and model this effect in our observations from 2014 and 2015.

Section 3.1 presents an overview on the removal of the stellar spectrum, the white-light Doppler tomographic planetary transit, and recovery of the planetary  $H\alpha$  excess signal through the transit event. Section 3.2 presents a toy transit model to describe the  $H\alpha$  transit light curves from our observations.

#### 3.1. $H\alpha$ Transit Light Curves

In this section, we detail the analysis of the  $H\alpha$  excess absorption of KELT-9b from our TRES observations. We detected the excess  $H\alpha$  absorption of KELT-9b at the expected orbital velocity of the planet during both TRES transit observations. The  $H\alpha$  transit light curve, which maps the temporal variation of the  $H\alpha$  excess through the transit, does not follow the shape expected for a standard white-light transit. We discuss our interpretation of this signal and offer a simple “cometary tail” model that replicates the observed transit shape.

We first normalize the spectral region within  $200 \text{ km s}^{-1}$  of the  $6562.8 \text{ \AA}$   $H\alpha$  absorption feature for each TRES observation. The planetary and stellar signals dramatically differ in their velocity variation over the course of the transit, allowing us to differentiate between the two signals despite their

contrast. The planetary transmission signal is expected to vary over  $\sim 130 \text{ km s}^{-1}$  during the course of the transit owing to its orbital motion, while the stellar Doppler motion is only expected at the  $\sim 0.25 \text{ km s}^{-1}$  level. We generate a master spectral template from a median combination of the observed stellar spectra for a given night of observations, and we remove this from each observed TRES spectrum via division.

During a transit, the residual spectral signatures comprise contributions from the Doppler shadow (the Rossiter-McLaughlin effect; McLaughlin 1924; Rossiter 1924) and the transmission spectroscopic signatures from the atmosphere of the planet. Depending on the projected orbital obliquity and the velocity amplitude of the planet’s orbit, there is a region in the transit where the Doppler and transmission signals can overlap and cancel each other’s effects. When this occurs, the Doppler shadow manifests as a reduction in the apparent absorption in a spectral line, while the transmission signal manifests as an excess of absorption. To correct for this, we simultaneously model for Doppler shadow and planetary transmission spectrum.

The trail of the Doppler shadow is modeled as per Zhou et al. (2016), with the transit parameters describing the transit centroid  $t_0$ , period  $P$ , normalized semimajor axis  $a/R_*$ , inclination  $i$ , and radius ratio  $r_p/R_*$  fixed to that reported in Gaudi et al. (2017). From observation of the secondary eclipse phase of KELT-9b, Wong et al. (2020) measured an eccentricity of  $e < 0.007$  to  $2\sigma$  significance; therefore, the planet transmission spectrum is assumed to have the orbital velocity of a circular orbit. We perform a cross-correlation between the spectral residuals and a synthetic planetary spectrum, as is appropriate to reveal the planetary transmission spectrum. The Doppler transit signal is best revealed when the template best matches that of the host star spectrum, and the relative cross-correlation function height between the planetary signal and the Doppler signal changes based on the specific synthetic planetary spectrum and the specific species adopted for a given analysis. Therefore, to best remove the Doppler shadow signal, we scale the relative depths of the Doppler shadow and the transmission spectrum trail in our simultaneous fit. The Doppler shadow is then subtracted from our spectral data, leaving only the contribution from the planet’s atmosphere trail. The  $H\alpha$  transmission and Doppler shadow transit signals before and after subtraction are presented in Figure 2 via the top two panels.

To estimate the detection significance of the  $H\alpha$  transmission signal, we compute its S/N over an array of possible orbital velocities for the planet. We perform a grid search over the systematic velocity of the KELT-9 system,  $v_{\text{sys}}$ , and the radial velocity semiamplitude of the planet,  $K_p$ . At each grid point, we align the  $H\alpha$  residuals as per a circular orbit and average over all exposures captured between second and third contact (i.e., full transit). Figure 2 shows the S/N of the cross-correlation peak as a function of  $K_p$  and  $v_{\text{sys}}$  (third panel), as well as the cross-correlation function S/N at the predicted  $v_{\text{sys}}$  of the system (bottom panel). We find that the  $H\alpha$  transmission signal can be best traced by a circular orbit with  $K_p = 260 \pm 110 \text{ km s}^{-1}$  and  $v_{\text{sys}} = -24 \pm 18 \text{ km s}^{-1}$ .

The  $H\alpha$  transit light curve describes the strength of the  $H\alpha$  absorption during a transit observation. To determine the  $H\alpha$  flux for a given observation, we model the planetary  $H\alpha$  line profile as a Gaussian, with its integral defining its absorption strength.

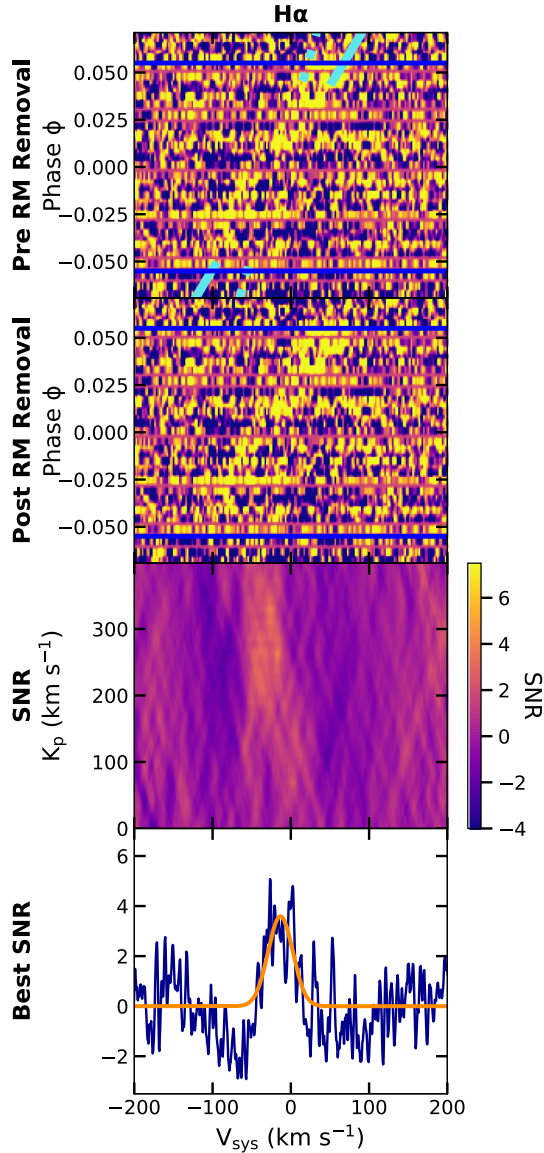


**Figure 2.** Cross-correlation between the ensemble of observations against the  $H\alpha$  absorption of KELT-9b. From top to bottom: the cross-correlation function analysis without the Doppler shadow subtracted (the solid cyan line represents the trail of the planet, and the dashed cyan line represents its Doppler shadow), the cross-correlation function analysis with the Doppler shadow subtracted, the cross-correlation S/N as a function of the planet’s orbital velocity  $K_p$  and systemic velocity  $v_{\text{sys}}$ , and the cross-correlation function at the best-fit orbital velocity.

Due to the intrinsic low S/N of the planetary absorption feature, we seek to reduce the flexibility of the Gaussian model fit during each epoch. We assume that the line profile width does not vary over the course of the observations. We also assume that the velocity of the planetary transmission signal follows that of the planetary circular orbit prescribed above.

The width  $\sigma$ , orbital velocity amplitude  $K_p$ , and systemic velocity  $v_{\text{sys}}$  are determined from a 2D elliptical Gaussian function fit to the master line profile, constructed from a median combination of all in-transit observations.

To compute the transit light curve, we model the local stellar spectrum blocked by the traversing planet via a Gaussian profile. The Gaussian profile has width  $\sigma$  and follows an orbit with amplitude  $K_p$  and systemic velocity  $v_{\text{sys}}$ . The resulting light curve describing the strength of the planetary  $H\alpha$  absorption through the transits is shown in Figure 4. We note that the per-point uncertainties of the light curve have been scaled such that the reduced  $\chi^2$  of the eventual light curve is at unity, after removal of the best-fit model from Section 3.2.

### 3.1.1. Estimating the Effect of Center-to-Limb Variations

The light curves representing transmission spectroscopic signals of deep Fraunhofer lines can be significantly affected by center-to-limb (CLV) effects. During a transit, the line profile of the planetary atmospheric spectrum is modulated by the flux of the deep stellar absorption feature. This effect naturally induces a “W” shape to the observed transmission spectrum light curve (e.g., Snellen et al. 2008; Zhou & Bayliss 2012; Wyttenbach et al. 2015; Cauley et al. 2016; Khalafinejad et al. 2017; Cauley et al. 2019).

To model this effect, we first compute the  $H\alpha$  line of KELT-9 at different limb angles corresponding to the phases of each spectral observation. We make use of the SPECTRUM spectral synthesis code (Gray & Corbally 1994) to compute the local  $H\alpha$  line profile as per Czesla et al. (2015). The planetary absorption feature is modeled as a Gaussian of width  $18 \text{ km s}^{-1}$  (as per its measured width) at the Keplerian velocity of the planet. The result is a net decrease in the relative absorption of the planet during midtransit, where the velocity of the planet aligns with that of the systemic velocity of the star. This model is incorporated in the following modeling described in Section 3.2. The dotted line in Figure 4 represents the best-fit model of the  $H\alpha$  absorption light curve accounting only for this center-to-limb effect.

### 3.2. $H\alpha$ Light-curve Model

Yan & Henning (2018) showed that the  $H\alpha$  radius of KELT-9b extends to 70% that of its Roche lobe, inferring that atmospheric escape may be ongoing for the highly irradiated planet. If the extended atmosphere of KELT-9b is nonspherical, as may be the case owing to significant ongoing mass loss, then the observed transits will be asymmetric.

To examine and quantify any temporal variability in the  $H\alpha$  transit light curve, we present a toy model that parameterizes a cometary-tail-shaped transit geometry to model the observed “W”-shaped transit. The model illustrates a neutral hydrogen tail being directed radially away from the star, toward the observer. We note, however, that neutral hydrogen in the  $n = 2$  excited state is not expected to be present far from the planet atmosphere (Section 5.2). This toy model nevertheless presents few free parameters and helps to quantify any variations between the multiple epochs of observations.

In this model, the in-transit absorption is “W” shaped because we see more of the tail during ingress and egress and less when it is aligned with our line of sight. Additional asymmetry in the transit, after inclusion of the center-to-limb effects described in Section 3.1.1, can be explained by a slight

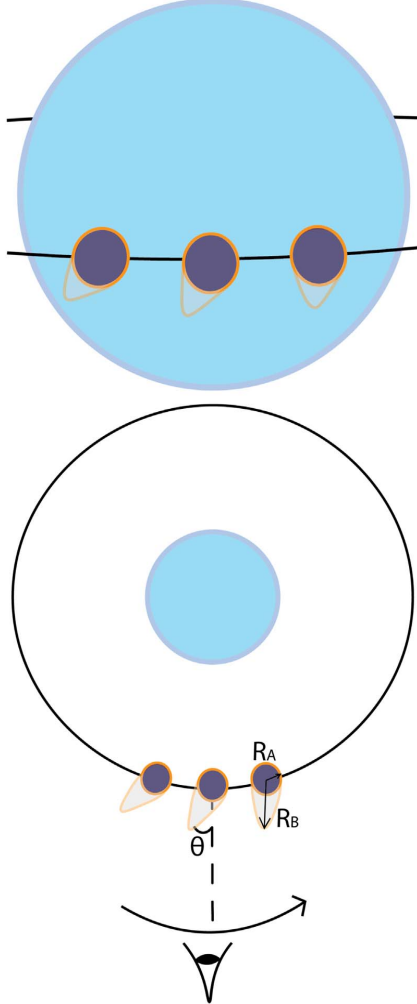


**Figure 3.** We present one model that successfully reproduces the observed “W”-shaped  $H\alpha$  transit of KELT-9b. In this toy model, the planet hosts a comet-like tail pointed away from the star. In this geometry, the area covered by the planet and tail is greatest during ingress and egress and is reduced during midtransit, resulting in a “W”-shaped transit as per our observations. The figure shows this toy model, with the tail pointed away from the star toward the observer, moving from right to left through the transit. The tail is modeled by a semiellipse with a short axis of radius similar to that of the planet  $R_A \approx R_p$ , and a tail of length  $R_B$  extending away from the planet toward the observer. Additional asymmetries in the transit are modeled by including a small tilt to the tail ( $\theta$ ), trailing away from the direction of motion. With only three free parameters in this toy model, we can easily compare the  $H\alpha$  transits between different observations and search for temporal variability in the  $H\alpha$  absorption from the planet’s atmospheres.

tilt in the angle of the tail along the orbital plane, perhaps due to the orbital motion of the planet. We test this hypothesis by constructing a semiellipsoid to represent the cometary tail of the planet’s escaping atmosphere. As shown in Figure 3, we denote the X-axis to be along the line of sight toward the observer, the Y-axis represents the horizontal axis along the sky plane, and the Z-axis is the vertical axis in the sky plane. The

combined planet and atmosphere evaporation is represented as a semiellipsoid, symmetric along the Y-axis and Z-axis but elongated away from the host star along the X-axis. The elongation is representative of the tail trailing behind the planet. Its projected area on the sky plane can be computed as half of that from the projection of the full ellipsoid except when the elongated axis is aligned with the X-axis exactly.

To compute the projected shape of an ellipsoid on the sky plane conveniently, we use the quadratic form of the ellipsoid to represent it. For example, an elongated ellipsoid along the X-axis can be expressed with equation  $\frac{x^2}{a^2} + \frac{y^2}{b^2} + \frac{z^2}{b^2} - 1 = 0$ , which can have a corresponding matrix of

$$Q = \begin{pmatrix} \frac{1}{a^2} & 0 & 0 & 0 \\ 0 & \frac{1}{b^2} & 0 & 0 \\ 0 & 0 & \frac{1}{b^2} & 0 \\ 0 & 0 & 0 & -1 \end{pmatrix}.$$

We assume that the ellipsoid rotates counterclockwise around the Z-axis by an angle  $\theta$  (due to the movement along the orbit of the planet). The rotated ellipsoid can therefore be expressed with the matrix  $Q' = I^{-1} Q I$ , where  $I$  represents the rotation matrix along the inclination,  $i$ , of the planet rotated around the Y-axis. Inclination  $i = 90^\circ$  when the impact parameter of the planet is 0:

$$I = \begin{pmatrix} \sin i & 0 & \cos i & 0 \\ 0 & 1 & 0 & 0 \\ -\cos i & 0 & \sin i & 0 \\ 0 & 0 & 0 & 1 \end{pmatrix}.$$

The projection of  $Q'$  onto any plane should be an ellipse represented by the matrix  $C = (P(Q')^{-1}P^T)^{-1}$ , where  $P$  is the camera matrix. The camera matrix  $P$  for a sky plane projection on the Y- and Z-axes is

$$P = \begin{pmatrix} 0 & 1 & 0 & 0 \\ 0 & 0 & 1 & 0 \\ 0 & 0 & 0 & 1 \end{pmatrix}.$$

The resulting matrix,

$$C = \begin{pmatrix} \frac{1}{\beta^2} & 0 & 0 \\ 0 & \frac{1}{\gamma^2} & 0 \\ 0 & 0 & -1 \end{pmatrix},$$

can be interpreted as an ellipse with the familiar function form of  $\frac{y^2}{\beta^2} + \frac{z^2}{\gamma^2} = 1$ .

We compare our derived  $H\alpha$  light curve to the toy light-curve model described above via a Markov Chain Monte Carlo (MCMC) exercise. We account for free parameters describing the semiellipsoid radius along the Y-axis and Z-axis ( $R_A/R_*$ ), radius along the X-axis ( $R_B/R_*$ ), and tilt of the tail ( $\theta$ ). Our model also includes the center-to-limb variation described in Section 3.1.1, with the obliquity of the planet orbit assumed to be  $\lambda = -84^\circ$  as per Gaudi et al. (2017). Our MCMC uses 50 walkers over 5000 iterations per walker to explore the posterior

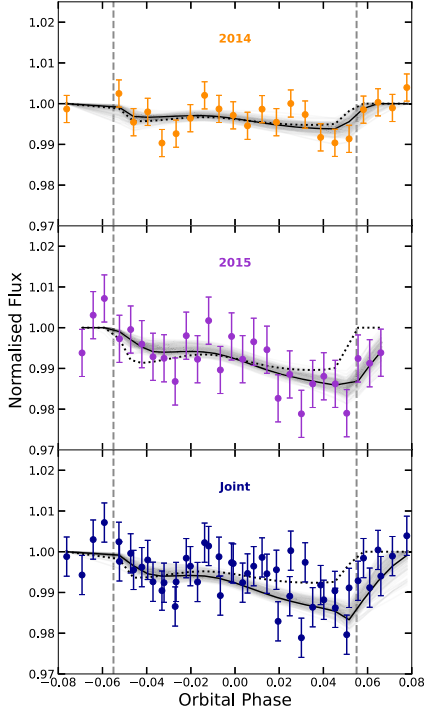


**Figure 4.** Light curve showing the time variation of the  $H\alpha$  absorption across each transit. The  $H\alpha$  light curves for the 2014 (top) and 2015 (middle) epochs are plotted independently. The best-fit escaping tail model is marked by the solid black line on each panel, while the spherical (no-tail) model is marked by the dotted line. We also jointly fit the 2014 and 2015 observations (bottom), with the gray lines representing 200 randomly drawn models from our posterior. The vertical dashed lines represent the ingress and egress for each epoch.

probability distribution. We analyze the 2014 and 2015 light curves independently and then model the joint data set. Free parameters include the radius and tilt parameters  $R_A$ ,  $R_B$ , and  $\theta$  and two free parameters allowing for a linear trend to the light curve. The model also includes the standard transit parameters of normalized semimajor axis  $a/R_*$ , line-of-sight inclination  $i$ , transit epoch  $T_0$ , and orbital period  $P$ , the values of which are adopted and fixed to those from Gaudi et al. (2017). For our combined 2014 and 2015 analysis, a separate linear trend is allowed for each night of observations. To prevent our walkers from exploring unrealistic values, we restrict our  $R_A$  and  $R_B$  parameter spaces to be positive while constraining  $\theta$  between  $-90^\circ$  and  $90^\circ$ . For each epoch, the best-fit  $R_A$ ,  $R_B$ , and  $\theta$  parameters are determined from the median of their respective posterior distributions.

Figure 4 and Table 1 present the best-fit models for our individual and combined 2014 and 2015  $H\alpha$  light curves. Figure 5 presents the  $1\sigma$  and  $2\sigma$  comparison among these free parameters. No significant variability was detected between the two epochs of observations at the  $3\sigma$  level.

We note that our fit does not incorporate the velocity profile of the outflow. Owen (2019) modeled the velocity profile of ongoing  $\text{Ly}\alpha$  escape and showed that a net blueshift line profile is expected. Figure 8 shows that we measure a broadened  $H\alpha$

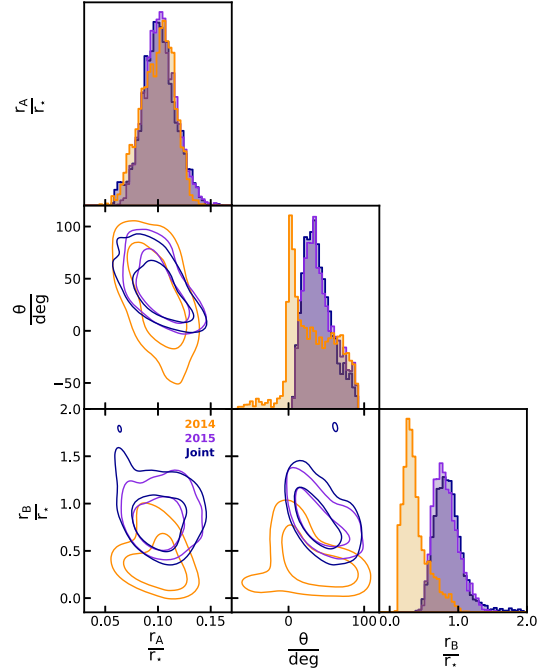


**Figure 5.** The derived parameter values for  $R_A$ ,  $R_B$ , and  $\theta$  when fitting our projected geometric model against the 2014 (orange) and 2015 (purple) epochs, and a combined (navy) data set via MCMC. The inner circle for each contour represents  $1\sigma$  accuracy, while the outer circle represents  $2\sigma$ . The histograms display the posterior distribution for each parameter in the 2014, 2015, and joint scenarios.

**Table 1**  
The Best-fit Values of Our  $H\alpha$  Transit Model

Epoch	$R_A (R_*)^a$	$R_B (R_*)^b$	$\theta$ (deg) <sup>c</sup>
2014	$0.101^{+0.014}_{-0.018}$	$0.33^{+0.24}_{-0.12}$	$28^{+39}_{-25}$
2015	$0.102^{+0.015}_{-0.015}$	$0.80^{+0.20}_{-0.15}$	$38^{+27}_{-16}$
Joint	$0.101^{+0.016}_{-0.015}$	$0.84^{+0.20}_{-0.17}$	$36^{+22}_{-15}$

**Notes.**

<sup>a</sup> The length of the short axis of the half-ellipse, in units of stellar radii.

<sup>b</sup> The length of the long axis of the half-ellipse, in units of stellar radii.

<sup>c</sup> Tilt in the ellipse with respect to the orbit normal.

velocity profile, as compared to the detected metallic absorption features (Section 4). A full model that describes the line profiles will include an opacity profile for the escaping gas and possibly invoke more complex modeling of stellar wind interactions that go beyond the scope of this study.

#### 4. Searching for Metallic Absorption Features

At temperatures of  $\sim 4900$  K on the dayside of KELT-9b, we expect complete disassociation of molecular species commonly found in planetary atmospheres. Instead, we expect the presence of atomic species such as Fe I, Fe II, Mg I, Ca I, Ca II, Cr II, Sc II, Ti II, and Y II, all of which have been identified in previous publications performing retrieval analysis on KELT-9b (Hoeijmakers et al. 2018; Cauley et al. 2019;

Hoeijmakers et al. 2019; Yan et al. 2019; Turner et al. 2020; Pino et al. 2020; Bello-Arufe et al. 2022). We use our TRES observations to search for the transmission spectrum from the upper atmosphere of the planet.

First, we remove the stellar spectrum as per Section 3.1, via the removal of a median-combined stellar spectrum of KELT-9b. We apply these corrections across all orders for a given exposure. Orders with significant telluric  $O_2$  absorption (outlined in Section 2) are excluded from the analysis. To detect the shallow planetary transmission spectral signature, we cross-correlate the observed spectra against a synthetic template of the planetary atmosphere.

#### 4.1. Synthetic Model Spectrum

In this work, we calculate the absorption cross sections of each species using the open-source and custom opacity calculator HELIOS-K (Grimm et al. 2021). We assume Voigt line profiles for the absorption lines and  $0.258 \text{ km s}^{-1}$  spectral resolution at a reference wavelength of  $5000 \text{ \AA}$ . We adopt other default settings of HELIOS-K, such as the line-wing cutting length, as per Grimm et al. (2021). In this work, we explore the line list from Kurucz (2017) to calculate the neutral and singly ionized metals: Fe I, Fe II, Ca I, Ca II, Mg I, Mg II, O I, Sc II, Cr II, Ti I, Ti II, TiO, and Y II.

Although we anticipate recovering atomic species only, some molecules were also explored. The line lists for the molecules investigated are  $H_2O$  (Barber et al. 2006),  $CH_4$  (Yurchenko & Tennyson 2014), CrH (Burrows et al. 2002), SiO (Barton et al. 2013), SiH (Yurchenko et al. 2018), VO (McKemmish et al. 2016), MgH (Yadin et al. 2012), and TiO (McKemmish et al. 2019). The chemical concentrations in the atmosphere are calculated using the open-source code FastChem (Stock et al. 2018). For the transmission spectra, we write a script that takes into account the results from HELIOS-K and FastChem and is based on the simple formalism presented in Gaidos et al. (2017) and Bower et al. (2019). Our model computes the effective tangent height in an atmosphere that was discretized in 200 annuli (Bello-Arufe et al. 2021; Cabot et al. 2021). We include in our model the  $H^-$  bound-free and free-free absorption from John (1988). Each transmission spectrum includes one gas species along with  $H^-$  continuum absorption and scattering by H and  $H_2$ .

The models use the planet bulk parameters presented in Gaudi et al. (2017) and assume that the atmosphere is isothermal at its equilibrium temperature.

#### 4.2. Cross-correlation against Spectral Residuals

A forest of metallic absorption lines is present in the optical wavelengths of highly irradiated hot Jupiters. We perform a cross-correlation between the observed spectral residuals and the synthetic planetary spectra described above.

To reduce edge-induced effects in the cross-correlation, we apply a 30% cosine apodization to the edge of the observed spectrum. The cross-correlation is performed using the PyAstronomy package (Czesla et al. 2019). The cross-correlation functions from each order are average combined, weighted by their noise, to a master cross-correlation function per exposure. We further correct for the Doppler shadow of the planetary transit as per Section 3.1.

The transmission signature of the atmosphere of KELT-9b was identified in archival TRES transit observations from 2014

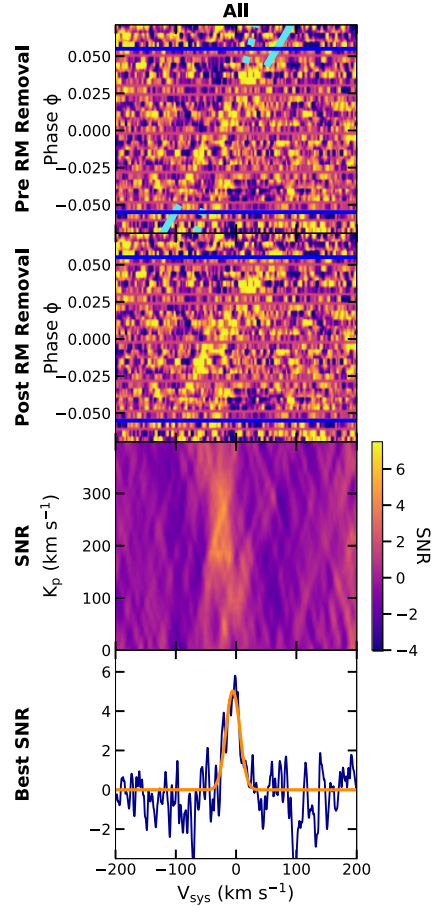


Figure 6. The cross-correlation function for the full synthetic absorption spectrum of KELT-9b. Figure description is as per Figure 2.

and 2015. Figure 6 shows the transmission spectroscopic signal of KELT-9b from the joint 2014 and 2015 data sets, including the cross-correlation function  $S/N$  as a function of the orbital parameters  $K_p$  and  $v_{\text{sys}}$ . We report a  $6\sigma$  detection of the joint 2014 and 2015 data sets. In addition, Fe I, Fe II, and Mg I were individually detected at a significance of  $6\sigma$ ,  $6\sigma$ , and  $4\sigma$ , respectively (Figure 7). Due to the difference in  $S/N$  between our observations and those from previous literature (Yan et al. 2019; Turner et al. 2020), we did not recover the transmission signals of Ca I, Ca II, Cr II, Sc II, Ti II, and Y II, nor any of the investigated molecules for KELT-9b.

#### 4.3. Stellar and Planetary Mass Estimates

Spectroscopic detections of the planetary transit allow us to empirically determine the dynamical masses of both components of the system. In this scenario, the system can be solved as a double-lined eclipsing binary, with the stellar radial velocity amplitude  $K_*$  and the planet radial velocity amplitude  $K_p$  being independently measured.

The best-fit planetary radial velocity amplitude for each species with a strong cross-correlation peak is tabulated in

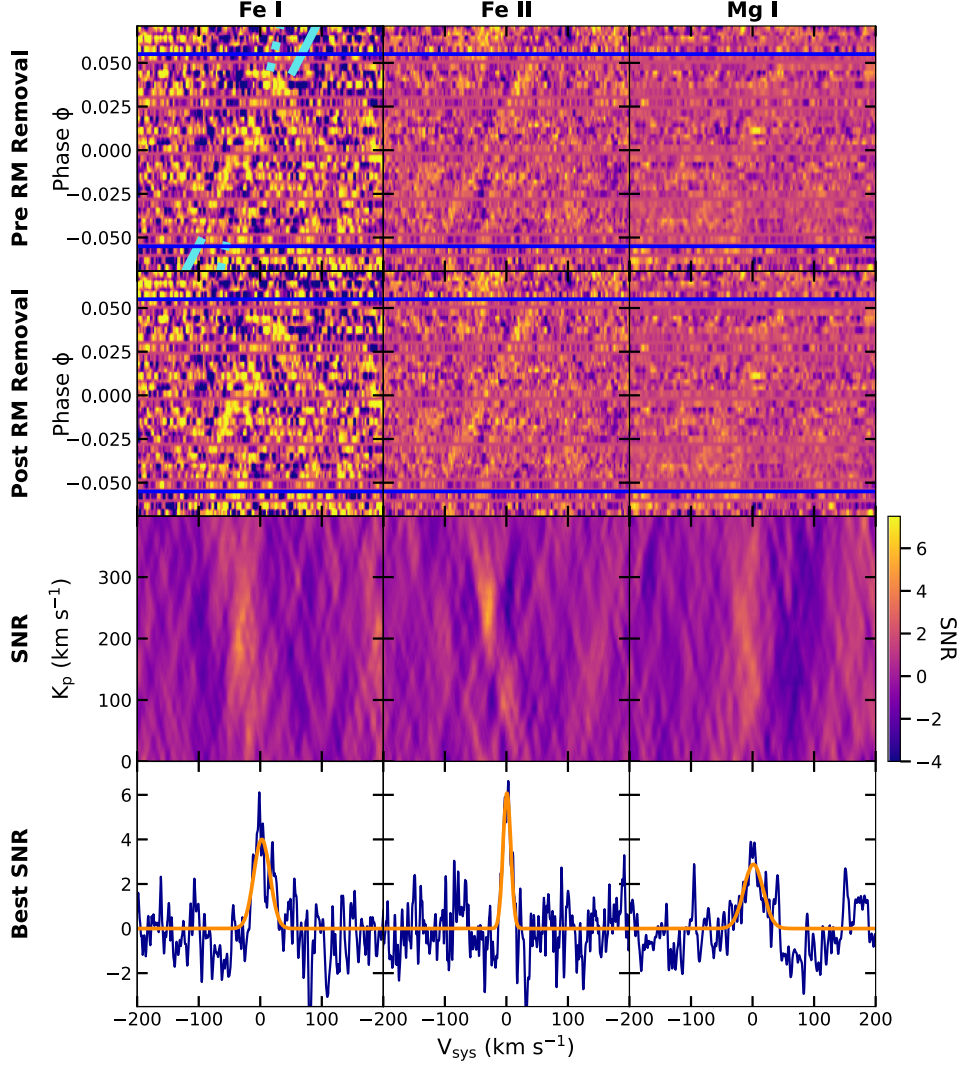


Figure 7. The cross-correlation function for Fe I, Fe II, and Mg I. Figure description is as per Figure 2.

Table 2. For each species, we compute the cross-correlation function strengths as a function of the planetary radial velocity amplitude  $K_p$  and the systemic velocity  $v_{\text{sys}}$  (e.g., Figure 6). We then fit a 2D Gaussian to the cross-correlation function height  $K_p$  and  $v_{\text{sys}}$  surface. As there is significant scatter in the resulting best-fit velocity amplitudes, we adopt the standard deviation of the scatter in the solutions for each species as the uncertainty in the subsequent mass calculations.

Rearranging the standard radial velocity equation for an aligned circular orbit (e.g., Perryman 2018),

$$K_* = \left( \frac{2G}{P} \right)^{1/3} \frac{M_p}{M_* + M_p}^{2/3}, \quad (1)$$

for the stellar mass  $M_*$  we get

$$M_* = K_*^3 \frac{P}{2\pi G} \frac{(q+1)^2}{q^3}, \quad (2)$$

where  $q$  is the ratio between the radial velocity amplitude of the star and the planet  $q = K_*/K_p$ . Likewise, the planet mass is

$$M_p = M_* q. \quad (3)$$

Adopting the period  $P$  and stellar radial velocity amplitude  $K_*$  from Gaudi et al. (2017), along with our measured planetary radial velocity amplitude  $K_p = 231 \pm 27 \text{ km s}^{-1}$ , we get  $M_* = 1.91 \pm 0.68 M_\odot$  and  $M_p = 2.31 M_J \pm 0.89 M_J$ . Both our stellar mass and planet mass are consistent with the values

**Table 2**  
Measurements of Orbital and Systemic Velocities from Per-species Cross Correlations

Species	Orbital Velocity $K_p$ ( $\text{km s}^{-1}$ ) <sup>a</sup>	Systemic Velocity $v_{\text{sys}}$ ( $\text{km s}^{-1}$ ) <sup>b</sup>
Combined template	$230 \pm 140$	$-23 \pm 18$
H $\alpha$	$260 \pm 110$	$-24 \pm 18$
Fe I	$200 \pm 140$	$-28 \pm 18$
Fe II	$260 \pm 50$	$-32.6 \pm 8.3$
Mg I	$200 \pm 160$	$-13 \pm 17$
Adopted values for mass calculations	$231 \pm 27$	$-25 \pm 10$

**Notes.**

<sup>a</sup> Best-fit orbital velocity; quoted uncertainties are the widths of the 2D Gaussian fit along the  $K_p$  plane.

<sup>b</sup> Best-fit systemic velocity; quoted uncertainties are the widths of the planetary absorption feature.

reported in Gaudi et al. (2017) and Pai Asnodkar et al. (2022) to within  $1\sigma$ .

## 5. Discussion

In this paper, we sought to characterize the transmission spectrum of the ultrahot Jupiter KELT-9b. We report a reanalysis of multiepoch transits obtained with the TRES facility on the 1.5 m telescope at FLWO. The observations yielded detections of excess H $\alpha$  absorption about the planet, which has been previously cited as a potential indirect tracer for ongoing atmospheric escape. We also report detections of select atomic species in the optical transmission spectrum of KELT-9b. The positive detections of planetary atmospheric features by a meter-class facility open the possibility of long-term temporal monitoring for highly irradiated planets.

### 5.1. H $\alpha$ as a Tracer for Evaporation and Temporal Atmospheric Variations

Evaporative processes play a key role in shaping the evolution of close-in exoplanets. Observations of excess planetary absorption of H $\alpha$  probe the extended neutral hydrogen envelope of planets as they undergo mass loss. The shape and size of the neutral hydrogen transits can also provide key tests for the interactions between the stellar wind and the escaping hydrogen exosphere. Owen et al. (2023) note that the observed Ly $\alpha$  excess is most dependent on timescale of photoionization of the neutral hydrogen tail. In strong extreme-UV environments, the neutral hydrogen tail that is optically thick in Ly $\alpha$  is quickly ionized by the stellar wind, resulting in a reduced transit depth in these wavelengths. 3D simulations (e.g., Kubyshkina et al. 2022) also reinforce the importance of stellar wind interactions for the observed shape and sizes of the escaping neutral hydrogen tails.

Multiepoch analysis of the KELT-9b H $\alpha$  extended atmosphere has the potential of revealing temporal variabilities in the neutral hydrogen tail of the planet. Cauley et al. (2019) reported an asymmetric “W”-shaped H $\alpha$  transit light curve, while Yan & Henning (2018) noted no asymmetric substructure in their transits (although S/N in their data set prohibited them from resolving velocity centroids of individual transmission spectra). Our observations agree with those of Cauley et al. (2019) and reveal a “W”-shaped transit in both our 2014 and 2015 TRES transits

(Figure 4). A “W” shape is recovered when constructing a spherical transit model that incorporates the CLV variations as outlined in Section 3.1.1; however, its contribution appears insufficient at explaining all the observed asymmetries. We offer a tail model as one possible scenario to explain the remaining asymmetries. In this scenario, we treat our H $\alpha$  light curve as being induced via an occultation of escaping material in the form of a half ellipsoid, with the shorter axis with length approximately that of the radius of the planet ( $R_A \approx R_p$ ), and an elongated axis trailing away from the planet in the form  $R_B$  with a tilt of  $\theta$ . With these additional free parameters, this model sufficiently explains the remaining asymmetries seen in the light curve and also offers a better-fitting model that can be used to search for any temporal variabilities in the transit shapes, though none were detected at  $>3\sigma$  significance.

To test the robustness of our models, we perform a Bayesian inference criterion (BIC) at each epoch, comparing the difference between the tail versus spherical transit scenarios. We find that the tail model is preferred when each epoch is considered individually and when the observations are modeled together, with  $\Delta\text{BIC}_{2014} = -70$ ,  $\Delta\text{BIC}_{2015} = -249$ , and  $\Delta\text{BIC}_{\text{combined}} = -11$  respectively.

We note that this model departs from standard models of atmospheric escape. Past neutral hydrogen transit models tend to assume that the outflowing gas trails behind the planet along its orbital path (e.g., Owen et al. 2023). This has been justified by the extended Ly $\alpha$  transits of GJ 436b (Lavie et al. 2017). However, “energetic neutral atoms” have been observed to stream radially away from solar system planets and have been proposed as a dominant process shaping the Ly $\alpha$  absorption of hot Jupiters. Holmström et al. (2008) and Ekenbäck et al. (2010) proposed that the Ly $\alpha$  excess of HD 209458b can be explained by a radial tail of energetic neutral atoms. The radial neutral hydrogen tail is formed when high-velocity protons from the stellar wind exchange electrons with the lower-velocity neutral hydrogen escaping from the atmosphere of the planet. The resulting tail streams away from the planet, as it primarily retains the momentum of the stellar wind. The energetic neutral atom tail has been observed for Venus, Earth, and Mars (Futaana et al. 2011). In addition, Owen et al. (2023) note that ram pressure from the stellar wind is sufficient to induce a significant radial component to the escaping neutral hydrogen exosphere from the planet. Mitani et al. (2022) showed through 2D hydrodynamic simulations that ram pressure from the stellar wind particles is sufficient in producing a tail escaping toward the observer’s line of sight. They also note that the H $\alpha$  transit depth does not strongly depend on the stellar mass-loss rate. H $\alpha$  absorption is dominated by the dense inner region of the exosphere and is more protected from the stellar wind than other escape tracers, such as Ly $\alpha$ .

Typical signatures of atmospheric evaporation, such as the UV Ly $\alpha$  line and infrared He I  $\lambda$ 10830 line, are inaccessible to meter-class facilities, but H $\alpha$  may be an indicator for mass loss that is accessible to meter-class ground-based observations. A number of other planets have reported H $\alpha$  excess absorption, including KELT-20b (e.g., Casasayas-Barris et al. 2018, 2019). Continued monitoring of these transits can help constrain models of stellar wind interactions with escaping planetary atmospheres. Understanding these interactions is key to properly modeling other observational signatures of evaporating atmospheres.

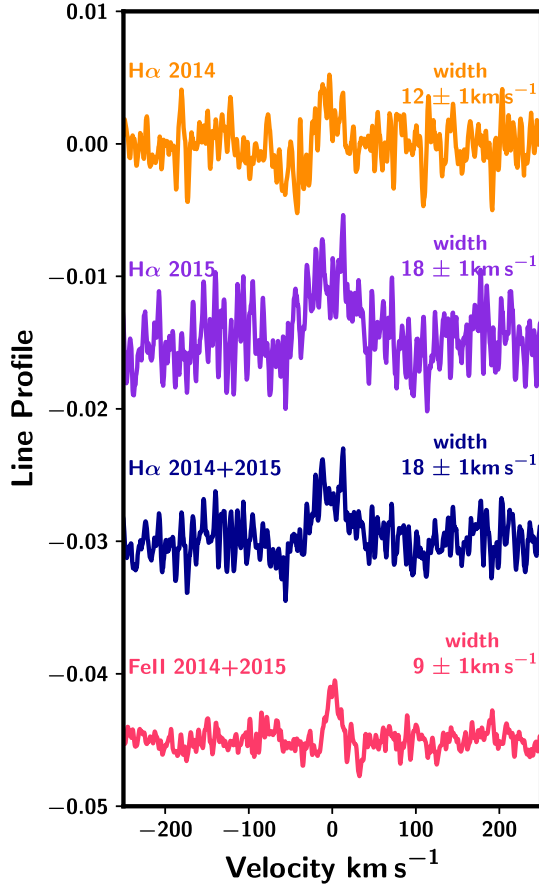


**Figure 8.** The line profile of the  $H\alpha$  absorption feature, compared to that for Fe II.  $H\alpha$  shows significant line broadening at the  $\sim 20 \text{ km s}^{-1}$  level in both 2014 and 2015. For comparison, the widths of photospheric lines like Fe II are consistent with instrument broadening. Extended broadening of  $H\alpha$  is consistent with the material forming an escaping exosphere about the planet.

Figure 8 shows the observed velocity profiles of the neutral hydrogen in KELT-9b, with the photospheric absorption profile of Fe II plotted for comparison. The  $H\alpha$  profile is significantly broader than that of the metallic absorption features in the transmission spectrum. We note that no significant blueshift is seen in the  $H\alpha$  line, as would be expected for rapidly escaping gas being accelerated by the stellar wind. This is consistent with the  $H\alpha$  velocity profile from Yan & Henning (2018). Models of “energetic neutral atom” tails of HD 209458b (Holmström et al. 2008) predict that the  $\text{Ly}\alpha$  line profile should be broadened by  $\sim 100 \text{ km s}^{-1}$  and be somewhat blueshifted. If  $H\alpha$  traces escaping neutral hydrogen for KELT-9b, it likely probes a much deeper zone in the exosphere and thus may not exhibit such a dramatic velocity broadening.

### 5.2. A Lack of $n = 2$ Excited Neutral Hydrogen in the Exosphere

Significant  $H\alpha$  absorption stemming from the extended tail requires a high number density of neutral hydrogen at the  $n = 2$

excited state. Maintaining a large population of neutral hydrogen at the  $n = 2$  excited state is a challenge outside of the atmosphere of the planet. Christie et al. (2013) demonstrated that neutral hydrogen at the metastable  $n = 2$  state provides significant absorption only for the optically thick parts of the atmosphere. Extended atmospheres are dominated by ionized hydrogen, which provides little absorption over the  $H\alpha$  line. As is, there are significant issues with the interpretation that the observed “W”-shaped  $H\alpha$  transit is induced by an extended  $n = 2$  tail escaping the planet. For a given population of  $H\alpha$  that might form at the upper boundary of the thermosphere, the sudden decrease in temperature at the thermopause could revert the majority of the population back to the ground state or become ionized.

Additional MHD modeling has also demonstrated that the  $n = 2$  population is not shaped by the stellar wind in the same manner as  $\text{Ly}\alpha$  absorption (e.g., Mitani et al. 2022), and as such it may not follow a cometary-tail-shaped outflow as suggested by our modeling.

We note that our escaping tail toy model for the “W”-shaped  $H\alpha$  transit of KELT-9b may not present a physical representation of the shape of the  $H\alpha$  envelope for the planet, but instead we propose that our model be used as a tracer for temporal variability among epoch observations that present “W”-shaped light curves. Improved center-to-limb non-LTE modeling of the  $H\alpha$  stellar absorption feature may suggest that  $H\alpha$  transit light curves should be naturally “W” shaped without invoking exotic transit geometries.

### 5.3. Detection of Metallic Transmission Spectroscopic Signatures from Meter-class Telescopes

The work in this paper was achieved using the TRES spectrograph on the 1.5 m FLWO reflector. Our work demonstrates the role that small meter-class ground-based telescopes can potentially play toward future exoplanet atmosphere characterization, especially for monitoring the interactions between evaporating atmospheres and the stellar environments they reside in. In addition to the  $H\alpha$  extended atmosphere of KELT-9b, we also successfully recovered the transmission spectrum from Fe I, Fe II, and Mg I at a significance of  $6\sigma$ ,  $6\sigma$ , and  $4\sigma$ , respectively. The independent atmospheric detections for all epochs are presented in Figure 9 in the Appendix, with independent molecular species analysis for 2014 and 2015 presented in Figures 10 and 11 in the Appendix, respectively. Due to the lower S/N of our observations compared to literature observations of KELT-9b, we report a null detection of Ca I, Ca II, Cr II, Sc II, Ti II, and Y II, previously reported to be present in high-resolution transmission spectra of the planet. KELT-9b is the first exoplanet to have atomic Fe I and Fe II directly detected in its atmosphere. These elements, typically found in cloud condensates in cooler atmospheres, are present in their atomic and ionized forms in the highly irradiated upper atmosphere of KELT-9b (Heng 2016; Stevenson 2016; Hoeijmakers et al. 2018). The stronger presence of Fe II versus Fe I is further confirmation of the high temperatures being achieved in the upper regions of the atmosphere (Hoeijmakers et al. 2018, 2019; Pino et al. 2020). Our detection of Mg I is the third KELT-9b observational data set to achieve this, succeeding Cauley et al. (2019) and Hoeijmakers et al. (2019). Huang et al. (2017) proposed magnesium to be an important atmosphere coolant owing to its electron impact followed by

radiative de-excitation ability, and it is potentially an indicator for evaporation (Bourrier et al. 2015).

## 6. Conclusion

KELT-9b is the hottest close-in Jovian planet known. In this paper, we report the reanalysis of archival high-resolution spectroscopic transits of KELT-9b from the TRES spectrograph on the 1.5 m reflector at FLWO. These observations, obtained in 2014 and 2015, revealed the extended neutral hydrogen atmosphere of KELT-9b, as well as the presence of atomic species in its upper atmosphere. From these observations we recover signals of Fe I, Fe II, Mg I, and H $\alpha$ . Using the velocity of the planetary signal during transit, we estimate a planetary and stellar mass of  $2.31M_J \pm 0.89M_J$  and  $1.91 \pm 0.68 M_\odot$ , respectively, all in agreement with previous publications. The H $\alpha$  absorption exhibits a “W”-shaped transit in both the 2014 and 2015 observations, which we model as evaporated material escaping KELT-9b and traveling radially away from the planet toward the direction of the observer. This is unlikely to be the true cause of light-curve trajectory, due to the assumed inability of H $\alpha$  to sustain a significant absorption  $n = 2$  population. Therefore, we instead use this model as an example of how to monitor temporal variability among individual epochs for “W”-shaped light curves. Our findings highlight the potential impact of meter-class telescopes in exoplanet atmosphere characterization, and our model presents an alternative for monitoring “W”-shaped light curves where external effects, such as those invoked by CLV, are insufficient at explaining all observed asymmetries.

We would like to acknowledge and pay respect to Australia’s Aboriginal and Torres Strait Islander peoples, who are the traditional custodians of the lands, the waterways, and the skies all across Australia. We thank you for sharing and

caring for the land on which we are able to learn. In particular, we pay our deepest respects to all Elders, ancestors, and descendants of the Giabal, Jarowair, and Yuggera nations, upon which the analysis for this paper was undertaken. We would also like to acknowledge and pay our deepest respects to the Indigenous American Elders, ancestors, and descendants who are the traditional custodians of the land upon which the Fred Lawrence Whipple Observatory is situated. We would like to thank the referee for their comments, as they significantly improved the scientific output of this publication. G.Z. acknowledges the support of the ARC DECRA program DE210101893. C.H. acknowledges the support of the ARC DECRA program DE200101840. We also thank Jessica Mink for running the TRES pipeline and maintaining the TRES archive. We acknowledge Andrew H. Szentgyorgyi, Gabor Fűrész, and John Geary, who played major roles in the development of the TRES instrument.

*Facility:* TRES

*Software:* Adobe Illustrator (Adobe Inc., 2022), astropy (Astropy Collaboration et al. 2018), batman (Kreidberg 2015), emcee (Foreman-Mackey et al. 2013), FastChem (Stock et al. 2018), HELEOS-K (Grimm et al. 2021), Matplotlib (Hunter 2007), NumPy (Harris et al. 2020), PyAstronomy (Czesla et al. 2019), SciPy (Virtanen et al. 2020), seaborn (Waskom 2021), Spectrum (Gray & Corbally 1994), telfit (Gullikson et al. 2014)

## Appendix Additional Figures

This section presents the independent atmospheric detections for all species and epochs analyzed from the TRES archival data of KELT-9b.

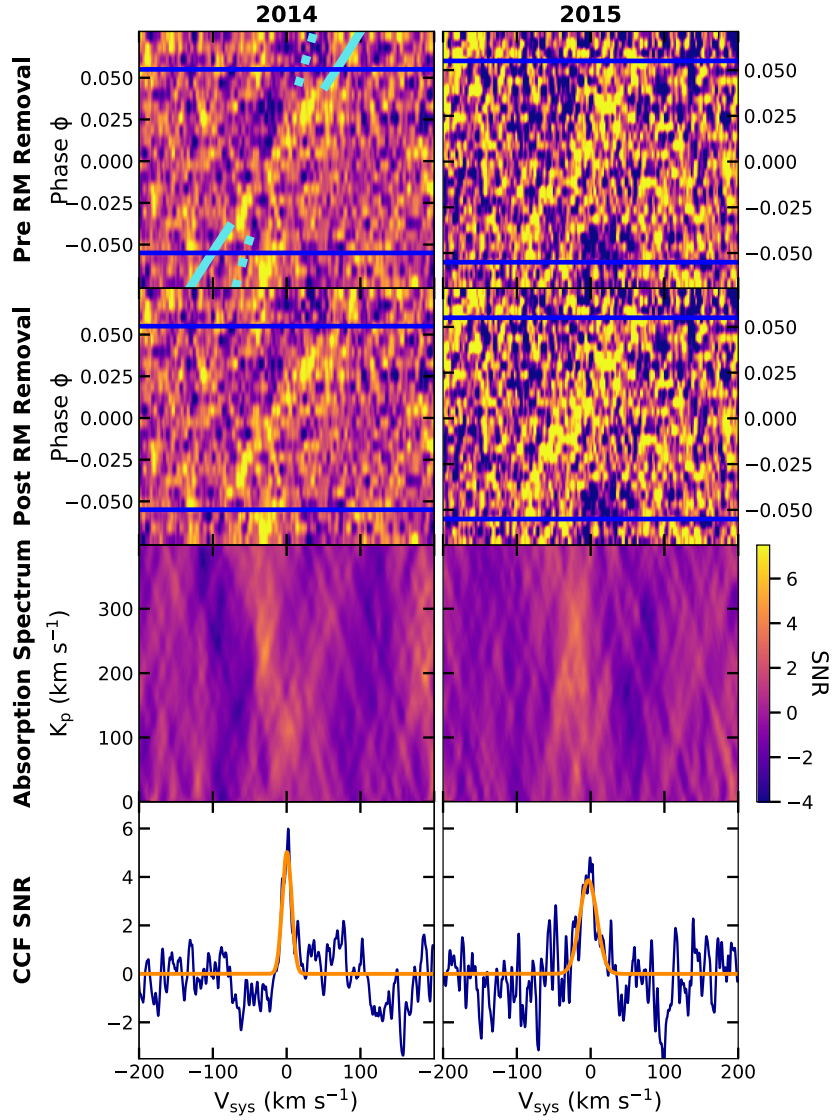


**Figure 9.** The cross-correlation function for the full synthetic absorption spectrum of KELT-9b at the individual 2014 and 2015 epochs. Figure description is as per Figure 2.

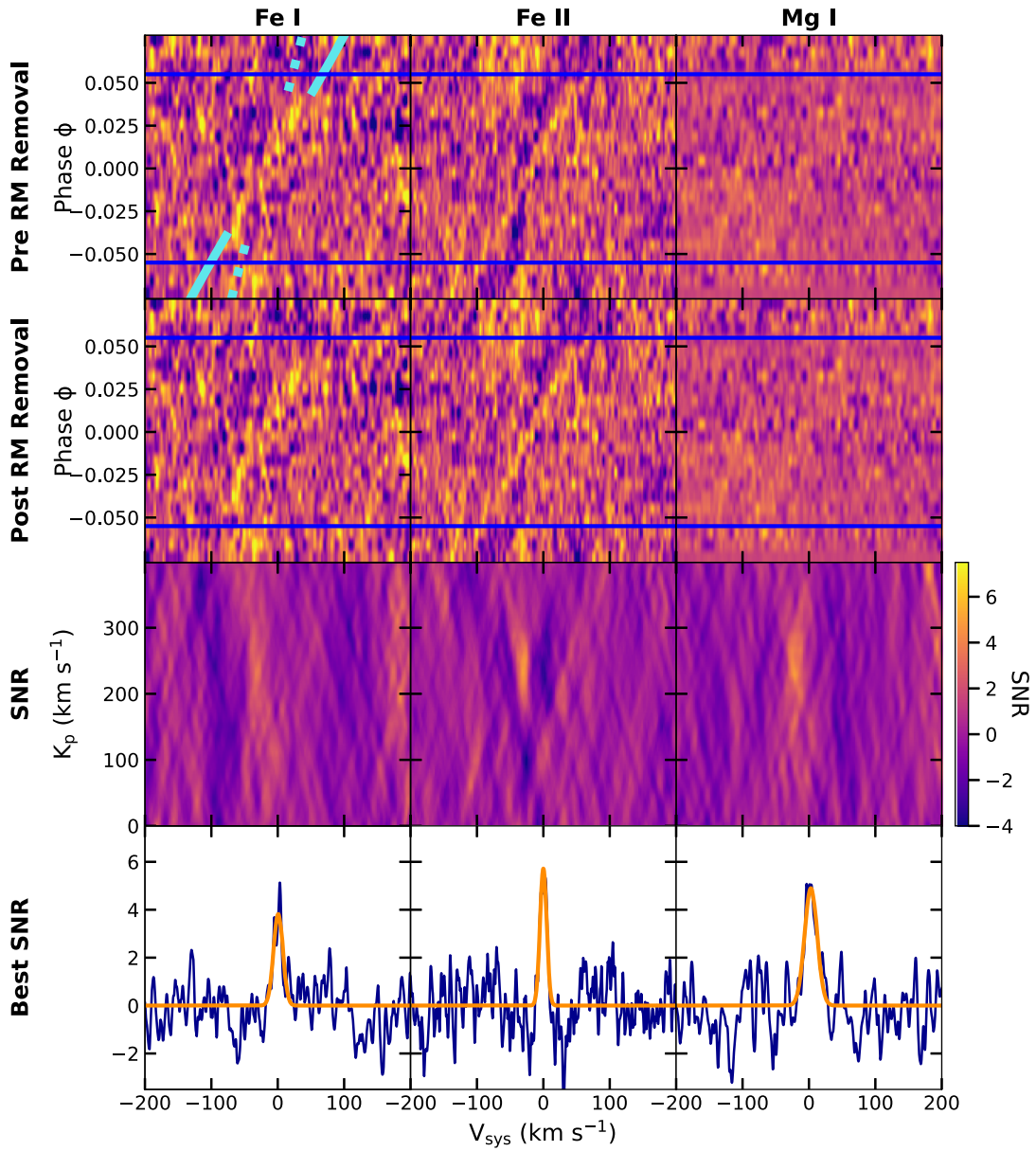


Figure 10. Individual cross-correlation analysis for the KELT-9b 2014 epoch using templates for Fe I, Fe II, and Mg I. Figure description is as per Figure 2.

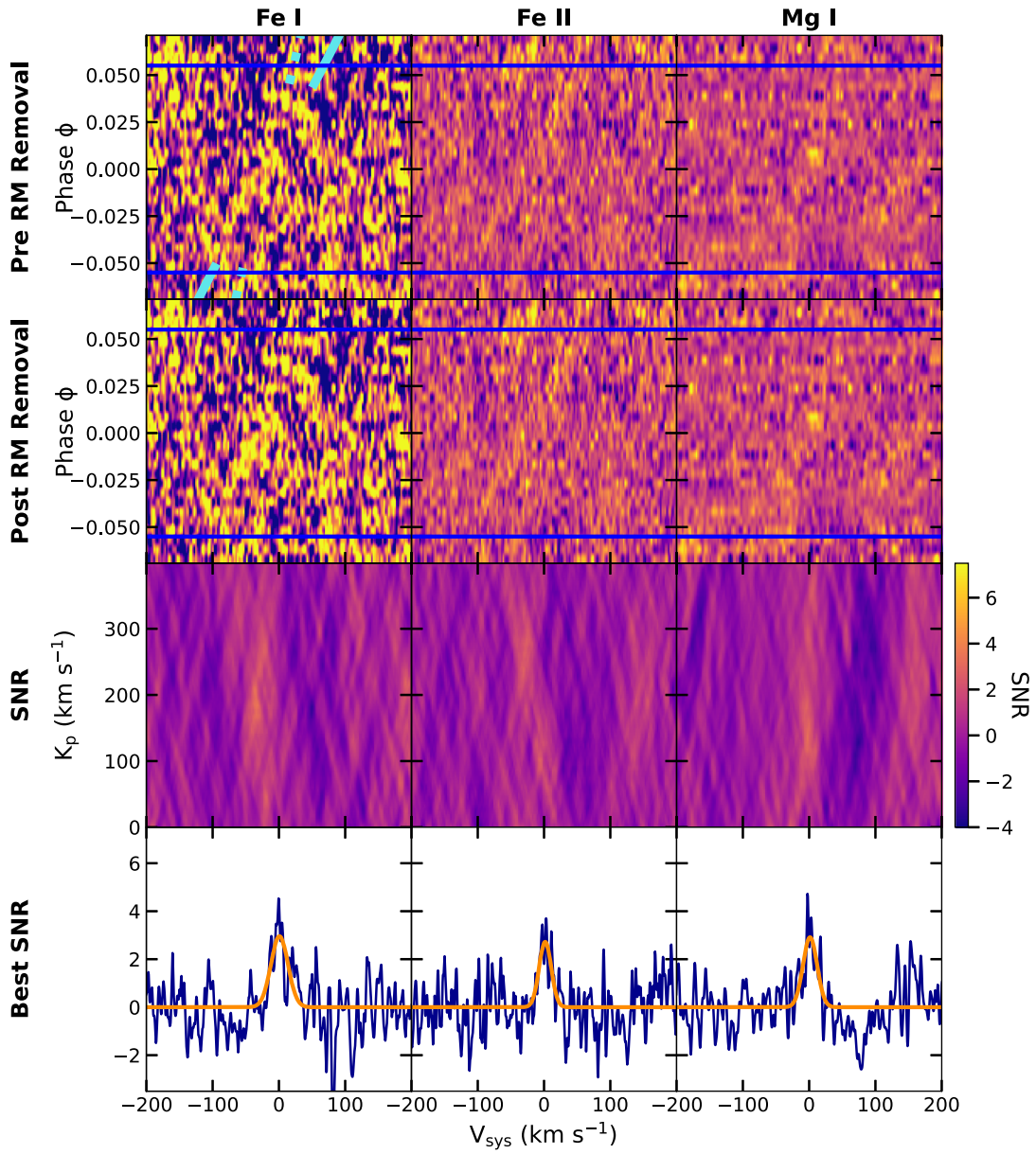


Figure 11. Individual cross-correlation analysis for the KELT-9b 2015 epoch using templates for Fe I, Fe II, and Mg I. Figure description is as per Figure 2.

## ORCID iDs

Nataliea Lowson  <https://orcid.org/0000-0001-6508-5736>  
 George Zhou  <https://orcid.org/0000-0002-4891-3517>  
 Duncan J. Wright  <https://orcid.org/0000-0001-7294-5386>  
 Chelsea X. Huang  <https://orcid.org/0000-0003-0918-7484>  
 João M. Mendonça  <https://orcid.org/0000-0002-6907-4476>  
 Samuel H. C. Cabot  <https://orcid.org/0000-0001-9749-6150>  
 Robert A. Wittenmyer  <https://orcid.org/0000-0001-9957-9304>  
 David W. Latham  <https://orcid.org/0000-0001-9911-7388>  
 Allyson Bieryla  <https://orcid.org/0000-0001-6637-5401>  
 Gilbert A. Esquerdo  <https://orcid.org/0000-0002-9789-5474>  
 Michael L. Calkins  <https://orcid.org/0000-0002-2830-5661>

## References

- Adobe Inc. 2022, Adobe Illustrator  
 Allart, R., Bourrier, V., Lovis, C., et al. 2018, *Sci*, 362, 1384  
 Allart, R., Pino, L., Lovis, C., et al. 2020, *A&A*, 644, A155  
 Alonso-Floriano, F. J., Snellen, I. A. G., Czesla, S., et al. 2019, *A&A*, 629, A110  
 Astropy Collaboration, Price-Whelan, A. M., Sipőcz, B. M., et al. 2018, *AJ*, 156, 123  
 Barber, R. J., Tennyson, J., Harris, G. J., & Tolchenov, R. N. 2006, *MNRAS*, 368, 1087  
 Barton, E. J., Yurchenko, S. N., & Tennyson, J. 2013, *MNRAS*, 434, 1469  
 Bean, J. L., Raymond, S. N., & Owen, J. E. 2021, *JGRE*, 126, e06639  
 Beaugé, C., & Nesvorný, D. 2013, *ApJ*, 763, 12  
 Bello-Arufe, A., Buchhave, L. A., Mendonça, J. M., et al. 2022, *A&A*, 662, A51  
 Bello-Arufe, A., Cabot, S. H. C., Mendonça, J. M., Buchhave, L. A., & Rathcke, A. D. 2021, *AJ*, 163, 96  
 Birkby, J. L. 2018, arXiv:1806.04617  
 Bourrier, V., Lecavelier des Etangs, A., Ehrenreich, D., et al. 2018, *A&A*, 620, A147  
 Bourrier, V., Lecavelier des Etangs, A., & Vidal-Madjar, A. 2015, *A&A*, 573, A11  
 Bower, D. J., Kitzmann, D., Wolf, A. S., et al. 2019, *A&A*, 631, A103  
 Brogi, M., de Kok, R. J., Albrecht, S., et al. 2016, *ApJ*, 817, 106  
 Burrows, A., Ram, R. S., Bernath, P., Sharp, C. M., & Milsom, J. A. 2002, *ApJ*, 577, 986  
 Cabot, S. H. C., Bello-Arufe, A., Mendonça, J. M., et al. 2021, *AJ*, 162, 218  
 Cabot, S. H. C., Madhusudhan, N., Hawker, G. A., & Gandhi, S. 2019, *MNRAS*, 482, 4422  
 Cabot, S. H. C., Madhusudhan, N., Welbanks, L., Piette, A., & Gandhi, S. 2020, *MNRAS*, 494, 363  
 Casasayas-Barris, N., Pallé, E., Yan, F., et al. 2018, *A&A*, 616, A151  
 Casasayas-Barris, N., Pallé, E., Yan, F., et al. 2019, *A&A*, 628, A9  
 Caulley, P. W., Redfield, S., & Jensen, A. G. 2017, *AJ*, 153, 217  
 Caulley, P. W., Redfield, S., Jensen, A. G., & Barman, T. 2016, *AJ*, 152, 20  
 Caulley, P. W., Shkolnik, E. L., Ilyin, I., et al. 2019, *AJ*, 157, 69  
 Caulley, P. W., Wang, J., Shkolnik, E. L., et al. 2021, *AJ*, 161, 152  
 Changeat, Q., & Edwards, B. 2021, *ApJL*, 907, L22  
 Chen, G., Casasayas-Barris, N., Pallé, E., et al. 2020, *A&A*, 635, A171  
 Christie, D., Arras, P., & Li, Z.-Y. 2013, *ApJ*, 772, 144  
 Clough, S. A., Iacono, M. J., & Moncet, J.-L. 1992, *JGR*, 97, 15761  
 Czesla, S., Klocová, T., Khalafinejad, S., Wolter, U., & Schmitt, J. H. M. M. 2015, *A&A*, 582, A51  
 Czesla, S., Lampón, M., Sanz-Forcada, J., et al. 2022, *A&A*, 657, A6  
 Czesla, S., Schröter, S., Schneider, C. P., et al. 2019, PyA: Python astronomy-related packages, Astrophysics Source Code Library, ascl:1906.010  
 de Kok, R. J., Brogi, M., Snellen, I. A. G., et al. 2013, *A&A*, 554, A82  
 Ehrenreich, D., Bourrier, V., Wheatley, P. J., et al. 2015, *Natur*, 522, 459  
 Ekenbäck, A., Holmström, M., Wurz, P., et al. 2010, *ApJ*, 709, 670  
 Foreman-Mackey, D., Hogg, D. W., Lang, D., & Goodman, J. 2013, *PASP*, 125, 306  
 Fossati, L., Shulyak, D., Sreejith, A. G., et al. 2020, *A&A*, 643, A131  
 Fulton, B. J., & Petigura, E. A. 2018, *AJ*, 156, 264  
 Fulton, B. J., Petigura, E. A., Howard, A. W., et al. 2017, *AJ*, 154, 109  
 Futaana, Y., Chaufray, J.-Y., Smith, H. T., et al. 2011, *SSRv*, 162, 213  
 Gaidos, E., Kitzmann, D., & Heng, K. 2017, *MNRAS*, 468, 3418  
 García Muñoz, A. 2007, *P&SS*, 55, 1426  
 García Muñoz, A., & Schneider, P. C. 2019, *ApJL*, 884, L43  
 Gaudi, B. S., Stassun, K. G., Collins, K. A., et al. 2017, *Natur*, 546, 514  
 Gray, R. O., & Corbally, C. J. 1994, *AJ*, 107, 742  
 Grimm, S. L., Malik, M., Kitzmann, D., et al. 2021, *ApJS*, 253, 30  
 Grisel, O., Mueller, A., Buitinck, L., et al. 2021, scikit-learn/scikit-learn:scikit-learn v0.24.2, Zenodo doi:10.5281/zenodo.591564  
 Gullikson, K., Dodson-Robinson, S., & Kraus, A. 2014, *AJ*, 148, 53  
 Harris, C. R., Millman, K. J., van der Walt, S. J., et al. 2020, *Natur*, 585, 357  
 Heng, K. 2016, *ApJL*, 826, L16  
 Hoeijmakers, H. J., Ehrenreich, D., Heng, K., et al. 2018, *Natur*, 560, 453  
 Hoeijmakers, H. J., Ehrenreich, D., Kitzmann, D., et al. 2019, *A&A*, 627, A165  
 Holmström, M., Ekenbäck, A., Selsis, F., et al. 2008, *Natur*, 451, 970  
 Hooton, M. J., Watson, C. A., de Mooij, E. J. W., Gibson, N. P., & Kitzmann, D. 2018, *ApJL*, 869, L25  
 Howe, A. R., Adams, F. C., & Meyer, M. R. 2020, *ApJ*, 894, 130  
 Huang, C., Arras, P., Christie, D., & Li, Z.-Y. 2017, *ApJ*, 851, 150  
 Hunter, J. D. 2007, *CSE*, 9, 90  
 John, T. L. 1988, *A&A*, 193, 189  
 Khalafinejad, S., von Essen, C., Hoeijmakers, H. J., et al. 2017, *A&A*, 598, A131  
 King, G. W., & Wheatley, P. J. 2021, *MNRAS*, 501, L28  
 Kirk, J., Alam, M. K., López-Morales, M., & Zeng, L. 2020, *AJ*, 159, 115  
 Kirk, J., Dos Santos, L. A., López-Morales, M., et al. 2022, *AJ*, 164, 24  
 Kitzmann, D., Heng, K., Rimmer, P. B., et al. 2018, *ApJ*, 863, 183  
 Knutson, H. A., Charbonneau, D., Burrows, A., O'Donovan, F. T., & Mandushev, G. 2009, *ApJ*, 691, 866  
 Kreidberg, L. 2015, *PASP*, 127, 1161  
 Kubyskhina, D. 2022, *AN*, 343, e10077  
 Kubyskhina, D., Vidotto, A. A., Villarreal D'Angelo, C., et al. 2022, *MNRAS*, 510, 2111  
 Kurucz, R. L. 2017, *CajPh*, 95, 825  
 Lammer, H., Selsis, F., Ribas, I., et al. 2003, *ApJL*, 598, L121  
 Lavie, B., Ehrenreich, D., Bourrier, V., et al. 2017, *A&A*, 605, L7  
 Lecavelier Des Etangs, A., Ehrenreich, D., Vidal-Madjar, A., et al. 2010, *A&A*, 514, A72  
 Louden, T., & Wheatley, P. J. 2015, *ApJL*, 814, L24  
 Lundkvist, M. S., Kjeldsen, H., Albrecht, S., et al. 2016, *NatCo*, 7, 11201  
 Madhusudhan, N. 2019, *ARA&A*, 57, 617  
 Mansfield, M., Bean, J. L., Oklopcic, A., et al. 2018, *ApJL*, 868, L34  
 Mansfield, M., Bean, J. L., Stevenson, K. B., et al. 2020, *ApJL*, 888, L15  
 Mazeh, T., Holzer, T., & Faigler, S. 2016, *A&A*, 589, A75  
 McKemmish, L. K., Masseron, T., Hoeijmakers, H. J., et al. 2019, *MNRAS*, 488, 2836  
 McKemmish, L. K., Yurchenko, S. N., & Tennyson, J. 2016, *MNRAS*, 463, 771  
 McLaughlin, D. B. 1924, *ApJ*, 60, 22  
 Mitani, H., Nakatani, R., & Yoshida, N. 2022, *MNRAS*, 512, 855  
 Murray-Clay, R. A., Chiang, E. I., & Murray, N. 2009, *ApJ*, 693, 23  
 Ninan, J. P., Stefansson, G., Mahadevan, S., et al. 2020, *ApJ*, 894, 97  
 Odert, P., Erkaev, N. V., Kislyakova, K. G., et al. 2020, *A&A*, 638, A49  
 Owen, J. E. 2019, *AREPS*, 47, 67  
 Owen, J. E., & Jackson, A. P. 2012, *MNRAS*, 425, 2931  
 Owen, J. E., Murray-Clay, R. A., Schreyer, E., et al. 2023, *MNRAS*, 518, 4357–4371  
 Pai Asnodkar, A., Wang, J., Gaudi, B. S., et al. 2022, *AJ*, 163, 40  
 Perryman, M. 2018, *The Exoplanet Handbook* (2nd ed.) (Cambridge: Cambridge Univ. Press)  
 Pino, L., Désert, J.-M., Brogi, M., et al. 2020, *ApJL*, 894, L27  
 Rogers, J. G., & Owen, J. E. 2021, *MNRAS*, 503, 1526  
 Rossiter, R. A. 1924, *ApJ*, 60, 15  
 Salz, M., Czesla, S., Schneider, P. C., et al. 2018, *A&A*, 620, A97  
 Seager, S., & Deming, D. 2010, *ARA&A*, 48, 631  
 Snellen, I. A. G., Albrecht, S., de Mooij, E. J. W., & Le Poole, R. S. 2008, *A&A*, 487, 357  
 Snellen, I. A. G., de Kok, R. J., de Mooij, E. J. W., & Albrecht, S. 2010, *Natur*, 465, 1049  
 Spake, J. J., Sing, D. K., Evans, T. M., et al. 2018, *Natur*, 557, 68  
 Stevenson, K. B. 2016, *ApJL*, 817, L16  
 Stevenson, K. B., Désert, J.-M., Line, M. R., et al. 2014, *Sci*, 346, 838  
 Stock, J. W., Kitzmann, D., Patzer, A. B. C., & Sedlmayr, E. 2018, *MNRAS*, 479, 865  
 Szentgyorgyi, A. H., & Fűrész, G. 2007, *RMxAC*, 28, 129  
 Turner, J. D., de Mooij, E. J. W., Jayawardhana, R., et al. 2020, *ApJL*, 888, L13  
 Van Eylen, V., Agentoft, C., Lundkvist, M. S., et al. 2018, *MNRAS*, 479, 4786

- Venturini, J., Guilera, O. M., Haldemann, J., Ronco, M. P., & Mordasini, C. 2020, [A&A](#), **643**, L1
- Vidal-Madjar, A., Lecavelier des Etangs, A., Désert, J. M., et al. 2003, [Natur](#), **422**, 143
- Virtanen, P., Gommers, R., Oliphant, T. E., et al. 2020, [NatMe](#), **17**, 261
- Waskom, M. 2021, [JOSS](#), **6**, 3021
- Wong, I., Shporer, A., Kitzmann, D., et al. 2020, [AJ](#), **160**, 88
- Wytttenbach, A., Ehrenreich, D., Lovis, C., Udry, S., & Pepe, F. 2015, [A&A](#), **577**, A62
- Wytttenbach, A., Mollière, P., Ehrenreich, D., et al. 2020, [A&A](#), **638**, A87
- Yadin, B., Veness, T., Conti, P., et al. 2012, [MNRAS](#), **425**, 34
- Yan, F., & Henning, T. 2018, [NatAs](#), **2**, 714
- Yan, F., Casasayas-Barris, N., Molaverdikhani, K., et al. 2019, [A&A](#), **632**, A69
- Yan, F., Wytttenbach, A., Casasayas-Barris, N., et al. 2021, [A&A](#), **645**, A22
- Yelle, R. V. 2004, [Icar](#), **170**, 167
- Yurchenko, S. N., Sinden, F., Lodi, L., et al. 2018, [MNRAS](#), **473**, 5324
- Yurchenko, S. N., & Tennyson, J. 2014, [MNRAS](#), **440**, 1649
- Žák, J., Kabáth, P., Boffin, H. M. J., Ivanov, V. D., & Skarka, M. 2019, [AJ](#), **158**, 120
- Zhou, G., & Bayliss, D. D. R. 2012, [MNRAS](#), **426**, 2483
- Zhou, G., Latham, D. W., Bieryla, A., et al. 2016, [MNRAS](#), **460**, 3376

### 3.2 LINKS AND IMPLICATIONS

Please refer to Section 6.1.2 in Chapter 6 to understand how this paper has contributed towards the exoplanet community.

# CHAPTER 4: PAPER 2: TWO MINI-NEPTUNES TRANSITING THE ADOLESCENT K-STAR HIP 113103 CONFIRMED WITH *TESS* AND *CHEOPS*.

## 4.1 INTRODUCTION

SUB-NEPTUNES ARE VITAL exoplanets to observe, for in addition to being the most common sub-class, they will also reveal insight towards the potential evolutionary pathways between rocky Earth analogues to gaseous Neptunian analogues. In this work, we present the first detection of two sub-Neptunes, HIP 113103 b and HIP 113103 c orbiting around the adolescent ( $470^{+170}_{-110}$  Myr using Gyrochronology from Bouma et al., 2023) K-star HIP 113103. These planets were first identified through *TESS*, followed by ground-based photometric and spectroscopic observations. Given the near 2:1 resonance of the system, we obtained additional photometry using *CHEOPS* to observe both planets within a  $\sim 17.5$  hour window, as its precision was required to confirm both planets, particularly HIP 113103 b.

OUR RESULTS DETECTED A planetary radius of  $R_p = 1.829^{+0.096}_{-0.067} R_\oplus$  for HIP 113103 b (placing it within the sparsely populated radius valley) and  $R_p = 2.40^{+0.10}_{-0.08} R_\oplus$  for HIP 113103 c . The brightness of the HIP 113103 (K = 7.557 mag) combined with the close proximity and high equilibrium temperature of both planets ( $P = 7.610303$  days,  $T_{eq} = 721 \pm 10$  K for HIP 113103 b and  $P = 14.245648$  days,  $T_{eq} = 585 \pm 10$  K for HIP 113103 c), makes the HIP 113103 system one of the few suitable K-star systems capable for atmospheric follow up. We simulated what this might look like if observed using *Twinkle*, *HST*, and *JWST* given cloudy and clear atmosphere scenarios in chemical equilibrium using the retrieval software TauREx 3.0.



## Two mini-Neptunes transiting the adolescent K-star HIP 113103 confirmed with *TESS* and *CHEOPS*

N. Lowson<sup>1</sup>,<sup>1\*</sup> G. Zhou,<sup>1\*</sup> C. X. Huang,<sup>1</sup> D. J. Wright,<sup>1</sup> B. Edwards,<sup>2</sup> E. Nabbie,<sup>1</sup> A. Venner<sup>1</sup>,<sup>1</sup> S. N. Quinn,<sup>3</sup> K. A. Collins,<sup>3</sup> E. Gillen<sup>4,5,6</sup>, M. Battley,<sup>7</sup> A. Triaud<sup>8</sup>, C. Hellier,<sup>9</sup> S. Seager,<sup>10,11,12</sup> J. N. Winn,<sup>13</sup> J. M. Jenkins,<sup>14</sup> B. Wohler,<sup>14,15</sup> A. Shporer,<sup>10</sup> R. P. Schwarz,<sup>3</sup> F. Murgas,<sup>16,17</sup> E. Pallé,<sup>16,17</sup> D. R. Anderson<sup>18,19</sup>, R. G. West<sup>18,19</sup>, R. A. Wittenmyer,<sup>1</sup> B. P. Bowler,<sup>20</sup> J. Horner<sup>1</sup>, S. R. Kane,<sup>21</sup> J. Kielkopf<sup>22</sup>, P. Plavchan<sup>23</sup>, H. Zhang,<sup>24</sup> T. Fairnington,<sup>1</sup> J. Okumura,<sup>1</sup> M. W. Mengel<sup>1</sup> and B. C. Addison<sup>1</sup>

*Affiliations are listed at the end of the paper*

Accepted 2023 September 2. Received 2023 August 28; in original form 2023 May 19

### ABSTRACT

We report the discovery of two mini-Neptunes in near 2:1 resonance orbits ( $P = 7.610303$  d for HIP 113103 b and  $P = 14.245651$  d for HIP 113103 c) around the adolescent K-star HIP 113103 (TIC 121490076). The planet system was first identified from the *TESS* mission, and was confirmed via additional photometric and spectroscopic observations, including a  $\sim 17.5$  h observation for the transits of both planets using ESA *CHEOPS*. We place  $\leq 4.5$  min and  $\leq 2.5$  min limits on the absence of transit timing variations over the 3 yr photometric baseline, allowing further constraints on the orbital eccentricities of the system beyond that available from the photometric transit duration alone. With a planetary radius of  $R_p = 1.829_{-0.067}^{+0.096} R_\oplus$ , HIP 113103 b resides within the radius gap, and this might provide invaluable information on the formation disparities between super-Earths and mini-Neptunes. Given the larger radius  $R_p = 2.40_{-0.08}^{+0.10} R_\oplus$  for HIP 113103 c, and close proximity of both planets to HIP 113103, it is likely that HIP 113103 b might have lost (or is still losing) its primordial atmosphere. We therefore present simulated atmospheric transmission spectra of both planets using *JWST*, *HST*, and *Twinkle*. It demonstrates a potential metallicity difference (due to differences in their evolution) would be a challenge to detect if the atmospheres are in chemical equilibrium. As one of the brightest multi sub-Neptune planet systems suitable for atmosphere follow up, HIP 113103 b and HIP 113103 c could provide insight on planetary evolution for the sub-Neptune K-star population.

**Key words:** techniques: photometric – techniques: spectroscopic – planets and satellites: detection – stars: individual: TIC121490076.

### 1 INTRODUCTION

Super-Earths ( $1 R_\oplus < R_p \leq 1.5 R_\oplus$ ) and mini-Neptunes ( $1.5 R_\oplus < R_p \leq 4 R_\oplus$ ) are the most common planets found around sun-like stars (referred to as sub-Neptunes hereafter), especially those residing in close-in orbits (Howard et al. 2012; Fressin et al. 2013; Bergsten et al. 2022), despite having no analogues in our own Solar System. These planets bridge the gap between rocky Earth-like worlds and gaseous Neptunes (e.g. Fulton et al. 2017). The *Transiting Exoplanet Survey Satellite* (*TESS*; Ricker et al. 2015) mission continues to expand our repertoire for sub-Neptunes, in particular those orbiting bright nearby stars. These discoveries have led to precise radius and mass constraints for a significant number of sub-Neptunes (e.g. Dragomir et al. 2019; Gandolfi et al. 2019; Cloutier et al. 2020; MacDougall et al. 2021; Sozzetti et al. 2021; Gan et al. 2022; Lubin et al. 2022),

as well as the possibility of in-depth atmospheric characterizations that reveal the origins and evolutionary pathways of this population (e.g. Osborn et al. 2021; Kawauchi et al. 2022).

Hypothesized planet formation pathways for sub-Neptunes [see Bean, Raymond & Owen (2021) for more information] will exhibit observable differences that are accessible with the new generation of space and ground based facilities (e.g. Greene et al. 2016; Tinetti et al. 2018). Depending on what occurs after dissipation of the gas disc, sub-Neptunes may not contain enough mass to gravitationally maintain their primordial atmosphere (e.g. Walker 1986; Lopez, Fortney & Miller 2012; Ginzburg, Schlichting & Sari 2018; Kite & Barnett 2020; Kite et al. 2020). The rate of mass-loss post-formation is strongly dependent on the irradiation the planets receive from their host stars. Planets receiving strong XUV irradiation may be more likely to lose their primordial envelope (e.g. Owen & Jackson 2012; Howe & Burrows 2015; Mordasini 2020; Ketzner & Poppenhaeger 2022).

The next generation space-based telescopes [commencing with the *James Webb Space Telescope* (*JWST*); Greene et al. (2016)] will

\* E-mail: natalia.lowson@unisq.edu.au (NL); george.zhou@unisq.edu.au (GZ)

be capable of characterizing the atmospheres of sub-Neptunes, and many are prioritizing wavelength regions towards the infrared (e.g. Tinetti et al. 2018; Stotesbury et al. 2022). Obstruction by haze and clouds are minimized at longer wavelengths, and early *JWST* observations have already demonstrated its invaluable retrieval capabilities for exoplanets atmospheres (e.g. Ahrer et al. 2023; Alderson et al. 2023; Feinstein et al. 2023; Rustamkulov et al. 2023; Tsai et al. 2023). Prior to the launch of these next generation telescopes, some attempts of measuring sub-Neptune atmospheres have resulted in observations obscured by haze (e.g. Kreidberg et al. 2014; Mugnai et al. 2021); however, there have been notable exceptions which suggest predominant H/He envelopes (e.g. Benneke et al. 2019; Tsiaras et al. 2019; Edwards et al. 2022; Orell-Miquel et al. 2022). Due to their size, observing sub-Neptune atmospheres is challenging in comparison to their larger Jovian counterparts, particularly around FGK stars. Therefore, the most suitable population of sub-Neptunes for atmosphere analysis are those residing in close orbits to bright host stars. In the known FGK planet population, there are only a handful of sub-Neptunes that meet these requirements (e.g. Winn et al. 2011; Gandolfi et al. 2018; Dragomir et al. 2019; Teske et al. 2020), with samples dwindling further when only considering multisub-Neptune planet systems (e.g. Rodriguez et al. 2018; Delrez et al. 2021; Scarsdale et al. 2021; Barragán et al. 2022). It is therefore vital to identify sub-Neptunes with short periods around bright stars, as these candidates will lead the research towards understanding the formation pathways of this vast sub-class.

In this paper, we report the discovery of two sub-Neptunes that orbit at a 2:1 resonance around the bright K-star HIP 113103 (TIC 121490076). The initial observations with *TESS* and subsequent follow up with the *Characterising Exoplanets Satellite* (*CHEOPS*; Benz et al. 2021) and ground-based facilities are outlined in Section 2, while our global model fit to constrain the physical parameters of each planet are outlined in Section 3. The physical properties of HIP 113103 are discussed in Section 4, while the elimination of false positive scenarios are outlined in Section 5. Our Results and Discussion are presented in Section 6 followed by our Conclusion in Section 7, respectively.

## 2 OBSERVATIONS

### 2.1 Candidate identification with *TESS*

The transiting planets around HIP 113103 were first identified by observations from *TESS*. Observations for HIP 113103 were obtained via the 30 min cadence Full Frame Images (FFI) from Sector 1 Camera 2, and via 10 min FFIs and 2 min target pixel stamps from Sector 28 Camera 2.

The transit signals around HIP 113103 were identified as part of a search for planets around young active field stars (Zhou et al. 2021) via public FFI light curves from the MIT Quick look pipeline (Huang et al. 2020a, b). The target star was identified as a potential young star via its high amplitude rotational modulation using the 10 min FFI light curves from Sector 28. The combined FFI light curves of Sector 1 and 28 were first modeled and detrended via a spline interpolation (Vanderburg & Johnson 2014), and searched for transit signals via the box-least-squared (BLS) procedure (Kovács, Zucker & Mazeh 2002). Two candidate signals are detected by BLS, one at  $\approx 7.61$  d with a signal to noise of 14, the other at  $\approx 14.24$  d with a signal to noise of 12.79. Both signals crossed the recommended threshold to be classified as a threshold crossing event (TCE) as defined by the *TESS* Objects of Interest (TOI) team (Guerrero et al. 2021). We vetted the data for both TCEs to rule out astrophysical false positives

due to blending from nearby eclipsing binaries outside of the centre pixel. We found that transit depth derived from different apertures are similar, and found no obvious blending sources when examining light curves from individual pixels in and around the aperture. We then promoted both TCEs for further follow up via *CHEOPS* (Section 2.2) and ground based instruments (Sections 2.3 and 2.4).

To refine the orbital and physical characteristics of the planets in our global model (Section 3), we use of the debelended Sector 28 target pixel stamp (TPF) 2-min cadence Simple Aperture Photometry (SAP) light curves (Twicken et al. 2010; Morris et al. 2020), performing the debrending using the contamination keywords in the TPF files. These light curves originate from the Science Processing Operations Center (SPOC; Jenkins et al. 2016) at NASA Ames Research Center, and are made available via the the Mikulski Archive for Space Telescopes (MAST).<sup>1</sup> HIP 113103 exhibits significant rotational modulation due to spot activity on the stellar surface. To ensure proper propagation of the uncertainties associated with these noise sources, we model the rotational modulation and spacecraft systematics alongside the transiting planet signals. We use the debelended simple aperture SPOC light curves in this simultaneously detrending procedure. Following Vanderburg et al. (2019), we describe these signals as a linear combination of the spacecraft quarternions, the top seven covariant basis vectors, and a set of 20 cosine and sine functions at frequencies up to the *TESS* orbital period of 13 d (also see Mazeh & Faigler 2010; Huang, Bakos & Hartman 2013). Fig. 1 shows the *TESS* discovery light curve before and after the removal of the stellar and instrumental effects, while Fig. 2 and Fig. 3, 3, 4 show the individual transit light curves centred at HIP 113103 b and HIP 113103 c respectively. Fig. 4 shows the phase folded *TESS* transit light curves for each planet.

### 2.2 *CHEOPS* follow-up photometry

Although we detected HIP 113103 b and HIP 113103 c through *TESS*, additional observations with higher precision are required to confirm and constrain the radius and ephemerides values for both planets. We therefore use the *CHEOPS* mission to observe the primary transit of both planets during a single observing window. *CHEOPS* is a visible to infrared (0.4  $\mu\text{m}$  – 1.1  $\mu\text{m}$ ) 0.32-m Ritchey–Chrétien telescope located in a 700-km geocentric Sun-synchronous orbit. It is capable of capturing high-precision photometry of exoplanets around bright stars, with the corresponding *CHEOPS* mission focusing on the radius refinement of super-Earths and sub-Neptunes (Benz et al. 2021).

The *CHEOPS* observation (observation ID: 1901592) was obtained between 2022 September 9 20:31 and 2022 September 10 14:06 UTC (10 orbits over  $\sim 17.5$  h), with a  $\sim 5$  h baseline between ingress and egress of both transits. At an exposure time of 60 s, 700 frames are obtained, with 10 frames affected by stray light and Earth occultation. This observation of a near-simultaneous transit for HIP 113103 b and HIP 113103 c was possible only because of the near 2:1 resonance of the system.

The low Earth orbit nadir-locked orientation of *CHEOPS* naturally induces field rotation over the course of a spacecraft-orbit, and results in correlated systematics in the observed light curve. We modelled these effects alongside the transit model as part of our global modelling (Section 3). The spacecraft signals are modelled as a linear combination of the sky background, smear, contamination, pixel X and Y drifts, and a set of four sine and cosine functions at

<sup>1</sup><https://archive.stsci.edu/>

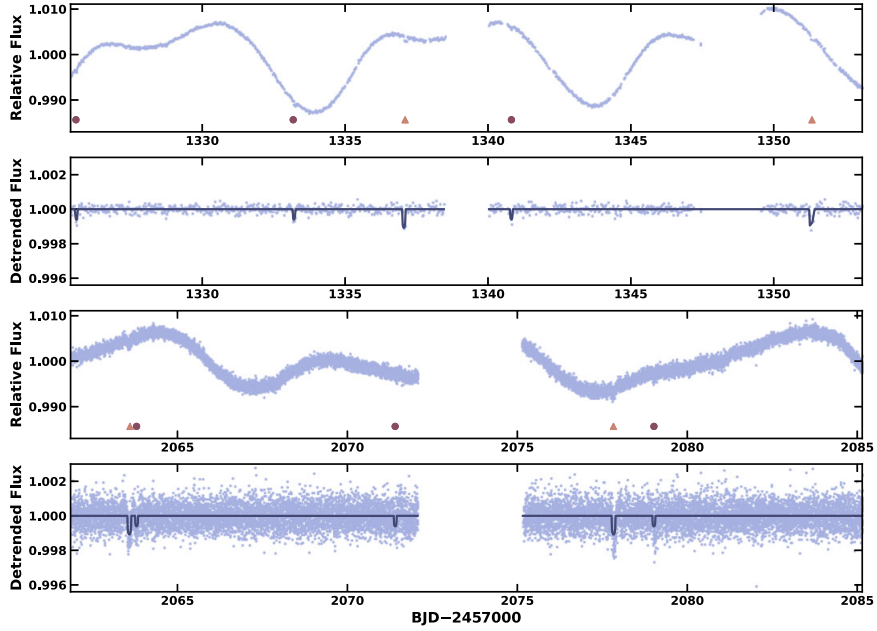


**Figure 1.** The *TESS* light curves before and after the removal of spot modulated rotational signals. The light curves of HIP 113103 from Sector 1 via FFI observations were observed at 30 min cadence (Panels 1 and 2), and from Sector 28 TPF observations at 2 min (Panels 3 and 4). Transits by HIP 113103 b and HIP 113103 c are illustrated via a circle and triangle respectively. The best-fitting transit model is displayed in navy.

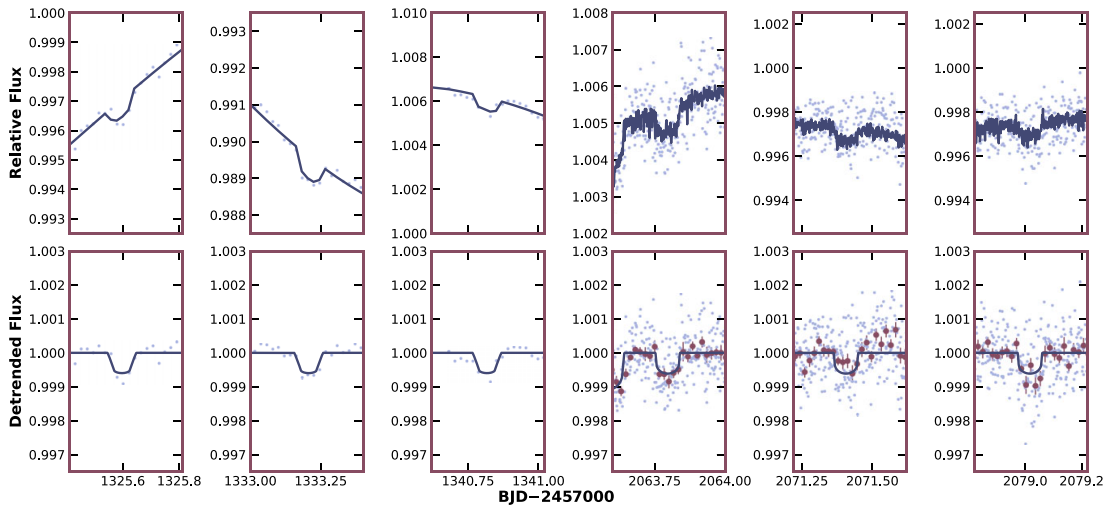


**Figure 2.** The *TESS* light curves centred on the transits of HIP 113103 b. The top panel shows the pre-detrending, the bottom panel shows the post-detrending light curves, after the removal of spot modulated rotational signal from HIP 113103. Columns 1–3 were observed at 30-min cadence during Sector 1, while 4–6 were observed at 2-min cadence from Sector 28. The best-fitting transit model is displayed in navy, and the detrended transits at 2-min cadence have been binned in 10-min intervals to illustrate the precision of *TESS*.

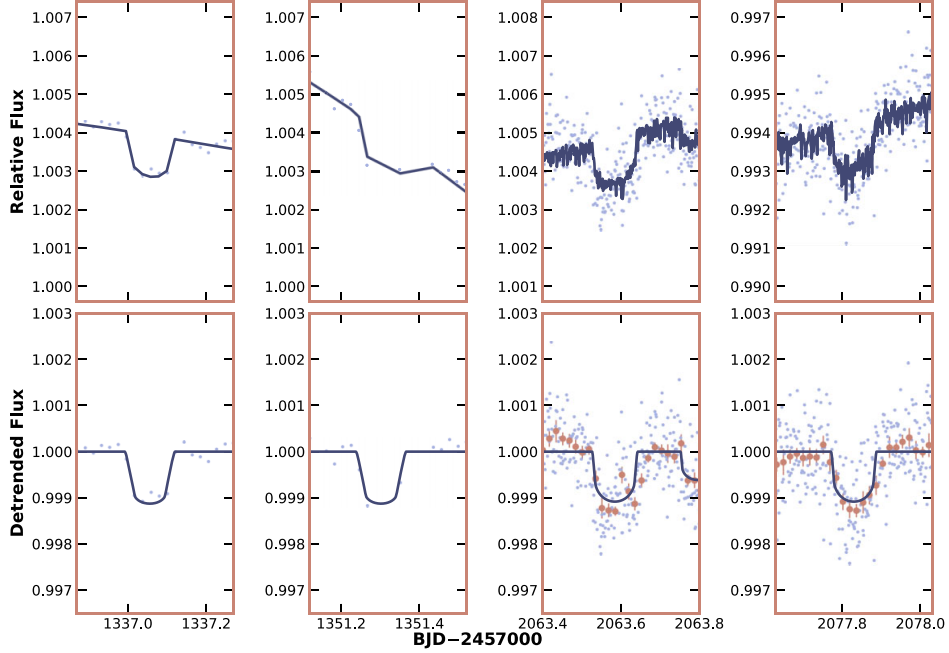


**Figure 3.** The *TESS* light curves centred on the transits of HIP 113103 c. The top panel shows the pre-detrending, the bottom shows the post-detrending light curve, after the removal of spot modulated rotational signal from HIP 113103. Columns 1–2 were observed at 30-min cadence during Sector 1, while 3–4 were observed at 2-min cadence during Sector 28. The best-fitting transit model is displayed in navy, and the detrended transits at 2-min cadence have been binned in 10-min intervals to illustrate the precision of *TESS*.

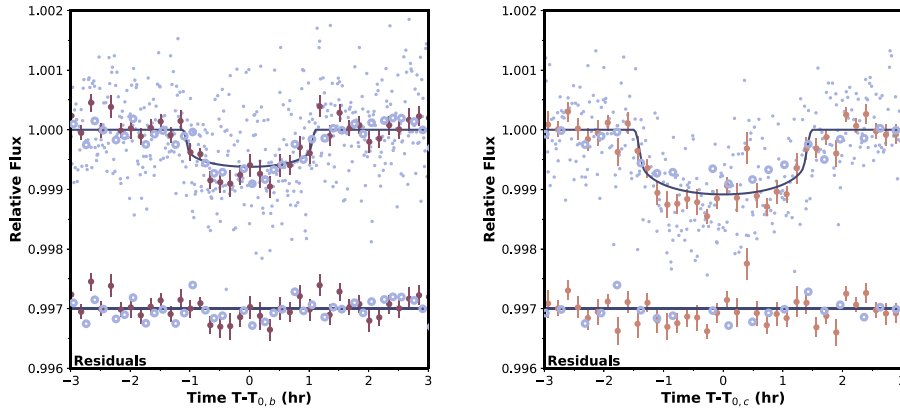


**Figure 4.** Phase folded *TESS* transit light curves for HIP 113103 b (left) and HIP 113103 c (right). The light blue open circles represent 30-min cadenced observations, while the light blue filled points represent the 2-min cadenced observations. The points with error bars show the binned 2-min light curves at 10-min cadence. The best-fitting models are over plotted. The binned residuals are plotted at the bottom, vertically offset by 0.003 in flux for clarity.

frequencies up to four times the spacecraft orbital period as a function of the spacecraft roll angle.

Fig. 5 shows the raw and detrended *CHEOPS* light curves, and the model describing the instrumental signals that were removed from the raw light curve.

### 2.3 Ground-based follow-up photometry

In addition to space-based observations, we also obtained ground-based seeing limited photometry through the *TESS* Follow-up Observing Program (TFOP) photometry science working group (SG1)

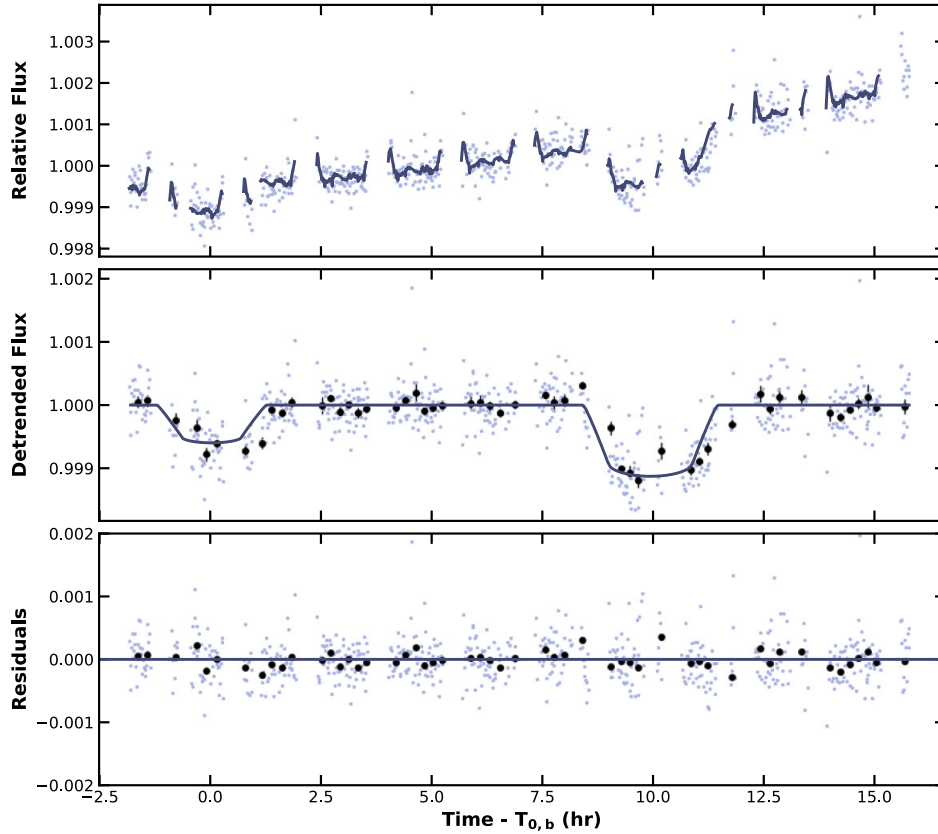


**Figure 5.** The follow-up *CHEOPS* observations of HIP 113103 b (first transit) and HIP 113103 c (second transit) taken over a single  $\sim 17.5$  h visit. The top panel displays the raw light curves from the optimal aperture extraction. The model describing the planetary transits and the instrumental effects is overplotted via the navy line (see Section 3). The middle panel shows the detrended *CHEOPS* light curve after removal of the instrumental spacecraft orbit induced variations and the best-fitting transit model. The transits are binned in 10-min intervals to illustrate the precision of *CHEOPS*. The bottom panel illustrates the residuals of the data.

to detect the transits of both planets and further rule out other nearby targets contaminating the detection.

Two transits of both HIP 113103 b and HIP 113103 c were obtained using the Las Cumbres Observatory Global Telescope (LCOGT Brown et al. 2013) facility. We used the 1-m telescopes of the LCOGT network for these observations. Each telescope is equipped with a *sinistro* 4 K  $\times$  4 K and/or EM CCD camera, yielding a field of view of 5.7 arcmin and a pixel scale of  $0.34'' \text{ pixel}^{-1}$ . These observations are able to detect the transits of both planets with high significance, and determine that the transit depths are consistent with those derived from *TESS* and *CHEOPS*. The images were calibrated using the standard LCOGT BANZAI pipeline (McCully et al. 2018) and the differential photometric data was extracted using ASTROIMAGEJ (Collins et al. 2017). Given *Gaia* DR3 catalogue shows that no other stars are within 10 arcsec of HIP 113103, we determine that the transit signals most likely originated from the target star. The light curves are detrended simultaneously against the airmass in our global fit. Fig. 6 shows the detrended light curves against their respective model light curve from our global model fit. The observations are detailed as follows:

A full transit of HIP 113103 b was obtained via the 1-m telescope at the South African Astronomical Observatory (SAAO) on UT 2022-09-09 with a 5.5 arcsec radius aperture using the  $z_s$  filter. On UT 2022-09-10, a partial transit of HIP 113103 c, including ingress, was obtained from the Cerro Tololo Interamerican Observatory (CTIO) node with a 6.2 arcsec radius aperture using the  $z_s$  filter. An additional full transit for both HIP 113103 b and HIP 113103 c were obtained from the CTIO node on UT 2022-09-10 and UT 2022-10-22. Both transits were obtained with the  $z_s$  filter, with an aperture size of 8.2 arcsec and 7.0 arcsec for HIP 113103 b and HIP 113103 c, respectively. Table 1 displays all the photometric transit observations analysed in this work.

#### 2.4 Spectroscopic characterization

To characterize the stellar properties of the host star and validate the planetary-nature of the transiting candidates, we obtained a series of reconnaissance spectroscopic observations of HIP 113103 with a set of southern spectroscopic facilities.

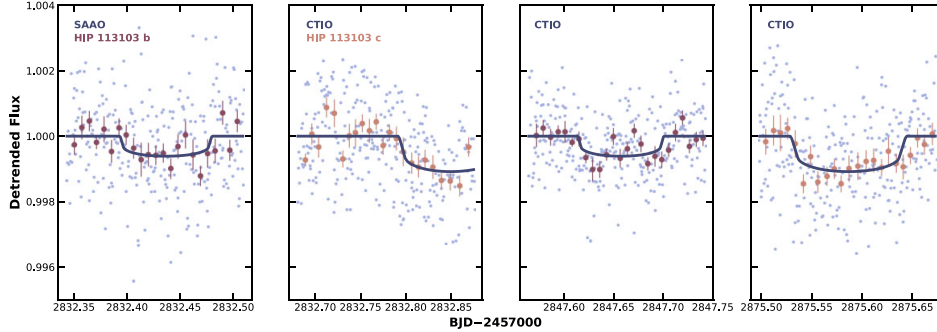


**Figure 6.** The ground-based detrended photometric follow-up observations of HIP 113103 b and HIP 113103 c, as obtained with the Las Cumbres Observatory 1-m telescopes at the South African Astronomical Observatory and the Cerro Tololo Interamerican Observatory (all in  $z_s$  filter). The best-fitting transit model is represented via the navy line, while each transit has been binned in 10-min intervals to illustrate the precision of the *LCO* telescopes.

**Table 1.** A summary of all ground-based photometric transit observations for HIP 113103 b and HIP 113103 c.

Target	Instrument	Date (UT)	Filter	Aperture
HIP 113103 b	SAAO 1.0 m	2022-09-09	$z_s$	5.5 arcmin
HIP 113103 c	CTIO 1.0 m	2022-09-10	$z_s$	6.2 arcmin
HIP 113103 b	CTIO 1.0 m	2022-09-25	$z_s$	8.2 arcmin
HIP 113103 c	CTIO 1.0 m	2022-10-22	$z_s$	7.0 arcmin

These instruments are involved in the LCOGT consortium.

The stellar atmospheric parameters were derived by matching each observation against a library of  $\sim 10\,000$  observed spectra previously classified through the Spectroscopic Classification Pipeline (Buchhave et al. 2012). The library is interpolated via a gradient boosting regressor model, from which the best-fitting spectral parameters were determined (Zhou et al. 2021). We found a best-fitting effective temperature of  $T_{\text{eff}} = 4930 \pm 100$  K, surface gravity of  $\log g = 4.6 \pm 0.1$  dex, metallicity of  $[\text{m}/\text{H}] = -0.1 \pm 0.1$  dex, and projected rotational broadening of  $v \sin i_* = 3 \pm 1$  km s $^{-1}$  for HIP 113103. We note that the rotational velocity is less than the instrument broadening, and the reported value is likely an upper limit of the true rotation velocity.

In addition, we obtained eight observations of HIP 113103 using the CHIRON facility on the SMARTS 1.5-m telescope located at Cerro Tololo Inter-American Observatory, Chile (Tokovinin et al. 2013). CHIRON is a fibre-fed echelle spectrograph with a resolving power of  $R \sim 80\,000$  over the wavelength range of 4100–8700 Å. We use the extracted spectra from CHIRON reduced via the standard pipeline as per Paredes et al. (2021). The radial velocities are derived from each observation via a least-squares deconvolution of the spectra against a synthetic template generated at the atmospheric parameters of the target star (Donati et al. 1997). The generated line profiles are modelled via a combination of kernels describing the rotational, macroturbulent, and instrument broadening effects (following Gray & Corbally 1994).

We also obtained 10 epochs of spectroscopic observations from the MINERVA-Australis array. MINERVA-Australis is an array of four identical 0.7-m telescopes, located at Mt Kent Observatory, Australia. The light from all four telescopes are combined into a single KIWIPEC high resolution echelle spectrograph, with a resolving power of  $R \sim 80\,000$  over the wavelength region of 4800–6200 Å (Barnes et al. 2012; Addison et al. 2019). Wavelength corrections are provided by

**Table 2.** Radial velocity measurements of HIP 113103.

BJD	RV (km s $^{-1}$ )	$\sigma_{\text{RV}}$ (km s $^{-1}$ )	Instrument
2459171.60440	12.813	0.035	CHIRON
2459174.59126	12.864	0.024	CHIRON
2459176.58998	12.824	0.022	CHIRON
2459178.62741	12.858	0.026	CHIRON
2459180.55586	12.818	0.029	CHIRON
2459182.53304	12.830	0.034	CHIRON
2459184.55875	12.854	0.026	CHIRON
2459186.62126	12.877	0.022	CHIRON
2459917.93684	13.370	0.022	MINERVA-Australis
2459917.95510	13.425	0.019	MINERVA-Australis
2459924.93091	13.377	0.015	MINERVA-Australis
2459924.94916	13.382	0.020	MINERVA-Australis
2459930.93397	13.356	0.038	MINERVA-Australis
2459930.95226	13.406	0.020	MINERVA-Australis
2459942.92801	13.384	0.019	MINERVA-Australis
2459942.94630	13.407	0.018	MINERVA-Australis
2460046.29239	13.435	0.035	MINERVA-Australis
2460046.31065	13.409	0.014	MINERVA-Australis

two simultaneous fibers adjacent to the object fibers, which pass light from a quartz lamp through an iodine cell. Relative radial velocities are derived by a cross correlation between each individual observation and an averaged spectrum of the set of spectra available for the target. These relative velocities are then shifted to the mean absolute velocity of the averaged spectrum. These velocities are also presented in Table 2.

The MINERVA-Australis observations have per-point uncertainties of 10–20 m s $^{-1}$ , and are comparable to those obtained from CHIRON. We do not detect significant radial velocity variations at the 20 m s $^{-1}$  level, consistent with the expected low mass of the planets around HIP 113103. The observations therefore remain consistent with a lack of detection of the radial velocity orbit, as is expected given the velocity uncertainties and the expected orbit amplitude. The line profiles exhibit no visible variations indicative of blend scenarios. In scenarios where the transit is induced by a background eclipsing binary, we would often observe correlations between the rotational broadening velocity and the radial velocities, with the apparent broadening at its maximum at the extremities of the velocity curve. We observe no such correlation for HIP 113103, with the exposure to exposure scatter in the rotational broadening of 0.2 km s $^{-1}$ .

**Table 3.** The physical properties of HIP 113103.

Parameter	Value	Source
<b>Identifiers</b>	HIP 113 103 TIC 121 490 076 TYC 8011-00766-1 2MASS J22541736-4300372 Gaia DR2 6 541 360 574 788 758 016	
<b>Astrometry</b>		
RA	22 <sup>h</sup> 54 <sup>m</sup> 17 <sup>s</sup> .37	Gaia Collaboration (2022)
Dec.	−43°00′37″.25	Gaia Collaboration (2022)
Parallax (mas)	21.61785 ± 0.00024	Gaia Collaboration (2022)
<b>Proper motion</b>		
Gaia (2016.4) RA proper motion (mas yr <sup>−1</sup> )	1.995 ± 0.020	Gaia Collaboration (2022)
Gaia (2016.3) Dec. proper motion (mas yr <sup>−1</sup> )	27.384 ± 0.021	Gaia Collaboration (2022)
Hipparcos (1991.2) RA proper motion (mas yr <sup>−1</sup> )	2.2 ± 1.5	Perryman et al. (1997)
Hipparcos (1991.4) Dec. proper motion (mas yr <sup>−1</sup> )	27.1 ± 1.3	Perryman et al. (1997)
Hipparcos-Gaia average RA proper motion (mas yr <sup>−1</sup> )	2.032 ± 0.048	Brandt (2021)
Hipparcos-Gaia average Dec. proper motion (mas yr <sup>−1</sup> )	27.396 ± 0.038	Brandt (2021)
<b>Photometry</b>		
TESS (mag)	8.9988 ± 0.0063	Stassun et al. (2019)
B (mag)	10.907 ± 0.033	Høg et al. (2000)
V (mag)	9.95 ± 0.03	Høg et al. (2000)
J (mag)	8.195 ± 0.03	Skrutskie et al. (2006)
H (mag)	7.67 ± 0.042	Skrutskie et al. (2006)
K (mag)	7.557 ± 0.031	Skrutskie et al. (2006)
Gaia G (mag)	9.6175 ± 0.0018	Gaia Collaboration (2022)
Gaia <sub>BP</sub> (mag)	10.1491 ± 0.0033	Gaia Collaboration (2022)
Gaia <sub>RP</sub> (mag)	8.9353 ± 0.0039	Gaia Collaboration (2022)
WISE W1 (mag)	7.398 ± 0.033	Cutri & et al. (2012)
WISE W2 (mag)	7.538 ± 0.02	Cutri & et al. (2012)
WISE W3 (mag)	7.489 ± 0.017	Cutri & et al. (2012)
WISE W4 (mag)	7.395 ± 0.132	Cutri & et al. (2012)
<b>Kinematics and position</b>		
U (km s <sup>−1</sup> )	5.00 ± 0.17	Propagated from Gaia <sup>1</sup>
V (km s <sup>−1</sup> )	4.635 ± 0.031	Propagated from Gaia <sup>1</sup>
W (km s <sup>−1</sup> )	−13.89 ± 0.32	Propagated from Gaia <sup>1</sup>
Distance (pc)	46.212 ± 0.086	This paper
$\gamma_{\text{CHIRON}}$ (km s <sup>−1</sup> )	12.845 <sup>+0.012</sup> <sub>−0.013</sub>	This paper
$\gamma_{\text{MINERVA}}$ (km s <sup>−1</sup> )	13.395 <sup>+0.010</sup> <sub>−0.011</sub>	This paper
Jitter <sub>CHIRON</sub> (m s <sup>−1</sup> )	16 <sup>+20</sup> <sub>−11</sub>	This paper
Jitter <sub>MINERVA</sub> (m s <sup>−1</sup> )	13 <sup>+14</sup> <sub>−9</sub>	This paper
<b>Physical properties</b>		
$M_*$ (M <sub>⊙</sub> )	0.761 ± 0.038	This paper
$R_*$ (R <sub>⊙</sub> )	0.742 ± 0.013	This paper
$T_{\text{eff}}$ (K)	4930 ± 100	This paper
log g (cgs)	4.6 ± 0.1	This paper
[m/H]	−0.1 ± 0.1	This paper
$v \sin i$ (km s <sup>−1</sup> )	3 ± 1	This paper
Rotation period (d)	9.92 ± 0.23	This paper
Gyrochronology age (Myr)	470 <sup>+170</sup> <sub>−110</sub>	Based on the gyrochronology relationship from Bouma, Palumbo & Hillenbrand (2023)
Limb darkening coefficients (TESS <sub>u1</sub> )	0.463 ± 0.021	Claret (2017)
Limb darkening coefficients (TESS <sub>u2</sub> )	0.182 ± 0.020	Claret (2017)
Limb darkening coefficients (CHEOPS <sub>u1</sub> )	0.604 ± 0.021	Claret & Bloemen (2011)
Limb darkening coefficients (CHEOPS <sub>u2</sub> )	0.111 ± 0.022	Claret & Bloemen (2011)
Limb darkening coefficients (LCO z' band <sub>u1</sub> )	0.350 ± 0.021	Claret & Bloemen (2011)
Limb darkening coefficients (LCO z' band <sub>u2</sub> )	0.287 ± 0.021	Claret & Bloemen (2011)

<sup>1</sup> Propagated from *Gaia* via the GAL UVW function in the PYASTRONOMY package (Czesla et al. 2019).

In addition, two archival spectra were obtained from the European Southern Observatory (ESO) HARPS facility on the ESO 3.6-m telescope in La Silla, Chile (Mayor et al. 2003). The observations have a spectral resolution of  $R = 120\,000$  over the spectral range

of 3780–6910 Å. We make use of the two archival observations, obtained in 2010 and 2013, to further classify the host star atmospheric properties. To calculate the spectroscopic parameters, we make use of the ZASPE package (Brahm et al. 2017) and its associated

**Table 4.** Derived parameters for HIP 113 103 b and HIP 113 103 c.

Parameter	Value	Prior
<b>Fitted parameters for HIP 113103 b</b>		
$T_0$ (BJD-TDB) .....	$1325.5966^{+0.0033}_{-0.0024}$	Fitted
$P$ (days) .....	$7.610303 \pm 0.000018$	Fitted
$R_p/R_*$ ( $R_*$ ) .....	$0.0242^{+0.0013}_{-0.0008}$	Fitted
$i$ (deg) .....	$88.23^{+0.18}_{-0.14}$	Fitted
$\sqrt{e} \cos \omega$ .....	$0.18^{+0.51}_{-0.45}$	Fitted
$\sqrt{e} \sin \omega$ .....	$-0.12^{+0.31}_{-0.32}$	Fitted
<b>Inferred parameters for HIP 113103 b</b>		
$e$ .....	$0.17^{+0.17}_{-0.13}$	Derived
$\omega$ (deg) .....	$-10^{+120}_{-140}$	Derived
$R_p$ ( $R_\oplus$ ) .....	$1.829^{+0.096}_{-0.067}$	Derived
$a/R_*$ ( $R_*$ ) .....	$21.39^{+0.10}_{-0.13}$	Derived
$a$ (au) .....	$0.06899^{+0.00029}_{-0.00023}$	Derived
$T_{14}$ (days) .....	$0.0891^{+0.0075}_{-0.0068}$	Derived
$T_{\text{eq}}$ (K) .....	$721 \pm 10$	Derived
$b$ .....	$0.656^{+0.070}_{-0.084}$	Derived
$(R_p/R_*)^2$ .....	$0.000596^{+0.000062}_{-0.000051}$	Derived
$M_p$ ( $M_\oplus$ ) from mass–radius relationships .....	$5.9 \pm 1.9^*$	Inferred
$K_{\text{RV}}$ ( $\text{m s}^{-1}$ ) from mass–radius relationships .....	$2.34 \pm 0.73^*$	Inferred
$\rho_p$ ( $\rho_\oplus$ ) from mass–radius relationships .....	$0.96^{+0.15}_{-0.22}$	Inferred
<b>Fitted parameters for HIP 113103 c</b>		
$T_0$ (BJD-TDB) .....	$1337.0559 \pm 0.0019$	Fitted
$P$ (days) .....	$14.245648 \pm 0.000019$	Fitted
$R_p/R_*$ ( $R_*$ ) .....	$0.0303^{+0.0014}_{-0.0010}$	Fitted
$i$ (deg) .....	$89.24^{+0.40}_{-0.22}$	Fitted
$\sqrt{e} \cos \omega$ .....	$-0.31^{+0.23}_{-0.25}$	Fitted
$\sqrt{e} \sin \omega$ .....	$0.21^{+0.13}_{-0.18}$	Fitted
<b>Inferred parameters for HIP 113103 c</b>		
$e$ .....	$0.17^{+0.17}_{-0.13}$	Derived
$\omega$ (deg) .....	$-70^{+100}_{-60}$	Derived
$R_p$ ( $R_\oplus$ ) .....	$2.40^{+0.10}_{-0.08}$	Derived
$a/R_*$ ( $R_*$ ) .....	$32.49^{+0.15}_{-0.19}$	Derived
$a$ (au) .....	$0.10479^{+0.00045}_{-0.00035}$	Derived
$T_{14}$ (days) .....	$0.1764^{+0.0091}_{-0.0050}$	Derived
$T_{\text{eq}}$ (K) .....	$585 \pm 10$	Derived
$b$ .....	$0.614^{+0.028}_{-0.063}$	Derived
$(R_p/R_*)^2$ .....	$0.001051^{+0.00011}_{-0.000087}$	Derived
$M_p$ ( $M_\oplus$ ) from mass–radius relationships .....	$8.4 \pm 1.9^*$	Inferred
$K_{\text{RV}}$ ( $\text{m s}^{-1}$ ) from mass–radius relationships .....	$2.67 \pm 0.58^*$	Inferred
$\rho_p$ ( $\rho_\oplus$ ) from mass–radius relationships .....	$0.60^{+0.054}_{-0.091}$	Inferred

Values denoted with an asterisk were calculated using an estimated mass derived from the method outlined in Wolfgang, Rogers & Ford (2016), as described in Section 6.1. For  $T_{\text{eq}}$ , we assume a  $A_B = 0$ .

custom spectral library computed from the Castelli & Kurucz (2004) model atmospheres. We find a mean effective temperature of  $T_{\text{eff}} = 4800 \pm 60$  K, surface gravity of  $\log g = 4.47 \pm 0.05$  dex, and metallicity of  $[\text{m}/\text{H}] = 0.0 \pm 0.05$  dex, with uncertainties adapted from the uncertainty floor as per Brahm et al. (2017). We do not incorporate the HARPS observations towards our spectroscopic parameters due to the sample being too small. We instead adopt the CHIRON and MINERVA-Australis spectra for our spectroscopic parameters, as we were able to test the self consistency of our parameters via its scatter from spectrum to spectrum (as presented in Table 3).

In addition, as the HARPS spectra cover the Calcium H&K lines, we also make use of the two available spectra to compute activity indices for HIP 113103. We followed the same procedure as per the Mt Wilson catalogue (Vaughan, Preston & Wilson 1978; Wilson 1978; Duncan et al. 1991; Baliunas et al. 1995), and compute the S-index via a set of photometric band passes about the line cores and continuum around each line. The S-index is then converted to the  $\log R'_{\text{HK}}$  index as per Noyes et al. (1984). We found a mean Calcium HK activity of  $\log R'_{\text{HK}} = -4.69 \pm 0.05$  from the two HARPS observations, indicating minimal chromospheric activity being exhibited by the host star (Henry et al. 1996).

### 3 GLOBAL MODEL

In order to constrain the stellar and planetary properties of the HIP 113 103 system, we performed a global model fit using all the observations outlined in Section 2. Our global model is similar to that implemented in previous papers (e.g. Zhou et al. 2022), and was tested against other publicly available codes such as EXOFASTV2 in Rodriguez et al. (2017). Free parameters fitted for include orbital parameters defining the orbital eccentricity  $\sqrt{e} \cos \omega$  and  $\sqrt{e} \sin \omega$  (where  $e$  is eccentricity and  $\omega$  is argument of periapsis), line-of-sight inclination  $i$ , orbital period  $P$ , radius ratio  $R_p/R_*$ , and transit midpoint  $T_0$ . The photometric transits are modeled via BATMAN (Kreidberg 2015) as per Mandel & Agol (2002), simultaneously incorporating an associated instrument model to account for additional variability induced by external factors. This includes fitting for a polynomial accounting for the influence of spacecraft on the photometric fluxes for CHEOPS as per Maxted et al. (2022), described in Section 2.2. Similarly, we also fit for linear coefficients to the mean, standard deviation, and skew terms of the three quarters for TESS as per Vanderburg et al. (2019). Ground based LCO photometry were simultaneously detrended against airmass to remove hours time-scale variability in the baseline. Limb darkening coefficients are interpolated from the CHIRON stellar atmospheric parameters for the host star via Claret & Bloemen (2011) and Claret (2017), and constrained by Gaussian priors with widths of 0.02. The width of the Gaussian prior is set by the uncertainties in the models, and by the propagated uncertainties from the spectroscopically derived stellar parameters. We also trialled the same global model, but with Gaussian priors of width 0.1 for the limb darkening parameters and note no significant changes to our model posteriors. Supersampling corrections of the light curve model has been applied where necessary when modelling the 30-min cadenced observations (Kipping 2010). The CHIRON and MINERVA-Australis radial velocities were modeled via the RADVEL package (Fulton et al. 2018), accounting for their respective instrumental offsets and velocity jitter terms.

To jointly model the stellar properties, we interpolate the MIST isochrones (Dotter 2016) along age, stellar mass, and metallicity, with outputs of stellar radius and absolute magnitudes in a set of photometric bands as is made available by the public isochrone files. The spectral energy distribution and *Gaia* parallax provide the tightest observational constraints on the host star properties. At each iteration, we include jump parameters for age, host star mass  $M_*$ , metallicity [M/H], and parallax. The parallax of the target is strongly constrained by a Gaussian prior about that measured by *Gaia* DR3 (Gaia Collaboration 2022), with a correction of  $-0.025657$  mas applied according to Lindgren et al. (2021). We compare the interpolated MIST absolute magnitudes against that of the observed *Hipparcos* TYCHO  $B$ , and  $V$ , 2MASS  $J$ ,  $H$ , and  $K$ , and the *Gaia*  $G$ ,  $B_p$ , and  $R_p$  bands (Perryman et al. 1997; Skrutskie et al. 2006; Gaia Collaboration 2018) magnitudes, after correcting for the distance modulus via the parallax jump parameter. In addition to the absolute magnitudes, we also interpolate the MIST isochrones along stellar radius, which is then incorporated into modelling of the transit parameters, such as  $a/R_*$ .

We constrained our models using a Markov chain Monte Carlo analysis via EMCEE (Foreman-Mackey et al. 2013), with 400 walkers over 4000 iterations per walker (with the first 2000 iterations allocated to burn in). Informative priors are summarised in Table 4, while all other fitted parameters are constrained by uniform priors bounded by their physical limits. The derived planetary and stellar values are presented in Tables 4 and 3, respectively. Fig. 1 shows our output model for our TESS data set, Fig. 5 for CHEOPS, and Fig. 6 for ground based photometric follow-up observations.

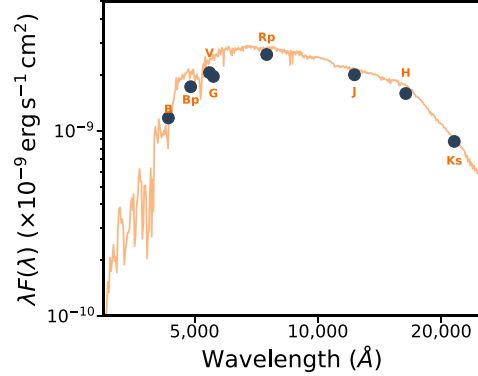


**Figure 7.** Spectral energy distribution of HIP 113103. We make use of the spectroscopic atmospheric priors and the photometric magnitudes of HIP 113103 to constrain the stellar properties simultaneous to our global modeling of the stellar and planetary parameters.

### 4 STELLAR ROTATION AND AGE

The TESS light curve of HIP 113103 exhibits significant quasi-periodic variability at the 0.5 per cent level representative of rotational variability. Fig. 7 shows the auto-correlation function of the periodicity over the two TESS sectors. We found a rotation period of  $10.2 \pm 1.4$  d from Sector 1, and  $10.0 \pm 1.3$  d from Sector 28 observations. The uncertainties were estimated by taking the width of the best-fitting Gaussian to the periodogram peaks. The rotation period is consistent between the two sectors, spanning 1 yr in separation.

In addition, HIP 113103 also received 1 yr of observations from the Wide Angle Search for Planets (WASP) Consortium (Pollacco et al. 2006) with the Southern SuperWASP facility, located at the Sutherland Station of the SAAO. The SuperWASP observatory consists of eight Canon 200-mm f/1.8 telephoto lenses, yielding a  $7.8^\circ \times 7.8^\circ$  field of view each over a  $2K \times 2K$  detector. SuperWASP observations of HIP 113103 spanned 2006-05-07 to 2007-11-13, yielding  $\sim 11000$  epochs of observations. The periodogram from the SuperWASP light curves are also overplotted in Fig. 8, yielding a rotation period of  $9.90 \pm 0.23$  d, consistent with the TESS observations more than a decade later. When combined, the TESS and WASP data sets provide a long term stable rotation period of  $9.92 \pm 0.23$  d for HIP 113103. In addition, we make use of the measured rotational velocity  $v \sin i_*$ , and the photometric rotation period to provide a  $1\sigma$  lower limit for the stellar inclination angle of  $i_* > 56^\circ$  (Masuda & Winn 2020), consistent with an aligned geometry. Using  $R_* = 0.742 \pm 0.013 R_\odot$  and  $P_{\text{rot}} = 9.92 \pm 0.23$  d, we also calculate an equatorial velocity of  $V_{\text{eq}} = 3.78 \pm 0.11 \text{ km s}^{-1}$ , which is in good agreement with our  $v \sin i_*$  value of  $3 \pm 1 \text{ km s}^{-1}$ .

The rotation period of HIP 113103 is consistent with an adolescent K dwarf. We adopt the rotation sequence interpolation presented by Bouma et al. (2023), and derive a rotation-based age of  $470_{-110}^{+170}$  Myr at  $1\sigma$  significance. Similarly, based on the rotation age relationship from Mamajek & Hillenbrand (2008), the  $1\sigma$  age range for HIP 113103 is 380–510 Myr. However, gyrochronology is particularly insecure in estimating the ages of single K dwarfs. The spins of these stars may stall within the first billion years, and many around giga-year clusters exhibit similar rotation periods (e.g. Meibom, Mathieu & Stassun 2009; Agüeros et al. 2018; Douglas et al. 2019). Angus et al. (2015) accounts for a larger spread in the spin-down

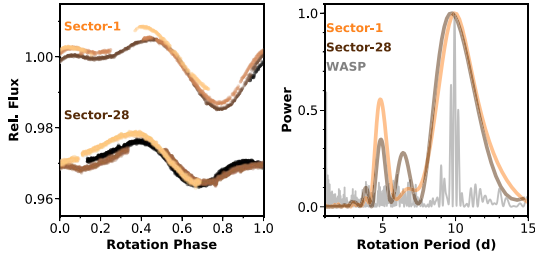


**Figure 8.** Spectral energy distribution of HIP 113103. We make use of the spectroscopic atmospheric priors and the photometric magnitudes of HIP 113103 to constrain the stellar properties simultaneous to our global modeling of the stellar and planetary parameters. HIP 113103 exhibits significant spot-induced rotational variability in its light curves. Left: *TESS* light curves from Sectors 1 and 28 folded to the rotation period of HIP 113103; each rotation cycle is plotted in a progressively lighter shade. The sectors are separated by an arbitrary vertical offset. HIP 113103 maintains a constant rotation period over the multiyear observations obtained by *TESS*. Right: Autocorrelation periodograms of the *TESS* and SuperWASP light curves of HIP 113103, showing a consistent peak at 10.0 d over the course of more than 10 yr.

dispersion of low mass stars, and the relationship they provide yields a  $1\sigma$  age range of 200–2000 Myr for HIP 113103. HIP 113103 lacks spectroscopic features, such as Li 6708 Å absorption and significant Calcium II H&K emission that are usually indicative of youth, as is expected for K dwarfs older than  $\sim 300$  million yr (Fig. 7). The Calcium II H&K derived index  $\log R_{\text{HK}} = -4.69 \pm 0.05$  corresponds to an age of  $1.9^{+0.7}_{-0.5}$  Gyr, consistent with the rotational derived age estimate. In addition, the isochrone modelling also provides a loose age constraint of  $5 \pm 2$  Gyr at the  $1\sigma$  level. We find no evidence that HIP 113103 is kinematically associated with comoving stars via the COMOVE package (Tofflemire et al. 2021).<sup>2</sup> It is therefore difficult to confirm the suspected youth of HIP 113103.

## 5 INVESTIGATING FALSE POSITIVE SCENARIOS

When identifying a new planetary system, it is important to carefully consider the possibilities of astrophysical and instrumental false positives.

When analysing beyond the *TESS* observations, HIP 113103 b and HIP 113103 c are detected with high significance on multiple instruments, yielding consistent transit depth and duration and thus sufficiently ruling out the scenario that the transit signals result from instrument false alarms of the *TESS* spacecraft.

We use the following steps to rule out various astrophysical false positive scenarios. We can determine that either HIP 113103 b or HIP 113103 c are not eclipsing binaries around HIP 113103 using radial velocity observations taken with CHIRON as outlined in Section 2.4. There were no detections of significant radial velocity variations at the  $20 \text{ m s}^{-1}$  level, ruling out stellar mass objects at the orbital period of the transit signals.

We then follow Seager & Mallén-Ornelas (2003) to use the transit shapes to constrain the probability that the transit signals were mimicked by a binary system blended with the HIP 113103. The maximum magnitude of an eclipsing binary that can produce a transit

with similar shape can be estimated by

$$\Delta M \lesssim 2.5 \log_{10} \left( \frac{t_{12}^2}{t_{13}^2 \delta} \right)^2, \quad (1)$$

where  $t_{12}$  represents the ingress duration, and  $t_{13}$  represent the time between the first and the third contact of the transit.

We model the transit shape of both planets independently using the *TESS* and *CHEOPS* light curves without putting any priors on the stellar parameters. We found the  $3\sigma$   $T_{\text{mag}}$  upper limit of any background stars capable of producing these transit signals are 13 ( $\Delta M < 4.23$  mag) and 12 ( $\Delta M < 3.06$  mag) for HIP 113103 b and HIP 113103 c, respectively.

We rule out an hierarchical binary system associated with HIP 113103, satisfying the above criteria. Neither CHIRON nor the HARPS observations (Section 2.4) detected secondary spectra lines, indicating no slow rotating, spectroscopic blended companions at  $\Delta M < 4$  (Zhou et al. 2021).

For non-associated background binaries, we can use the *Gaia* DR3 catalogue to rule out stars brighter than our magnitude limit up to 1 arcmin away from HIP 113103. There are no stars within 20 arcsec of HIP 113 103 based on *Gaia* DR3 catalogue. We estimate the density of stars brighter than our magnitude limit within 1 arcmin of HIP 113103 (which may be unresolved) by following the procedure described in Zhou et al. (2021). We found that the chance of finding a random star in the direction of HIP 113103 with  $\Delta M < 4.2$  and  $\Delta M < 3$  are  $3 \times 10^{-5}$  and  $1 \times 10^{-5}$ .

Taken together, the combined observations that the system hosts multiple planets, the box-shaped transits, and the lack of additional stars in the spectra and background give us high confidence that HIP 113103 b and HIP 113103 c are genuine planets.

We also conducted a statistical validation on the *TESS* observations using the TRICERATOPS package (Giacalone et al. 2021), the false positive probability (FPP) yielded 0.052 for HIP 113103 b and 0.026 for HIP 113103 c. The Nearby Star FPP (NFPP) for both planets is 0. The main contributor to the FPP is the scenario that a transiting planet with the same period is around an unresolved secondary star (known as STP). We have high confidence that CHIRON and HARPS spectra can rule out secondary stars in the same system within  $\Delta \text{mag}$  of 4, which is the magnitude limit to cause a transit given the transit shape constraints. The rest of false positive scenario have total FPP less than  $1e-3$ , therefore we can confidently call both candidates planets.

## 6 RESULTS AND DISCUSSION

### 6.1 Planet properties

We statistically validate the planetary nature of the HIP 113103 system, with the best-fitting planetary parameters presented in Table 4. HIP 113103 b has a radius of  $R_p = 1.829^{+0.096}_{-0.067} R_{\oplus}$ , placing it in the upper bound of the radius gap, a small population of planets within the radii bounds  $1.5 R_{\oplus} < R_p \leq 2 R_{\oplus}$  which may be the transition point from super-Earths to mini-Neptunes via photoevaporation-driven mass loss (Fulton et al. 2017). HIP 113103 c has a radius of  $R_p = 2.40^{+0.10}_{-0.08} R_{\oplus}$ , and an equilibrium temperature of  $585 \pm 10$  K, making it a warm mini-Neptune.

We compare the HIP 113103 system with other K stars hosting multisub-Neptune planets with  $T_{\text{eq}} \leq 750$  K in (Fig. 9), evaluating the transmission spectroscopy metric (TSM) for each target (Kempton et al. 2018). Due to the relative brightness of HIP 113103 ( $V \sim 10$  mag) and high equilibrium temperatures, HIP 113103 b (TSM = 53) and HIP 113103 c (TSM = 68) are the second most suited system around a K star for atmosphere characterization [only succeeded

<sup>2</sup><https://github.com/adamkraus/Comove>

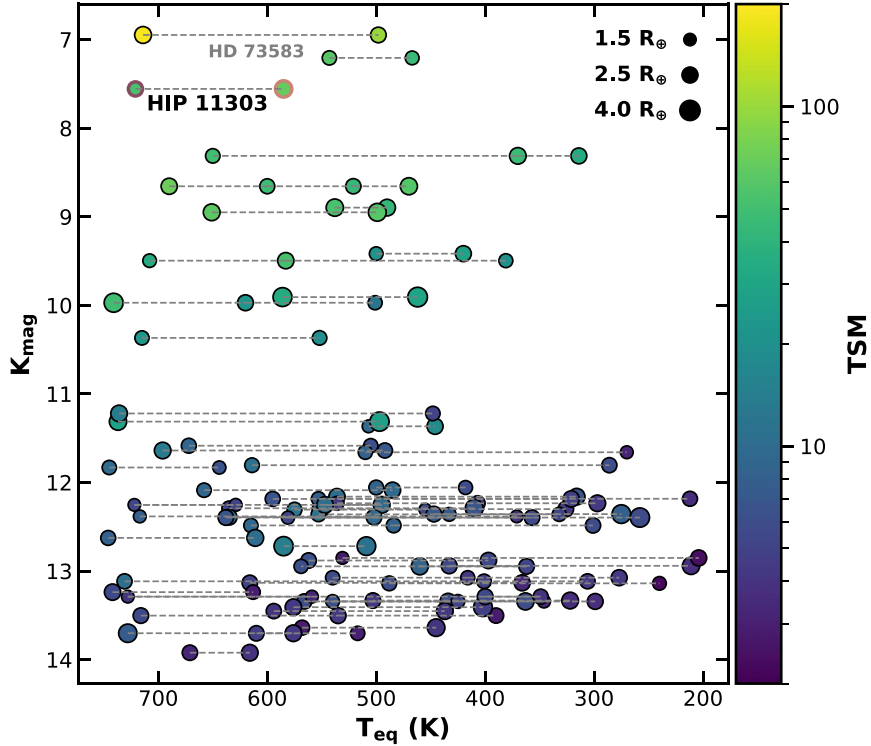


**Figure 9.** The HIP 11303 system in the context of other multiplanet systems. Specifically, we show multiplanet systems hosting two or more warm Neptunes or super-Earths with equilibrium temperature  $T_{\text{eq}} \leq 750$  K, orbiting K stars as a function of their equilibrium temperature and K-band magnitude. The dashed lines connect each planet within the respective planetary system. The HIP 11303 system orbits one of the brightest K-dwarf host stars, and are promising candidates for follow up atmospheric observations. The colour bar illustrating the TSM for each planet places the HIP 11303 system as second highest suitable for atmosphere analysis, behind the HD 73 583 system (Barragán et al. 2022).

by the HD 73 583 system (Barragán et al. 2022)], and therefore invaluable targets to understand how multisub-Neptune systems might evolve around K-stars. This stellar population is optimal for radial velocity due to its brightness in comparison to planets orbiting M-dwarfs (Neil & Rogers 2018; Rojas-Ayala 2023). This aids the detection of smaller planets around a stellar population that shares similar characteristics to G-stars (Howard et al. 2012). Additionally from an atmosphere analysis perspective, K-stars have had repeated success at hosting planets with absorption at the He I 10 830 Å line, a tracer associated with atmosphere evaporation (Nortmann et al. 2018; Allart et al. 2019; Guilluy et al. 2020; Fu et al. 2022). Although the TSM values for HIP 113103 b and HIP 113103 c are below the J-band priority threshold of 90 (for targets within the  $1.5 R_{\oplus} \leq R_p \leq 10 R_{\oplus}$ ), the derived radii of the planets combined with their close proximity to HIP 113103, and its Gyrochronological age make it a valuable system to explore through atmosphere analysis.

To estimate the mass of both planets to gauge the feasibility of future follow-up observations, we adopt the mass–radius relationship from Wolfgang et al. (2016). We estimate  $M_p = 5.9 \pm 1.9 M_{\oplus}$  for HIP 113103 b and  $M_p = 8.4 \pm 1.9 M_{\oplus}$  for HIP 113103 c. These correspond to radial velocity semi-major amplitudes of  $2.34 \text{ m s}^{-1}$  and  $2.67 \text{ m s}^{-1}$ , respectively. Additional analysis using the Echelle SPectrograph for Rocky Exoplanets and Stable Spectroscopic Ob-

servations (ESPRESSO; Pepe et al. 2021) instrument on the Very Large Telescope (VLT) to understand this system in greater detail is currently underway.

## 6.2 Transit timing variations

We search for transit timing variations (TTVs), indicative of interactions between the two planets, or the presence of additional companions. To derive accurate transit times for each event, we perform an additional global model of the system, as per Section 3, where the transit epoch of each transit event is a free variable, and the period is held fixed. The resulting transit times are displayed in Fig. 10. We find no evidence for deviations from a linear ephemeris propagation larger than 4.5 (resp. 2.5) min ( $1\sigma$  scatter) for HIP 113103 b (resp. c). The mean timing uncertainty per transit is 5.7 (resp. 3.3) min, consistent with the measured scatter. We estimated the expected TTV amplitude for the system using TTVFASTER (Agol & Deck 2016). Given the pair of planets has a period ratio within 10 percent of the 2:1 mean motion resonance, we can estimate that if the planets are on modest eccentric orbits or are relatively massive, they are highly likely to exhibit TTVs with amplitudes detectable by our observations. In detail, if both planets are of Neptune mass ( $\sim 17 M_{\oplus}$ ), and we assume relatively low eccentricities follow a Rayleigh distribution

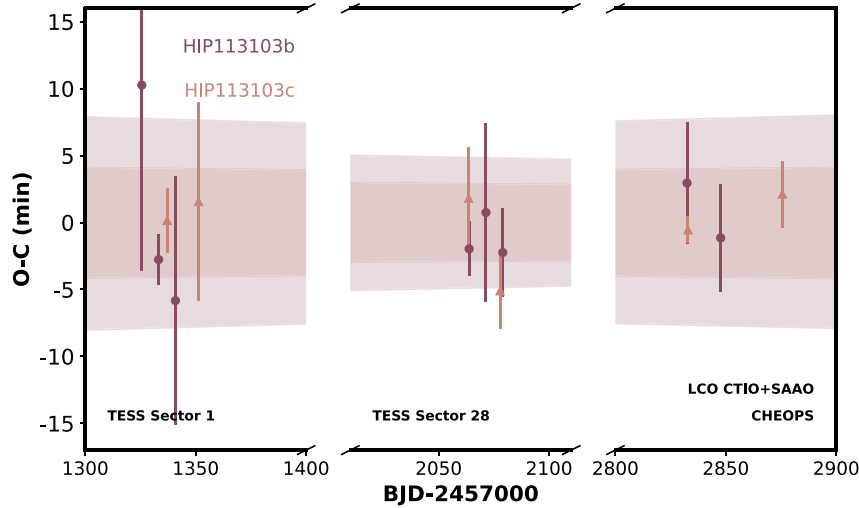


**Figure 10.** Deviations from linear transit times for individual transits of HIP 113103 b (circle markers) and HIP 113103 c (triangle markers) from all photometric observations, with each facility identified via labels along the time axis. Using our global fitted  $T_0$  values to serve as the linear baseline for HIP 113103 b and HIP 113103 c, we show that over a 4-yr period, the transit midpoint for each target does not vary beyond  $\sim 10$  min shaded regions denote the  $1\sigma$  propagated transit timing uncertainties for each respective planet. Note that the individual transit times are fully consistent with the linear transit ephemeris.

with  $\sigma_e = 0.06$  (consequent mean eccentricity,  $\bar{e} = 0.075$ ), the median TTV scatter for HIP 113103 b (resp. HIP 113103 c) should be on the 10 (resp. 15) min time-scale (Jurić & Tremaine 2008). If we adopt masses for both planets as per the mass–radius relationship from Wolfgang et al. (2016), TTVFASTER estimates that the eccentricity of the system is most likely lower than 0.2 given the non-detection of a significant TTV signal. This puts tighter constraints on the system eccentricity compared to our global modeling. This eccentricity upper limit is derived by comparing the scatter in the transit times from TTVFASTER simulations and the observed data. We first compute the 3 sigma scatter of the transit times from the data set presented in Fig. 10. We then compute the corresponding eccentricities of the systems that would produce larger transit time deviations in 95 per cent of the simulations.

95% (2)

### 6.3 Prospect for atmospheric follow-up

Systems hosting transiting small planets are optimal for understanding the radius evolution and mass-loss processes that sculpt the close-in sub-Neptune population (e.g. Owen & Campos Estrada 2020). Having planets that formed from the same protoplanetary disc and experienced the same host star XUV evolution, allows us to test photoevaporation processes by isolating the effects of insulation on mass-loss. We tested for the future prospect of atmospheric transmission spectroscopic observations for the planets in the HIP 113103 system via a set of current and upcoming space-based facilities, including the *Twinkle Space Telescope* (Twinkle; Stotesbury et al. 2022), *HST* (Kimble et al. 2008; Tsiaras et al. 2016), and *JWST* (Bean et al. 2018; Jakobsen et al. 2022). *Twinkle* is a visible to infrared ( $0.5\ \mu\text{m}$ – $4.5\ \mu\text{m}$ ) 0.45-m space telescope set to begin scientific operations in 2025 at a 700 km geocentric Sun-synchronous orbit.

The simulated transmission *Twinkle* spectra is generated for both channels ( $0.5\ \mu\text{m} \leq \text{Ch0} \leq 2.43\ \mu\text{m}$ ,  $2.43\ \mu\text{m} \leq \text{Ch1} \leq$

$4.5\ \mu\text{m}$ ) using the radiometric tool available on the mission’s data base Stardrive<sup>3</sup>, while the *HST* (WFC3 NIR G141 grism:  $1.075\ \mu\text{m}$ – $1.7\ \mu\text{m}$ ) and *JWST* (NIRSpec G395H grism:  $2.87\ \mu\text{m}$ – $5.14\ \mu\text{m}$ ) transmission spectra are generated using the publicly available noise simulator, PANDEXO (Batalha et al. 2017). The synthetic transmission spectra are processed through the retrieval framework TAUREX 3.0 (Al-Refaie et al. 2021), which generates an atmosphere divided into 100 evenly spaced layers across a log grid varying from  $10^{-4}$  to  $10^6$  Pa. The trace gases in our models were assumed to be in chemical equilibrium and the abundances were calculated using FASTCHEM (Stock et al. 2018). We keep the C/O ratio fixed at 0.54 (an oxygen rich atmosphere at solar abundances as discussed in Madhusudhan 2012) and assume a metallicity of  $100 \times$  Solar for HIP 113103 b and  $10 \times$  Solar for HIP 113103 c, aligning with previous studies that relate metallicity and low-mass planets as being inversely proportional (e.g. Fortney et al. 2013; Kreidberg et al. 2014; Charnay, Meadows & Leconte 2015). The trace gases inserted into this atmosphere included the molecular opacities of  $\text{CH}_4$  (Hill, Yurchenko & Tennyson 2013; Yurchenko & Tennyson 2014),  $\text{CO}$  (Li et al. 2015),  $\text{CO}_2$  (Rothman et al. 2010),  $\text{H}_2\text{O}$  (Polyansky et al. 2018), and  $\text{NH}_3$  (Yurchenko, Barber & Tennyson 2011), with all opacities being obtained through the ExoMol (Tennyson et al. 2016) and HITRAN data bases (Gordon et al. 2016). In addition, we also implement Rayleigh scattering for all inserted molecules (Cox 2015), provide a collision induced absorption from  $\text{H}_2$ – $\text{H}_2$  (Abel et al. 2011; Fletcher, Gustafsson & Orton 2018) and  $\text{H}_2$ –He interactions (Abel et al. 2012). For each instrument, we modelled both a clear atmosphere scenario (i.e.  $P = 10^6$  Pa) and a uniform opaque deck scenario (i.e. grey clouds) at  $P = 10^1$  Pa.

We present our simulated spectra of HIP 113103 b in Fig. 11 and HIP 113103 c in Fig. 12. Should HIP 113103 b and HIP 113103 c reflect a similar composition as our simulated spectra, we can recover

<sup>3</sup>Stardrive Database

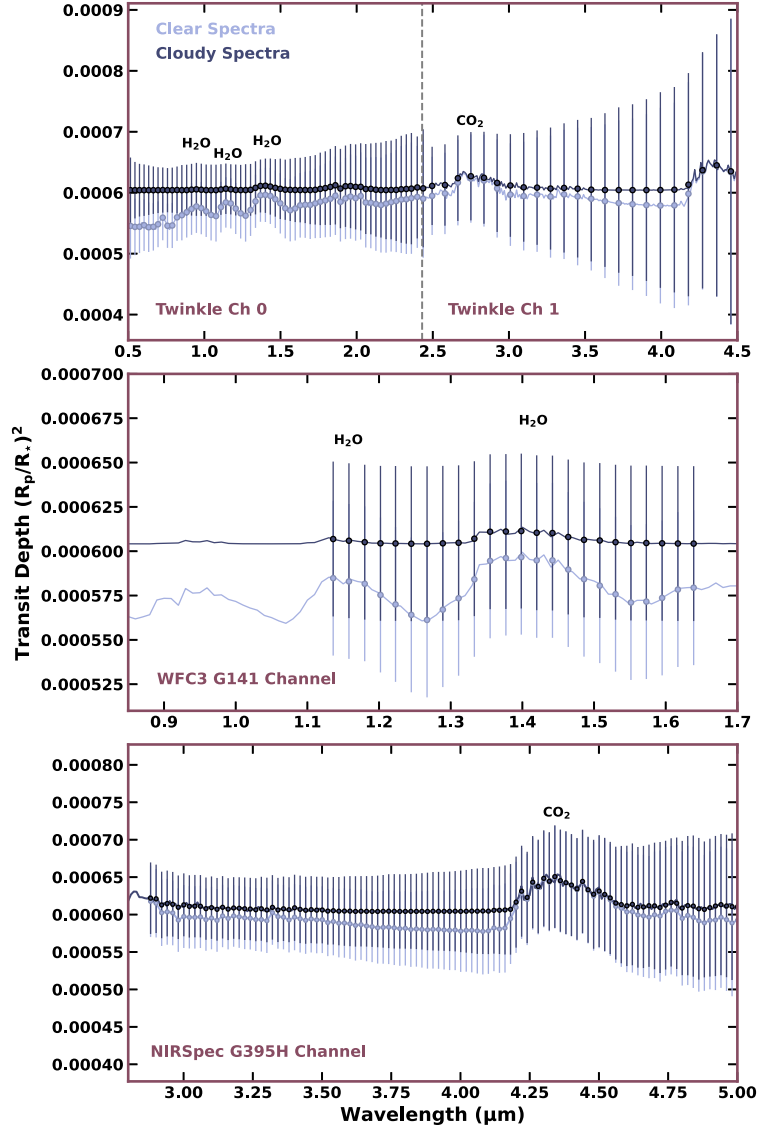


**Figure 11.** A synthetic atmospheric transmission spectra of HIP 113103 b, incorporating absorbing species  $\text{CH}_4$ ,  $\text{CO}$ ,  $\text{CO}_2$ ,  $\text{H}_2\text{O}$ , and  $\text{NH}_3$  at chemical equilibrium assuming an atmospheric metallicity of  $100\times$  Solar. The top panel illustrates the expected spectrum after 10 visits with *Twinkle*, the middle panel shows the simulated spectrum from a single visit with *HST* WFC3 with the G141 grism, and the bottom panel shows the simulated spectrum from a single visit with *JWST* NIRSpec G395H grism (with each instrument capturing a different wavelength range). For each facility, we have illustrated two scenarios: one where spectrum is cloud-free ( $10^6$  Pa), and another with a grey cloud deck ( $10^1$  Pa). The synthetic spectra for *Twinkle* was obtained using the radiometric tool on the *Twinkle* Stardrive portal, while the *HST* and *JWST* spectra were generated using PANDEXO.

a transmission spectra from 10 orbits using *Twinkle* (top panels; Stotesbury et al. 2022). Likewise, Figs 11 and 12 demonstrate the precision we can expect to achieve from one orbit observation using the infrared WFC3 G141 grism (middle panels) on *HST* (Kimble et al. 2008; Tsiaras et al. 2016) and NIRSpec G395H grism (bottom panels) on *JWST* (Bean et al. 2018; Jakobsen et al. 2022). We can successfully retrieve molecular species for HIP 113103 c with each

instrument given a clear atmosphere (with  $\text{H}_2\text{O}$  and  $\text{CO}_2$  displaying the strongest absorption). However, in the event of clouds, we would struggle to detect any signal for HIP 113103 c using *Twinkle* and *HST* instruments. Distinguishing between a clear or cloudy atmosphere on all three instruments is challenging for HIP 113103 b. An atmosphere that is in chemical disequilibrium for both targets could result in stronger absorption but would be dependent on various unknown

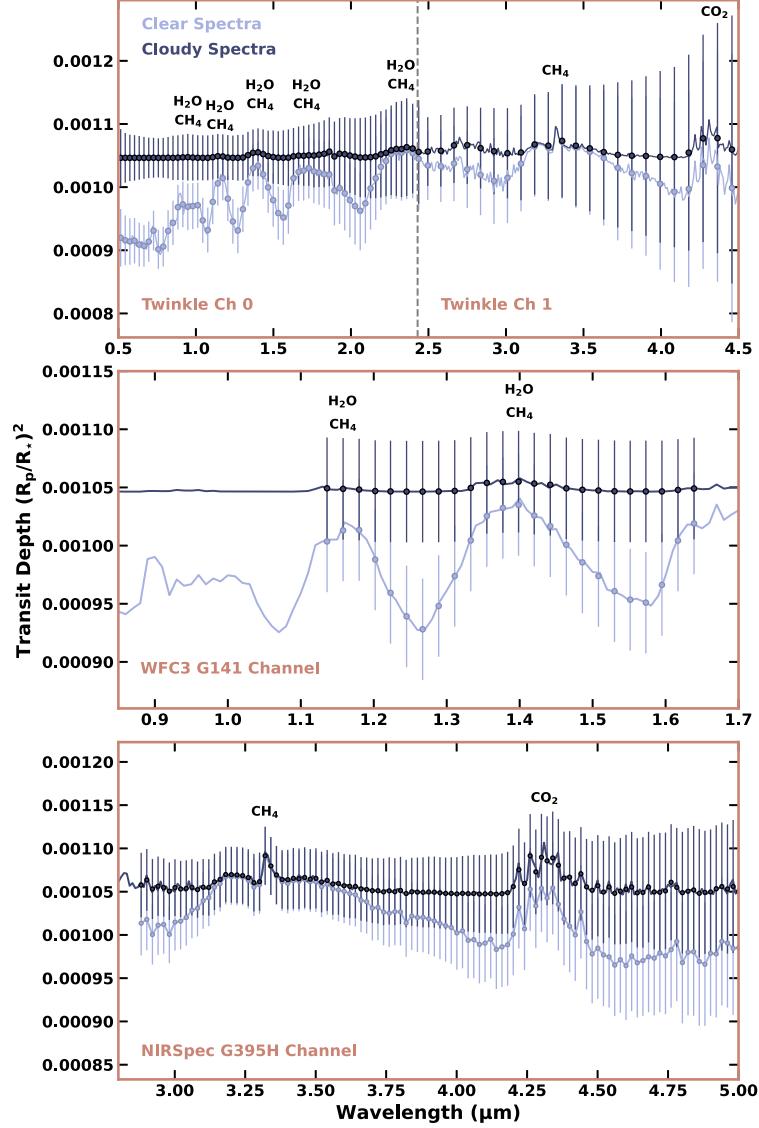


**Figure 12.** A synthetic atmospheric transmission spectrum of HIP 113103 c, with absorbing species including  $\text{CH}_4$ ,  $\text{CO}$ ,  $\text{CO}_2$ ,  $\text{H}_2\text{O}$ , and  $\text{NH}_3$  in chemical equilibrium at an atmospheric metallicity of  $10\times$ Solar. Figure configuration is as per Fig. 11, with the *Twinkle* retrieval representing 10 visits.

physical parameters. Alternatively, the evolutionary path of HIP 113103 b could be the product of a migrated Water World instead of photoevaporation of a mini-Neptune (e.g. Luque & Pallé 2022); however, this scenario can only be explored in more detail after planet density measurements have been calculated. Our density estimation for HIP 113103 b of  $0.96^{+0.15}_{-0.22} \rho_{\oplus}$  is indicative of a rocky planet, but is inferred from a mass–radius relationship and may not reflect the true bulk density of the planet. Accurate mass measurements of HIP 113103 b and HIP 113103 c are required to confirm their densities.

## 7 CONCLUSION

In this paper, we confirm the existence of two sub-Neptunes, HIP 113103 b and HIP 113103 c, within  $\sim 10\%$  of 2:1 resonance around the bright K3V star HIP 113103. First identified with *TESS*, this system is revisited using both ground based transit observations (observed with the photometric LCO network and on the CHIRON spectrograph), as well as a space-based photometric observations of both targets within a  $\sim 17.5$ -h visit using *CHEOPS*. Follow up TTV analysis does not reveal any additional outer companions. Our planetary parameters revealed a radius of  $R_p = 1.829^{+0.096}_{-0.067} R_{\oplus}$

for HIP 113103 b and  $R_p = 2.40^{+0.10}_{-0.08} R_\oplus$  for HIP 113103 c, confirming both targets reside within the mini-Neptune sub-class. For HIP 113103 b, the combination of its close proximity to HIP 113103 and its planetary radius means it resides within the radius gap, which if confirmed via mass follow up, would add an additional target a sparse sub-class of planets which are hypothesized to bridge the formation transition between super-Earths and mini-Neptunes. If HIP 113103 b is the subject of atmosphere evaporation due to its close proximity to HIP 113103, our generated retrieval plots (using the *Twinkle*, *HST*, and *JWST* telescopes) suggest it would be a struggle to distinguish an evolutionary gap via metallicity disparity for all three telescopes (assuming chemical equilibrium), even if there is a clear atmosphere. Ultimately, this system provides two key targets capable of atmospheric analysis within the population of mini-Neptune multiplanet systems orbiting K-stars.

#### ACKNOWLEDGEMENTS

We would like to acknowledge and pay respect to Australia's Aboriginal and Torres Strait Islander peoples, who are the traditional custodians of the lands, the waterways, and the skies all across Australia. We thank Australia's Aboriginal and Torres Strait Islander peoples for sharing and caring for the land on which we are able to learn. In particular, we pay our deepest respects to all Elders, ancestors, and descendants of the Giabal, Jarowair, and Yuggera nations, upon which the MINERVA-Australis facility is situated, and analysis for this paper was undertaken. We would also like to acknowledge and pay our deepest respects to the Indigenous Elders, ancestors and descendants who are the traditional custodians of the land upon which the CTIO, SAAO, and ESO 3.6-m are situated. This includes (but may not be exclusive to) the Diaguita and Khoisan nations. GZ thanks the support of the Australian Research Council (ARC) Discovery Early Career Research Award (DECRA) programme DE210101893. CXH thanks the support of the ARC DECRA programme DE200101840. GZ and SQ thank the support of the *TESS* Guest Investigator Program G03007. CH thanks the support of the ARC DECRA programme DE200101840. KAC acknowledges support from the *TESS* mission via subaward s3449 from MIT. This research has used data from the CTIO/SMARTS 1.5-m telescope, which is operated as part of the SMARTS Consortium by RECONS. This work makes use of data from the European Space Agency (ESA) mission *CHEOPS* via the *CHEOPS* Guest Observers Program AO-3-10. This work has made use of data from the ESA mission *Gaia*, processed by the *Gaia* Data Processing and Analysis Consortium (DPAC). Funding for the DPAC has been provided by national institutions, in particular the institutions participating in the *Gaia* Multilateral Agreement. This work makes use of observations from the LCOGT network. Part of the LCOGT telescope time was granted by NOIRLab through the Mid-Scale Innovations Programme (MSIP). MSIP is funded by NSF. This work makes use of data from the MINERVA-Australis facility. MINERVA-Australis is supported by Australian Research Council LIEF Grant LE160100001, Discovery Grants DP180100972 and DP220100365, Mount Cuba Astronomical Foundation, and institutional partners University of Southern Queensland, University of New South Wales Sydney, Massachusetts Institute of Technology, Nanjing University, George Mason University, University of Louisville, University of California Riverside, University of Florida, and The University of Texas at Austin. This research has made use of the NASA Exoplanet Archive, which is operated by the California Institute of Technology, under contract with the National Aeronautics and Space Administration

under the Exoplanet Exploration Programme. This work has been carried out within the framework of the NCCR PlanetS supported by the Swiss National Science Foundation under grants 51NF40<sub>182901</sub> and 51NF40<sub>205606</sub>. Funding for the *TESS* mission is provided by NASA's Science Mission directorate. We acknowledge the use of public *TESS* Alert data from pipelines at the *TESS* Science Office and at the *TESS* Science Processing Operations Center. This research has made use of the Exoplanet Follow-up Observation Programme (ExoFOP; DOI: 10.26134/ExoFOP5) website, which is operated by the California Institute of Technology, under contract with the National Aeronautics and Space Administration under the Exoplanet Exploration Programme. This paper includes data collected by the *TESS* mission, which are publicly available from the Mikulski Archive for Space Telescopes (MAST). Resources supporting this work were provided by the NASA High-End Computing (HEC) Programme through the NASA Advanced Supercomputing (NAS) Division at Ames Research Center for the production of the SPOC data products.

#### DATA AVAILABILITY

The data underlying this article will be shared on reasonable request to the corresponding author.

#### REFERENCES

- Abel M., Frommhold L., Li X., Hunt K. L., 2011, *J. Phys. Chem. A*, 115, 6805  
 Abel M., Frommhold L., Li X., Hunt K. L., 2012, *J. Chem. Phys.*, 136, 44319  
 Addison B. et al., 2019, *PASP*, 131, 115003  
 Agol E., Deck K., 2016, *ApJ*, 818, 177  
 Agüeros M. A. et al., 2018, *ApJ*, 862, 33  
 Ahrer E.-M. et al., 2023, *Nature*, 614, 653  
 Al-Refaie A. F., Changeat Q., Waldmann I. P., Tinetti G., 2021, *ApJ*, 917, 37  
 Alderson L. et al., 2023, *Nature*, 614, 664  
 Allart R. et al., 2019, *A&A*, 623, A58  
 Angus R., Aigrain S., Foreman-Mackey D., McQuillan A., 2015, *MNRAS*, 450, 1787  
 Baliunas S. L. et al., 1995, *ApJ*, 438, 269  
 Barnes S. L., Gibson S., Nield K., Cochran D., 2012, in McLean I. S., Ramsay S. K., Takami H. eds, *SPIE Conf. Ser. Vol. 8446, Ground-based and Airborne Instrumentation for Astronomy IV*. SPIE, Bellingham. p. 844688  
 Barragán O. et al., 2022, *MNRAS*, 514, 1606  
 Batalha N. E. et al., 2017, *PASP*, 129, 64501  
 Bean J. L. et al., 2018, *PASP*, 130, 114402  
 Bean J. L., Raymond S. N., Owen J. E., 2021, *J. Geophys. Res. (Planets)*, 126, e06639  
 Benneke B. et al., 2019, *Nature Astron.*, 3, 813  
 Benz W. et al., 2021, *Exp. Astron.*, 51, 109  
 Bergsten G. J., Pascucci I., Mulders G. D., Fernandes R. B., Koskinen T. T., 2022, *AJ*, 164, 5  
 Bouma L. G., Palumbo E. K., Hillenbrand L. A., 2023, *ApJ*, 947, L3  
 Brahm R., Jordán A., Hartman J., Bakos G., 2017, *MNRAS*, 467, 971  
 Brandt T. D., 2021, *ApJS*, 254, 42  
 Brown T. M. et al., 2013, *PASP*, 125, 1031  
 Buchhave L. A. et al., 2012, *Nature*, 486, 375  
 Castelli F., Kurucz R. L., 2004, preprint (arXiv:Astrophysics e-prints)  
 Charnay B., Meadows V., Lecointe J., 2015, *ApJ*, 813, 15  
 Claret A., 2017, *A&A*, 600, A30  
 Claret A., Bloemen S., 2011, *A&A*, 529, A75  
 Cloutier R. et al., 2020, *AJ*, 160, 3  
 Collins K. A., Kielkopf J. F., Stassun K. G., Hessman F. V., 2017, *AJ*, 153, 77

- Cox A. N., 2015, in *Allen's Astrophysical Quantities*. Springer, United Kingdom, p. 721
- Cutri R. M. et al., 2012, *VizieR Online Data Catalog*, p. II/311
- Czesla S., Schröter S., Schneider C. P., Huber K. F., Pfeifer F., Andreasen D. T., Zechmeister M., 2019, *PyA: Python astronomy-related packages*, preprint (ascl:1906.010)
- Delrez L. et al., 2021, *Nature Astron.*, 5, 775
- Donati J.-F., Semel M., Carter B. D., Rees D. E., Collier Cameron A., 1997, *MNRAS*, 291, 658
- Dotter A., 2016, *ApJS*, 222, 8
- Douglas S. T., Curtis J. L., Agüeros M. A., Cargile P. A., Brewer J. M., Meibom S., Jansen T., 2019, *ApJ*, 879, 100
- Dragomir D. et al., 2019, *ApJ*, 875, L7
- Duncan D. K. et al., 1991, *ApJS*, 76, 383
- Edwards B. et al., 2022, preprint (arXiv:2211.00649)
- Feinstein A. D. et al., 2023, *Nature*, 614, 670
- Fletcher L. N., Gustafsson M., Orton G. S., 2018, *ApJS*, 235, 24
- Foreman-Mackey D., Hogg D. W., Lang D., Goodman J., 2013, *PASP*, 125, 306
- Fortney J. J., Mordasini C., Nettelmann N., Kempton E. M. R., Greene T. P., Zahnle K., 2013, *ApJ*, 775, 80
- Fressin F. et al., 2013, *ApJ*, 766, 81
- Fu G. et al., 2022, *ApJ*, 940, L35
- Fulton B. J. et al., 2017, *AJ*, 154, 109
- Fulton B. J., Petigura E. A., Blunt S., Sinukoff E., 2018, *PASP*, 130, 44504
- Gaia Collaboration, 2018, *A&A*, 616, A1
- Gaia Collaboration, 2022, *A&A*, 674, A1
- Gan T. et al., 2022, *MNRAS*, 514, 4120
- Gandolfi D. et al., 2018, *A&A*, 619, L10
- Gandolfi D. et al., 2019, *ApJ*, 876, L24
- Giacalone S. et al., 2021, *AJ*, 161, 24
- Ginzburg S., Schlichting H. E., Sari R., 2018, *MNRAS*, 476, 759
- Gordon I., Rothman L. S., Wilzewski J. S., Kochanov R. V., Hill C., Tan Y., Wcislo P., 2016, in *AAS/Division for Planetary Sciences Meeting Abstracts #48*, p. 421.13
- Gray R. O., Corbally C. J., 1994, *AJ*, 107, 742
- Greene T. P., Line M. R., Montero C., Fortney J. J., Lustig-Yaeger J., Luther K., 2016, *ApJ*, 817, 17
- Guerrero N. M. et al., 2021, *ApJS*, 254, 39
- Guilluy G. et al., 2020, *A&A*, 639, A49
- Henry T. J., Soderblom D. R., Donahue R. A., Baliunas S. L., 1996, *AJ*, 111, 439
- Hill C., Yurchenko S. N., Tennyson J., 2013, *Icarus*, 226, 1673
- Høg E. et al., 2000, *A&A*, 355, L27
- Howard A. W. et al., 2012, *ApJS*, 201, 15
- Howe A. R., Burrows A., 2015, *ApJ*, 808, 150
- Huang C. X. et al., 2020a, *Res. Notes Am. Astron. Soc.*, 4, 204
- Huang C. X. et al., 2020b, *Res. Notes Am. Astron. Soc.*, 4, 206
- Huang X., Bakos G. Á., Hartman J. D., 2013, *MNRAS*, 429, 2001
- Jakobsen P. et al., 2022, *A&A*, 661, A80
- Jenkins J. M. et al., 2016, in *Software and Cyberinfrastructure for Astronomy IV*, p. 99133E
- Jurić M., Tremaine S., 2008, *ApJ*, 686, 603
- Kawauchi K. et al., 2022, *A&A*, 666, A4
- Kempton E. M. R. et al., 2018, *PASP*, 130, 114401
- Ketzer L., Poppenhaeger K., 2022, *MNRAS*, 518, 1683
- Kimble R. A., MacKenty J. W., O'Connell R. W., Townsend J. A., 2008, in *Oschmann Jacobus M. J., de Graauw M. W. M., MacEwen H. A. eds, SPIE Conf. Ser. Vol. 7010, Space Telescopes and Instrumentation 2008: Optical, Infrared, and Millimeter*. SPIE, Bellingham. p. 70101E
- Kipping D. M., 2010, *MNRAS*, 408, 1758
- Kite E. S., Barnett M. N., 2020, *Proc. Natl. Acad. Sci.*, 117, 18264
- Kite E. S., Fegley Bruce J., Schaefer L., Ford E. B., 2020, *ApJ*, 891, 111
- Kovács G., Zucker S., Mazeh T., 2002, *A&A*, 391, 369
- Kreidberg L. et al., 2014, *Nature*, 505, 69
- Kreidberg L., 2015, *PASP*, 127, 1161
- Li G., Gordon I. E., Rothman L. S., Tan Y., Hu S.-M., Kassi S., Campargue A., Medvedev E. S., 2015, *ApJS*, 216, 15
- Lindgren L. et al., 2021, *A&A*, 649, A4
- Lopez E. D., Fortney J. J., Miller N., 2012, *ApJ*, 761, 59
- Lubin J. et al., 2022, *AJ*, 163, 101
- Luque R., Pallé E., 2022, *Science*, 377, 1211
- MacDougall M. G. et al., 2021, *AJ*, 162, 265
- Madhusudhan N., 2012, *ApJ*, 758, 36
- Mamajek E. E., Hillenbrand L. A., 2008, *ApJ*, 687, 1264
- Mandel K., Agol E., 2002, *ApJ*, 580, L171
- Masuda K., Winn J. N., 2020, *AJ*, 159, 81
- Maxted P. F. L. et al., 2022, *MNRAS*, 514, 77
- Mayor M. et al., 2003, *Messenger*, 114, 20
- Mazeh T., Faigler S., 2010, *A&A*, 521, L59
- McCully C., Volgenau N. H., Harbeck D.-R., Lister T. A., Saunders E. S., Turner M. L., Siivert R. J., Bowman M., 2018, in *Proc. SPIE. 10707*, p.107070K
- Meibom S., Mathieu R. D., Stassun K. G., 2009, *ApJ*, 695, 679
- Mordasini C., 2020, *A&A*, 638, A52
- Morris R. L., Twicken J. D., Smith J. C., Clarke B. D., Jenkins J. M., Bryson S. T., Girouard F., Klaus T. C., 2020, *Kepler Data Processing Handbook: KSC1-19081-003*
- Mugnai L. V. et al., 2021, *AJ*, 161, 284
- Neil A. R., Rogers L. A., 2018, *ApJ*, 858, 58
- Nortmann L. et al., 2018, *Science*, 362, 1388
- Noyes R. W., Hartmann L. W., Baliunas S. L., Duncan D. K., Vaughan A. H., 1984, *ApJ*, 279, 763
- Orell-Miquel J. et al., 2022, *A&A*, 659, A55
- Osborn A. et al., 2021, *MNRAS*, 507, 2782
- Owen J. E., Campos Estrada B., 2020, *MNRAS*, 491, 5287
- Owen J. E., Jackson A. P., 2012, *MNRAS*, 425, 2931
- Paredes L. A., Henry T. J., Quinn S. N., Gies D. R., Hinojosa-Goñi R., James H.-S., Jao W.-C., White R. J., 2021, *AJ*, 162, 176
- Pepe F. et al., 2021, *A&A*, 645, A96
- Perryman M. A. C. et al., 1997, *A&A*, 323, L49
- Pollacco D. L. et al., 2006, *PASP*, 118, 1407
- Polyansky O. L., Kyuberis A. A., Zobov N. F., Tennyson J., Yurchenko S. N., Lodi L., 2018, *MNRAS*, 480, 2597
- Ricker G. R. et al., 2015, *J. Astron. Telescopes Instrum. Syst.*, 1, 14003
- Rodríguez J. E. et al., 2017, *AJ*, 153, 256
- Rodríguez J. E., Vanderburg A., Eastman J. D., Mann A. W., Crossfield I. J. M., Ciardi D. R., Latham D. W., Quinn S. N., 2018, *AJ*, 155, 72
- Rojas-Ayala B., 2023, preprint (arXiv:2301.03442)
- Rothman L. et al., 2010, *J. Quant. Spectrosc. Radiat. Transfer*, 111, 2139
- Rustamkulov Z. et al., 2023, *Nature*, 614, 659
- Scarsdale N. et al., 2021, *AJ*, 162, 215
- Seager S., Mallén-Omelas G., 2003, *ApJ*, 585, 1038
- Skrutskie M. F. et al., 2006, *AJ*, 131, 1163
- Sozzetti A. et al., 2021, *A&A*, 648, A75
- Stassun K. G. et al., 2019, *AJ*, 158, 138
- Stock J. W., Kitzmann D., Patzer A. B. C., Sedlmayr E., 2018, *MNRAS*, 479, 865
- Stotesbury I. et al., 2022, in *Coyle L. E., Matsuura S., Perrin M. D. eds, SPIE Conf. Ser. Vol. 12180, Space Telescopes and Instrumentation 2022: Optical, Infrared, and Millimeter Wave*. SPIE, Bellingham. p. 1218033
- Tennyson J. et al., 2016, *J. Mol. Spectrosc.*, 327, 73
- Teske J. et al., 2020, *AJ*, 160, 96
- Tinetti G. et al., 2018, *Exp. Astron.*, 46, 135
- Tofflemire B. M. et al., 2021, *AJ*, 161, 171
- Tokovinin A., Fischer D. A., Bonati M., Giguere M. J., Moore P., Schwab C., Spronck J. F. P., Szymkowiak A., 2013, *PASP*, 125, 1336
- Tsai S.-M. et al., 2023, *Nature*, 617, 483
- Tsiaras A. et al., 2016, *ApJ*, 820, 99
- Tsiaras A., Waldmann I. P., Tinetti G., Tennyson J., Yurchenko S. N., 2019, *Nature Astron.*, 3, 1086
- Twicken J. D., Clarke B. D., Bryson S. T., Tenenbaum P., Wu H., Jenkins J. M., Girouard F., Klaus T. C., 2010, in *Software and Cyberinfrastructure for Astronomy*, p. 774023
- Vanderburg A. et al., 2019, *ApJ*, 881, L19
- Vanderburg A., Johnson J. A., 2014, *PASP*, 126, 948

Vaughan A. H., Preston G. W., Wilson O. C., 1978, *PASP*, 90, 267

Walker J. C. G., 1986, *Icarus*, 68, 87

Wilson O. C., 1978, *ApJ*, 226, 379

Winn J. N. et al., 2011, *ApJ*, 737, L18

Wolfgang A., Rogers L. A., Ford E. B., 2016, *ApJ*, 825, 19

Yurchenko S. N., Barber R. J., Tennyson J., 2011, *MNRAS*, 413, 1828

Yurchenko S. N., Tennyson J., 2014, *MNRAS*, 440, 1649

Zhou G. et al., 2021, *AJ*, 161, 2

Zhou G. et al., 2022, *AJ*, 163, 289

<sup>1</sup>Centre for Astrophysics, University of Southern Queensland, 499-565 West Street, Toowoomba, QLD 4350, Australia

<sup>2</sup>SRON, Netherlands Institute for Space Research, Niels Bohrweg 4, NL-2333 CA, Leiden, The Netherlands

<sup>3</sup>Center for Astrophysics | Harvard & Smithsonian, 60 Garden Street, Cambridge, MA 02138, USA

<sup>4</sup>Winton Fellow

<sup>5</sup>Astronomy Unit, Queen Mary University of London, Mile End Road, London E1 4NS, UK

<sup>6</sup>Astrophysics Group, Cavendish Laboratory, J.J. Thomson Avenue, Cambridge CB3 0HE, UK

<sup>7</sup>Observatoire de Genève, Université de Genève, 51 Chemin Pegasi, CH-1290 Versoix, Switzerland

<sup>8</sup>School of Physics & Astronomy, University of Birmingham, Edgbaston, Birmingham B15 2TT, UK

<sup>9</sup>Astrophysics Group, Keele University, Keele ST5 5BG, UK

<sup>10</sup>Department of Physics and Kavli Institute for Astrophysics and Space Research, Massachusetts Institute of Technology, Cambridge, MA 02139, USA

<sup>11</sup>Department of Earth, Atmospheric and Planetary Sciences, Massachusetts Institute of Technology, 77 Massachusetts Ave, Cambridge, MA 02139, USA

<sup>12</sup>Department of Aeronautics and Astronautics, Massachusetts Institute of Technology, 77 Massachusetts Avenue, Cambridge, MA 02139, USA

<sup>13</sup>Department of Astrophysical Sciences, Princeton University, 4 Ivy Lane, Princeton, NJ 08544, USA

<sup>14</sup>NASA Ames Research Center, Moffett Field, CA 94035, USA

<sup>15</sup>SETI Institute, Mountain View, CA 94043, USA

<sup>16</sup>Instituto de Astrofísica de Canarias, C/vía Láctea, s/n, E-38205 La Laguna, Tenerife, Spain

<sup>17</sup>Departamento de Astrofísica, Universidad de La Laguna (ULL), E-38206 La Laguna, Tenerife, Spain

<sup>18</sup>Department of Physics, University of Warwick, Gibbet Hill Road, Coventry CV4 7AL, UK

<sup>19</sup>Centre for Exoplanets and Habitability, University of Warwick, Gibbet Hill Road, Coventry CV4 7AL, UK

<sup>20</sup>Department of Astronomy, The University of Texas at Austin, TX 78712, USA

<sup>21</sup>Department of Earth and Planetary Sciences, University of California, Riverside, CA 92521, USA

<sup>22</sup>Department of Physics and Astronomy, University of Louisville, Louisville, KY 40292, USA

<sup>23</sup>Department of Physics & Astronomy, George Mason University, 4400 University Drive MS 3F3, Fairfax, VA 22030, USA

<sup>24</sup>Shanghai Astronomical Observatory, Chinese Academy of Sciences, Shanghai 200030, China

This paper has been typeset from a  $\text{\TeX}/\text{\LaTeX}$  file prepared by the author.

## 4.2 LINKS AND IMPLICATIONS

Please refer to Section 6.1.2 in Chapter 6 to understand how this paper has contributed towards the exoplanet community.

# CHAPTER 5: PAPER 3: TARGET PREPARATION FOR THE *TWINKLE SPACE* *MISSION*.

## 5.1 INTRODUCTION

IN THE ADVENT OF next generation satellite telescopes having a large portion (if not all) of their science cases focused on exoplanet characterisation (e.g. *JWST* and *Ariel*), it is important we diligently prepare future space surveys ahead of launch, as to maximise the science output once first light is achieved. The *Twinkle Space Mission* (of which UniSQ is a founding member) is a visible to infrared ( $0.5\ \mu\text{m} - 4.5\ \mu\text{m}$ ) 0.45 m space telescope set to begin scientific operations in 2025 at a 700 km geocentric Sun-synchronous orbit.

THIS WORK IS FOCUSED on preparing 28 targets for the *Twinkle Space Mission*, using photometry from *TESS*. Our ephemerides values improve and extend previous transit timing constraints, with uncertainties being tightly constrained to cover the entirety of the initial three year survey. Within our 28 target sample, we also identify nine single-planet systems that present short-term transit timing variations. The source of these variations, in addition to

targets from our sample that are not observed throughout the *TESS* mission, will be further explored using global network of ground-based facilities (including MINERVA South at UniSQ).

## Target Preparation for the *Twinkle Space Mission*

NATALIEA LOWSON <sup>1</sup>, DUNCAN J. WRIGHT <sup>1</sup>, CHELSEA X. HUANG <sup>1</sup>, GEORGE ZHOU <sup>1</sup>

<sup>1</sup>Centre for Astrophysics, University of Southern Queensland, 499-565 West Street, Toowoomba, QLD 4350, Australia

### ABSTRACT

*Twinkle*, an upcoming seven-year satellite mission, is poised to conduct an initial three-year survey that will contribute towards advancing exosolar and Solar System research. It is therefore vital that the orbital constraints on targets are well established to maximise survey time prior to first light. Leveraging photometry from the *TESS* mission, we conduct transit timing refinement for 28 exoplanets from a sample of 50 targets that have been selected for the exosolar component of the *Twinkle Space Mission*. Our values improve upon previous transit timing constraints, with uncertainties tightly constrained to cover the entirety of the initial three year survey. We also identify single-planet systems of interest from our sample that are indicative of short-term variations. Ground-based monitoring will be conducted for targets that require tighter transit timing constraints, targets in our sample that will not be observed through the *TESS* mission, and to further investigate the identified transit timing variations.

*Keywords:* Exoplanets(498) — Light curve classification (1954) — Transient detection(1957) — Ephemerides(464) — Transit timing variation method(1710)

### 1. INTRODUCTION

Exoplanet research has now reached turning point from a strong focus on discovery towards characterisation, particularly for their atmospheres. This shift coincides with the launch of next generation satellites such as the *James Webb Space Telescope (JWST)* (Gardner et al. 2006) and the *Atmospheric Remote-sensing Infrared Exoplanet Large-survey (ARIEL)* (Tinetti et al. 2018) capable of observing exoplanets in the optical and infrared, two key regions required to analyse the dynamics and temporal variation affiliated with deep layers in exoplanet atmospheres. Another upcoming exoplanet mission, the *Twinkle Space Mission (Twinkle)*, is set to begin scientific operations in 2025 on a 700 km geocentric Sun-synchronous orbit. Its 0.45 m aperture will be capable of obtaining photometric and spectroscopic observations ranging from the visible to infrared (0.5 $\mu$ m – 4.5 $\mu$ m) (Edwards et al. 2019; Stotesbury et al. 2022). The primary mission will observe thousands of targets over an initial seven year period, with time allocated towards extrasolar and Solar System objects. Led

by the Blue Skies Space Science, the mission is being overseen by a global network of institutions.

Although orbital constraints are evaluated for exoplanets when discovered, their accuracy decays over time which can result in incorrect transit opportunity predictions. The source of this decay can be due to a number of physical effects, including mass loss or an interaction with unseen companions within the system. For the latter, this effect is known as transit timing variation (TTV), and is identified when the ingress and egress of an exoplanet occurs before or after the predicted values. Given the time sensitive nature of satellite surveys like *Twinkle*, it is critical to monitor these targets and provide updated parameter constraints, in particular the transit time of conjunction, otherwise formally known as the ephemerides. Large community efforts to provide updated ephemerides values for various targets have been successful through programs such as ExoClock, as well as individual projects such as Transit Timing en Mass (Ivshina & Winn 2022; Kokori et al. 2023).

In this paper, we report updated ephemerides of targets selected for the science cases that *Twinkle* members will investigate as part of the extra-solar survey component of the *Twinkle Space Mission*. We also monitor for TTV signals in each system. The initial observation selection process is outlined in Section 2 while the mod-

Corresponding author: Nataliea Lowson  
nataliea.lowson@usq.edu.au

els for calculating the ephemerides and TTV identification is outlined in Section 3. Our Results and Discussion are presented in Section 4 followed by our Conclusion in Section 5.

## 2. DATA SELECTION

The targets in this paper have been selected in accordance to the science goals agreed upon for the extra-solar survey by the *Twinkle* founding members. This includes focus groups on (but is not limited to) Super-Earths sub-Neptunes, ultra hot-Jupiters, TTVs, and Ground-Based analysis. With the continuous all-sky monitoring from *TESS*, we identify which targets have been observed through two or more sectors and use these observations to refine ephemerides and monitor for TTVs (Section 2.1). For targets with less than two sectors of observations via *TESS*, we perform ground-based follow up using a global network of telescopes accessible to the founding members (Section 2.2).

### 2.1. *TESS*

The *TESS* photometry originates from the Science Processing Operations Center (SPOC, Jenkins et al. 2016) at NASA Ames Research Center, and is publicly available via the Mikulski Archive for Space Telescopes (MAST)<sup>1</sup>. We obtained the Presearch Data Conditioning Simple Aperture Photometry (PDCSAP) light curves, which already correct for instrumentation systematics from the *TESS* spacecraft. Stellar modulation was removed independently before the ephemerides refinement and TTV fitting via masking each transit using the cosine method from the detrending software *wotan* (Hippke et al. 2019). For each target we determine a window size, which is a single configurable parameter that describes the smoothing timescale. The window size is evaluated as three times the transit duration ( $T_{14}$ ), where  $T_{14}$  values are extracted from the Exoplanet Follow-up Observing Program (ExoFOP)<sup>2</sup> *TESS* objects of interest (TOI) list. If a target does not have a TOI affiliation, the  $T_{14}$  value is extracted from the NASA Exoplanet Archive<sup>3</sup>. The full target list obtained from *TESS* is presented in Table 1.

### 2.2. Ground-Based Follow-up Photometry

Additional observations are conducted by the *Twinkle* Ground-Based working group, which is monitoring selected targets prior to launch and will also manage any

<sup>1</sup> <https://archive.stsci.edu/portal/>

<sup>2</sup> <https://exofop.ipac.caltech.edu/tess/>

<sup>3</sup> <https://exoplanetarchive.ipac.caltech.edu/index.html>

requested ground-based follow up throughout the mission. For targets in Table 1, we perform ground-based observations using a global network of facilities that are available to the Ground-Based working group under two conditions. Either there is no *TESS* data observed prior to launch, or the *TESS* data that is available does not constrain the ephemerides of our target within the acceptable threshold determined for the *Twinkle Space Mission*.

## 3. MODEL

In order to evaluate the ephemerides and monitor for TTV activity, we perform a model fit via Bayesian statistical analysis on each target using the observations outlined in Section 2.

### 3.1. Estimating Ephemerides

The photometric model light curves are generated using *batman*, with the period,  $P$ , and time of conjunction,  $T_0$  fitted as free parameters. The planetary radius,  $R_p$ , is extracted for each target from the ExoFOP *TESS* candidate target list. Since ExoFOP does not always provide values for the ratio of semi-major axis to stellar radius,  $a/R_*$ , and line of sight inclination,  $i$ , when not available they are obtained from the latest publication on for a given target on the NASA Exoplanet Archive. The limb-darkening  $u1$  and  $u2$  parameters are evaluated for each target using ExoTiC-LD (Grant & Wakeford 2022) using a quadratic configuration. The selected stellar grid for our ExoTiC-LD parameters use the stellar models from (Kostogryz et al. 2022) evaluated with abundances from (Asplund et al. 2009) and stellar parameters from (Viani et al. 2018) for the chemical mixing length. An example of our model fitted against the data is presented in Figures 1 and 2. The targets known to have an eccentricity consistent with 0 are fixed such that the eccentricity,  $e$ , and argument of periapsis,  $\omega$ , are constant at 0. Those with non-zero eccentricities have their  $e$  and  $\omega$ , fixed at the best fit value available to avoid degeneracies in fitting those parameters confusing or masking any transit timing variations.

We constrained the ephemerides for each target using the Markov Chain Monte Carlo (MCMC) method via the python package *emcee* (Foreman-Mackey et al. 2013). We implemented 40 walkers over 2500 iterations per walker, with the first 700 iterations allocated to burn in. We use Gaussian priors taken from previously published data where available. If targets within our sample were part of the Transit Timing En Mass project (Ivshina & Winn 2022), they were also included in the ExoClock III data release (Kokori et al. 2023), which was simultaneously but independently published.

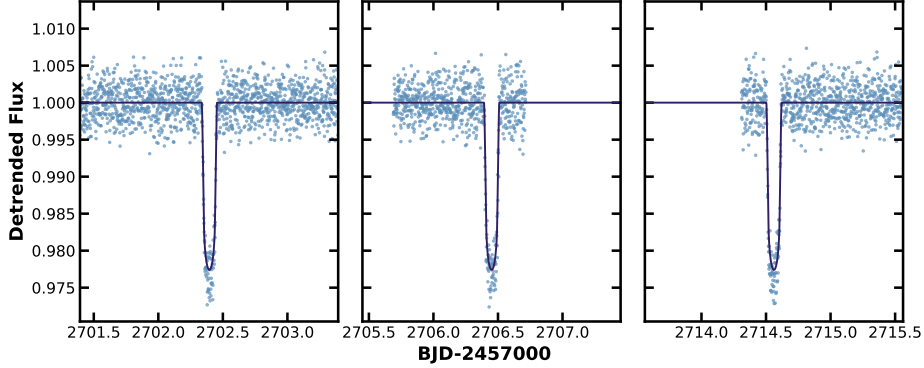


Figure 1. The detrended *TESS* data of WASP-39b against the best fit light curve model.

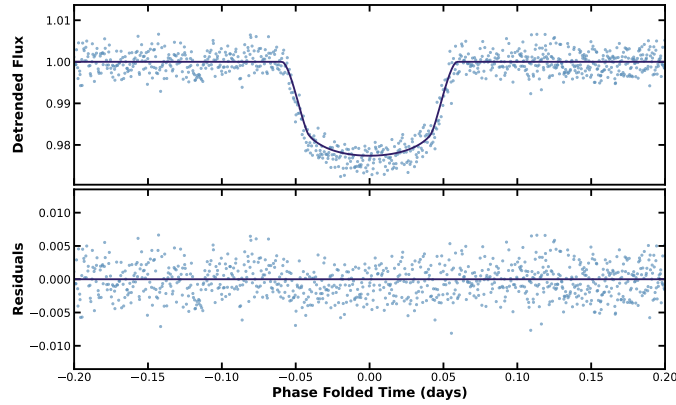


Figure 2. The **top** panel presents the detrended phase folded *TESS* transit data of WASP-39 b against the best fit light curve model. The **bottom** panel illustrates the residuals of the data.

Although our targets were constrained in both publications, we only reference Kokori et al. (2023), since it is the more recent publication. Kokori et al. (2023) constrained ephemerides values up to *TESS* Sector 44 (November 2021). As a consequence, if a target is referenced in Kokori et al. (2023), we fit for transits in *TESS* Sectors 45 to 67 (06 Nov 2021 to 29 Jul 2023), adopting the ExoClock III ephemerides values as priors in our model via the Gaussian prior method. If a target is absent from the Kokori et al. (2023) publication but had its ephemerides constrained using *TESS* photometry subsequent to Sector 45, we perform a fitting analysis for all available transits up to Sector 67, starting from its most recent publication date (see Table 2). This fitting process also employs a Gaussian prior, similar to our approach for targets featured in Kokori et al. (2023). If a target was not amongst the Kokori et al. (2023) sample, nor had any subsequent ephemerides refinement in other

publications, we used all the available *TESS* Sectors up to 67 to constrain the ephemerides using a uniform prior distribution. Targets modelled with a uniform prior had  $T_0$ ,  $P$ ,  $a/R_*$ , and  $i$ , as free parameters, using  $T_0$  and  $P$  values from ExoFOP for targets with a *TESS* Object of Interest (TOI) number or  $T_0$  and  $P$  values from the latest publication available on the Exoplanet Archive for those without a TOI number. The evaluated values for each target are presented in Table 3.

### 3.2. Searching for Transit Timing Variations

In addition to constraining the ephemerides, we search for TTV signals using all available *TESS* Sectors from MAST. To derive accurate transit times for each event, we perform an additional MCMC fit for each target (as outlined in Section 3.1), with three notable changes. First, we fix  $P$  to the evaluated value for each target presented in Table 3, only enabling  $T_0$  to remain as

**Table 1.** The *TESS* targets and their corresponding Sectors that were used for ephemerides refinement. Note that all available Sectors per target were used in the TTV analysis.

System	TIC	<i>TESS</i> Magnitude	Sectors
55 Cnc e	TIC332064670	$5.2058 \pm 0.006$	45, 46
GJ 3470 b	TIC19028197	$10.2479 \pm 0.007$	45, 46
GJ 436 b	TIC138819293	$8.40346 \pm 0.007$	49
GJ 9827 d	TIC301289516	$9.0684 \pm 0.006$	42
HAT-P-12 b	TIC198108326	$11.7551 \pm 0.006$	49, 50
HAT-P-26 b	TIC420779000	$10.9016 \pm 0.006$	50
HD 189733 b	TIC256364928	$6.8481 \pm 0.006$	54
HD 209458 b	TIC420814525	$7.1274 \pm 0.006$	56
HD 63433 b and HD 63433 c	TIC130181866	$6.2683 \pm 0.006$	45,46,47
HD 73583 b	TIC101011575	$8.5925 \pm 0.006$	61
HD 97658 b	TIC82308728	$6.9859 \pm 0.006$	49
K2-141 c	TIC301235044	$10.0298 \pm 0.006$	42
K2-18 c	TIC388804061	$11.2373 \pm 0.007$	45, 46
K2-3 b and K2-3 c and K2-3 d	TIC173103335	$10.5459 \pm 0.0073$	45, 46
KELT-20 b	TIC69679391	$7.5522 \pm 0.006$	54
TOI-1130 b and TOI-1130 c	TIC254113311	$10.1429 \pm 0.006$	67
TOI-178 d	TIC251848941	$10.42 \pm 0.006$	29
TOI-620 b	TIC296739893	$10.2139 \pm 0.007$	62
TOI-776 b and TOI-776 c	TIC306996324	$9.73597 \pm 0.007$	63
WASP-11 b	TIC85593751	$10.9332 \pm 0.006$	58
WASP-39 b	TIC181949561	$11.3763 \pm 0.006$	51
WASP-69 b	TIC248853232	$8.8628 \pm 0.006$	55
WASP-80 b	TIC243921117	$10.3622 \pm 0.007$	54

a free parameter, and second, we use a uniform prior for each target. Lastly, each individual transit has  $T_0$  independently evaluated rather than simultaneously as performed in Section 3.1. We also perform an outlier rejection above  $4\sigma$  for each transit. This method is only applicable for small TTVs, with variations larger than an hour requiring additional free parameters.

## 4. RESULTS AND DISCUSSION

### 4.1. Ephemerides Refinement

We use the publicly available *TESS* Sectors between 45 and 67 to refine the ephemerides of targets for the upcoming *Twinkle Space Mission*, with the updated parameters presented in Table 3. We forward project the transit time uncertainty for each Target to July 2029, when *Twinkle* is expected to complete its initial survey. With the exception of K2-141 c, K2-18 b, and K-3 b, each target has a projected transit time uncertainty that is improved from previously published values, meeting the 10 minute uncertainty threshold. The projected values for K2-141 c, K2-18 b, and K2-3 b have uncertainties larger than 10 minutes (the acceptable threshold determined for the *Twinkle Space Mission*), meaning additional transit data is required to constrain these values for the mission. These targets will be re-observed prior to launch via the *Twinkle* Ground-Based working group, using a global network of ground facilities available to the *Twinkle* science team. Additionally, we will also perform ground monitoring for GJ 1214 b, HD 3167 c, WASP-74 b, and WASP-103 b, which are in the priority list but will not be observed throughout the *TESS* mission’s currently scheduled Extended Missions.

### 4.2. TTV monitoring

For each target, we monitor for TTV amongst all available *TESS* Sectors up to 67. TTVs are successfully identified for all targets known to be in multi-planet systems (see the example in Figure 3), while we have iden-

tified nine targets (see Table 4) currently thought to reside in single-planet systems that exhibit short-term variations. Figures 4, 5, and 6 are three planets in this sample, each showing visible sinusoidal distributions for their respective Sectors. Many of the targets orbit a low-mass star, which are commonly known to host multiple planets. These targets will require ground-based follow-up observations to confirm these variations, however if valid, they could be indicative of small planetary companions.

## 5. CONCLUSION

In this paper, we utilise photometry from *TESS* to refine the transit timing for 28 exoplanets from a sample of 50 targets that are to be observed throughout the exosolar survey for the *Twinkle Space Mission*. All targets improve on previous values with the exception of K2-141 c, K2-18 b, and K2-3 b. These three planets are instead constrained alongside the non-*TESS* target list of GJ 1214 b, HD 3167 c, WASP-74 b, and WASP-103 b, using a network of ground-based facilities available to the *Twinkle* ground-based working group. We have also detected nine single-planet systems exhibiting short-term transit timing variations. However, additional follow-up observations will be necessary to confirm if unseen planet companions are the source of these variations.

*Facilities:* TESS

*Software:* AstroImageJ (Collins et al. 2017), Astropy (Astropy Collaboration et al. 2013, 2018, 2022), batman (Kreidberg 2015), emcee (Foreman-Mackey et al. 2013), ExoTiC-LD (Grant & Wakeford 2022), Matplotlib (Hunter 2007), NumPy (Harris et al. 2020), wotan (Hippke et al. 2019)

## REFERENCES

- Asplund, M., Grevesse, N., Sauval, A. J., & Scott, P. 2009, *ARA&A*, 47, 481, doi: [10.1146/annurev.astro.46.060407.145222](https://doi.org/10.1146/annurev.astro.46.060407.145222)
- Astropy Collaboration, Robitaille, T. P., Tollerud, E. J., et al. 2013, *A&A*, 558, A33, doi: [10.1051/0004-6361/201322068](https://doi.org/10.1051/0004-6361/201322068)
- Astropy Collaboration, Price-Whelan, A. M., Sipőcz, B. M., et al. 2018, *AJ*, 156, 123, doi: [10.3847/1538-3881/aabc4f](https://doi.org/10.3847/1538-3881/aabc4f)
- Astropy Collaboration, Price-Whelan, A. M., Lim, P. L., et al. 2022, *ApJ*, 935, 167, doi: [10.3847/1538-4357/ac7c74](https://doi.org/10.3847/1538-4357/ac7c74)
- Collins, K. A., Kielkopf, J. F., Stassun, K. G., & Hessman, F. V. 2017, *AJ*, 153, 77, doi: [10.3847/1538-3881/153/2/77](https://doi.org/10.3847/1538-3881/153/2/77)
- Delrez, L., Ehrenreich, D., Alibert, Y., et al. 2021, *Nature Astronomy*, 5, 775, doi: [10.1038/s41550-021-01381-5](https://doi.org/10.1038/s41550-021-01381-5)
- Edwards, B., Rice, M., Zingales, T., et al. 2019, *Experimental Astronomy*, 47, 29, doi: [10.1007/s10686-018-9611-4](https://doi.org/10.1007/s10686-018-9611-4)
- Feinstein, A. D., David, T. J., Montet, B. T., et al. 2022, *ApJL*, 925, L2, doi: [10.3847/2041-8213/ac4745](https://doi.org/10.3847/2041-8213/ac4745)

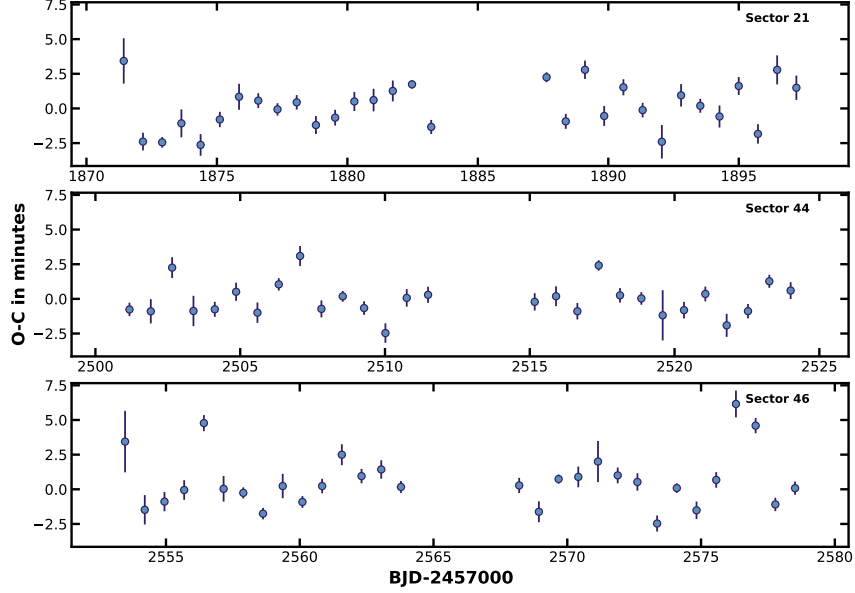


**Figure 3.** The transit timing variations for 55 Cnc e, for each available Sector observed with *TESS*. 55 Cnc e is known to be in a multi-planet system.

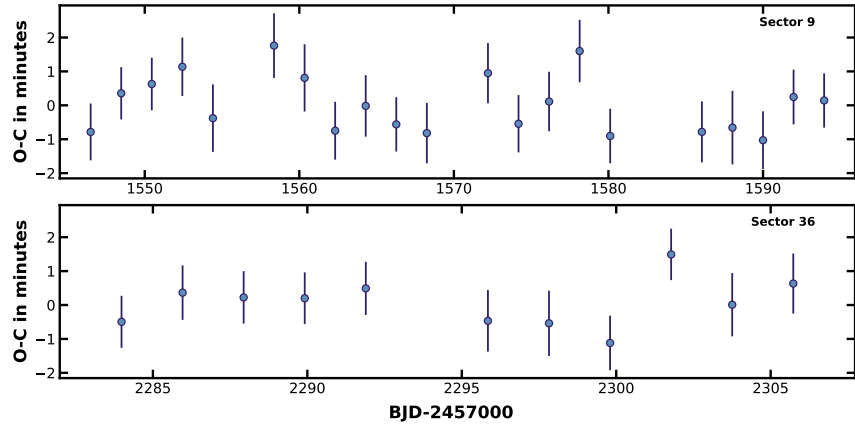


**Figure 4.** The transit timing variations for TOI-674 b, for Sector 9 and 36 observed with *TESS*. TOI-674 is currently classified as a single-planet system.

Foreman-Mackey, D., Hogg, D. W., Lang, D., & Goodman, J. 2013, *PASP*, 125, 306, doi: [10.1086/670067](https://doi.org/10.1086/670067)

Gardner, J. P., Mather, J. C., Clampin, M., et al. 2006, *SSRv*, 123, 485, doi: [10.1007/s11214-006-8315-7](https://doi.org/10.1007/s11214-006-8315-7)

Gilbert, E. A., Barclay, T., Quintana, E. V., et al. 2022, *AJ*, 163, 147, doi: [10.3847/1538-3881/ac23ca](https://doi.org/10.3847/1538-3881/ac23ca)

Grant, D., & Wakeford, H. R. 2022, *Exo-TiC/ExoTiC-LD: ExoTiC-LD v3.0.0*, v3.0.0, Zenodo, doi: [10.5281/zenodo.7437681](https://doi.org/10.5281/zenodo.7437681)

Harris, C. R., Millman, K. J., van der Walt, S. J., et al. 2020, *Nature*, 585, 357, doi: [10.1038/s41586-020-2649-2](https://doi.org/10.1038/s41586-020-2649-2)

Hipke, M., David, T. J., Mulders, G. D., & Heller, R. 2019, *AJ*, 158, 143, doi: [10.3847/1538-3881/ab3984](https://doi.org/10.3847/1538-3881/ab3984)

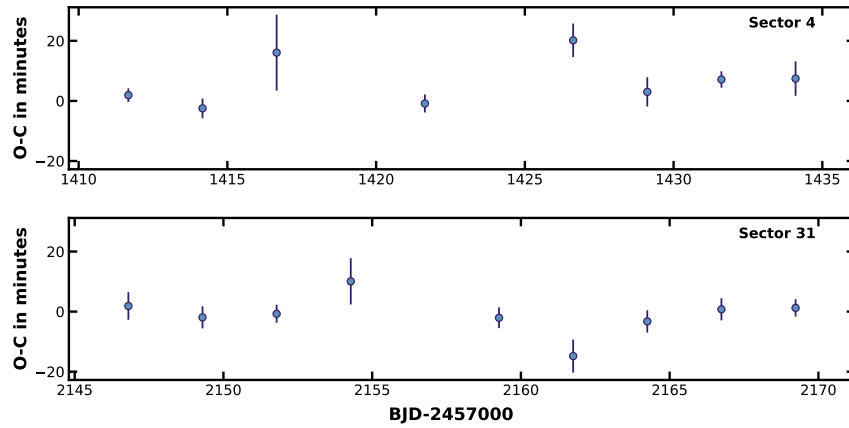


**Figure 5.** The transit timing variations for TOI-1201 b, for Sector 4 and 31 observed with *TESS*. Like in Figure 4, TOI-1201 b is currently classified as a single-planet system.

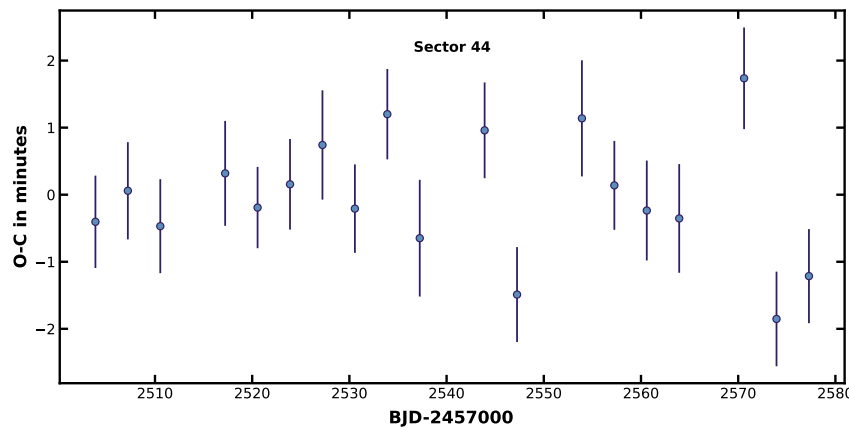


**Figure 6.** The transit timing variations for GJ 3470 b for Sector 44 observed with *TESS*. Like in Figure 4, GJ 3470 b is currently classified as a single-planet system.

Hunter, J. D. 2007, *Computing in Science & Engineering*, 9, 90, doi: [10.1109/MCSE.2007.55](https://doi.org/10.1109/MCSE.2007.55)

Ivshina, E. S., & Winn, J. N. 2022, *ApJS*, 259, 62, doi: [10.3847/1538-4365/ac545b](https://doi.org/10.3847/1538-4365/ac545b)

Jenkins, J. M., Twicken, J. D., McCauliff, S., et al. 2016, in *Proc. SPIE*, Vol. 9913, *Software and Cyberinfrastructure for Astronomy IV*, 99133E, doi: [10.1117/12.2233418](https://doi.org/10.1117/12.2233418)

Kokori, A., Tsiaras, A., Edwards, B., et al. 2023, *ApJS*, 265, 4, doi: [10.3847/1538-4365/ac9da4](https://doi.org/10.3847/1538-4365/ac9da4)

Kostogryz, N. M., Witzke, V., Shapiro, A. I., et al. 2022, *A&A*, 666, A60, doi: [10.1051/0004-6361/202243722](https://doi.org/10.1051/0004-6361/202243722)

Kreidberg, L. 2015, *PASP*, 127, 1161, doi: [10.1086/683602](https://doi.org/10.1086/683602)

Leleu, A., Alibert, Y., Hara, N. C., et al. 2021, *A&A*, 649, A26, doi: [10.1051/0004-6361/202039767](https://doi.org/10.1051/0004-6361/202039767)

Oddo, D., Dragomir, D., Brandeker, A., et al. 2023, *AJ*, 165, 134, doi: [10.3847/1538-3881/acb4e3](https://doi.org/10.3847/1538-3881/acb4e3)

Reefe, M. A., Luque, R., Gaidos, E., et al. 2022, *AJ*, 163, 269, doi: [10.3847/1538-3881/ac658b](https://doi.org/10.3847/1538-3881/ac658b)

Stotesbury, I., Edwards, B., Lavigne, J.-F., et al. 2022, in *Society of Photo-Optical Instrumentation Engineers (SPIE) Conference Series*, Vol. 12180, *Space Telescopes and Instrumentation 2022: Optical, Infrared, and Millimeter Wave*, ed. L. E. Coyle, S. Matsuura, & M. D. Perrin, 1218033, doi: [10.1117/12.2641373](https://doi.org/10.1117/12.2641373)

**Table 2.** The priors used for our targets.

System	$T_0$ (BJD)	P (days)	Source
55 Cnc e	$2459370.807543 \pm 0.000093$	$0.73654625 \pm 0.00000015$	Kokori et al. (2023)
GJ 436 b	$2455290.751684 \pm 0.00005$	$2.64389762 \pm 0.00000096$	Kokori et al. (2023)
HAT-P-12 b	$2456851.481119 \pm 0.00006$	$3.21305762 \pm 0.0000007$	Kokori et al. (2023)
HAT-P-26 b	$2456901.059458 \pm 0.000094$	$4.2345002 \pm 0.00000064$	Kokori et al. (2023)
HD 189733 b	$2456194.067619 \pm 0.000034$	$2.218574944 \pm 0.00000003$	Kokori et al. (2023)
HD 209458 b	$2455420.84456 \pm 0.00016$	$3.52474955 \pm 0.00000032$	Kokori et al. (2023)
HD 63433 b	$2459342.92881 \pm 0.00047$	$7.107939 \pm 0.000011$	Kokori et al. (2023)
HD 63433 c	$2459296.02303 \pm 0.00013$	$20.5438060 \pm 0.0000083$	Kokori et al. (2023)
HD 73583 b	$2459240.6702 \pm 0.0007$	$6.39805 \pm 0.00001$	Oddo et al. (2023)
HD 97658 b	$2457339.205224 \pm 0.000098$	$9.4893037 \pm 0.0000016$	Kokori et al. (2023)
KELT-20 b	$2459288.807775 \pm 0.000021$	$3.47410042 \pm 0.00000022$	Kokori et al. (2023)
TOI-1130 b	$2458866.6752 \pm 0.0013$	$4.077039 \pm 0.000026$	Kokori et al. (2023)
TOI-1130 c	$2458841.60130 \pm 0.00013$	$8.3498494 \pm 0.0000060$	Kokori et al. (2023)
TOI-178 d	$2458747.14623 \pm 0.00091$	$6.557700 \pm 0.000016$	Leleu et al. (2021)
TOI-620 b	$2458992.19724 \pm 0.00074$	$5.0988179 \pm 0.0000046$	Reefe et al. (2022)
TOI-776 b	$2458785.82769 \pm 0.00078$	$8.246630 \pm 0.000019$	Kokori et al. (2023)
TOI-776 c	$2459026.89405 \pm 0.00088$	$15.665340 \pm 0.000038$	Kokori et al. (2023)
WASP-11 b	$2456646.984352 \pm 0.000076$	$3.72247919 \pm 0.00000018$	Kokori et al. (2023)
WASP-39 b	$2456888.031364 \pm 0.00008$	$4.05528043 \pm 0.00000032$	Kokori et al. (2023)
WASP-69 b	$2457269.01322 \pm 0.00027$	$3.86813888 \pm 0.00000091$	Kokori et al. (2023)
WASP-80 b	$2456726.717483 \pm 0.000044$	$3.06785251 \pm 0.00000018$	Kokori et al. (2023)

Tinetti, G., Drossart, P., Eccleston, P., et al. 2018,  
Experimental Astronomy, 46, 135,  
doi: [10.1007/s10686-018-9598-x](https://doi.org/10.1007/s10686-018-9598-x)

Viani, L. S., Basu, S., Ong J., M. J., Bonaca, A., & Chaplin,  
W. J. 2018, ApJ, 858, 28, doi: [10.3847/1538-4357/aab7eb](https://doi.org/10.3847/1538-4357/aab7eb)  
Waalkes, W. C., Berta-Thompson, Z. K., Collins, K. A.,  
et al. 2021, AJ, 161, 13, doi: [10.3847/1538-3881/abc3b9](https://doi.org/10.3847/1538-3881/abc3b9)

**Table 3.** Ephemerides measurements for preliminary *Twinkle* targets

Planet	$T_0$ (BJD)	$P$ (days)	Source
55 Cnc e	2459370.807491 $\pm$ 0.00006	0.73654621 $\pm$ 0.00000014	This Work
AU Mic b	2458330.3908 <sup>+0.00058</sup> <sub>-0.00057</sub>	8.4630004 <sup>+0.000058</sup> <sub>-0.000060</sub>	Gilbert et al. (2022)
AU Mic c	2458342.2239 <sup>+0.0017</sup> <sub>-0.0019</sub>	18.858982 <sup>+0.000053</sup> <sub>-0.000050</sub>	Gilbert et al. (2022)
GJ 3470 b	2456974.689869 $\pm$ 0.000056	3.33665236 $\pm$ 0.00000011	This Work
GJ 436 b	2455290.751682 $\pm$ 0.00005	2.643897617 $\pm$ 0.00000005	This Work
GJ 9827 d	2457740.96120 $\pm$ 0.00040	6.2018089 $\pm$ 0.0000075	This Work
HAT-P-12 b	2456851.481139 $\pm$ 0.000056	3.21305773 $\pm$ 0.00000011	This Work
HAT-P-18 b	2457408.449133 $\pm$ 0.000081	5.50802941 $\pm$ 0.00000053	Kokori et al. (2023)
HAT-P-26 b	2456901.059482 $\pm$ 0.000091	4.23450085 $\pm$ 0.00000052	This Work
HATS-72 b	2458124.287570 $\pm$ 0.000045	7.3279496 $\pm$ 0.0000014	Kokori et al. (2023)
HD 136352 c	2458954.4099 <sup>+0.00052</sup> <sub>-0.00054</sub>	27.59221 $\pm$ 0.00011	Delrez et al. (2021)
HD 189733 b	2456194.067632 $\pm$ 0.000028	2.218574960 $\pm$ 0.000000017	This Work
HD 209458 b	2455420.84449 $\pm$ 0.00015	3.52474918 $\pm$ 0.00000012	This Work
HD 63433 b	2459342.92902 $\pm$ 0.00031	7.1079445 $\pm$ 0.0000092	This Work
HD 63433 c	2459342.92748 $\pm$ 0.00043	7.10792210 $\pm$ 0.0000095	This Work
HD 73583 b	2459240.67057 $\pm$ 0.00061	6.3980586 $\pm$ 0.0000058	This Work
HD 97658 b	2457339.205242 $\pm$ 0.000095	9.4893048 $\pm$ 0.0000011	This Work
K2-141 c	2457751.15462 $\pm$ 0.00051	7.74896 $\pm$ 0.0003	This Work
K2-18 b	2459537.2500 $\pm$ 0.0016	32.9380 $\pm$ 0.0022	This Work
K2-25 b	2457651.471616 $\pm$ 0.000062	3.48456248 $\pm$ 0.00000064	Kokori et al. (2023)
K2-3 b	2459528.1714 $\pm$ 0.0031	10.0537 $\pm$ 0.0023	This Work
K2-3 c	2457329.85688 $\pm$ 0.00052	24.6467384 $\pm$ 0.00004	This Work
K2-3 d	2457271.78798 $\pm$ 0.00075	44.556112 $\pm$ 0.000094	This Work
KELT-20 b	2459288.80779548 $\pm$ 0.000019	3.47410073 $\pm$ 0.00000017	This Work
LHS 1140 b	2458103.084207 $\pm$ 0.000043	24.737210 $\pm$ 0.000017	Kokori et al. (2023)
LP 714-47 b	2458774.70336 $\pm$ 0.00024	4.0520345 $\pm$ 0.0000026	Kokori et al. (2023)
LP 791-18 c	2458905.78256 $\pm$ 0.00020	4.9899054 $\pm$ 0.0000026	Kokori et al. (2023)
LTT 1445 Ab	2458905.71556 $\pm$ 0.00071	5.358777 $\pm$ 0.000011	Kokori et al. (2023)
LTT 3780 c	2458608.11003 $\pm$ 0.00045	12.252208 $\pm$ 0.000027	Kokori et al. (2023)
TOI-1130 b	2458866.67523 $\pm$ 0.0013	4.077039 $\pm$ 0.000025	This Work
TOI-1130 c	2458866.6752 $\pm$ 0.0013	4.077039 $\pm$ 0.000025	This Work
TOI-1201 b	2458822.84776 $\pm$ 0.00037	2.4919726 $\pm$ 0.0000024	Kokori et al. (2023)
TOI-178 d	2458747.14590 $\pm$ 0.00082	6.557694 $\pm$ 0.000015	This Work
TOI-237 b	2458697.7197997 <sup>+0.0007960</sup> <sub>-0.0008150</sub>	5.4360980.000039	Waalkes et al. (2021)
TOI-421 c	2458681.14621 $\pm$ 0.00059	16.067531 $\pm$ 0.000028	Kokori et al. (2023)
TOI-620 b	2458992.19622 $\pm$ 0.00051	5.0987929 $\pm$ 0.0000022	This Work
TOI-674 b	2458862.847755 $\pm$ 0.000088	1.97716420 $\pm$ 0.00000051	Kokori et al. (2023)
TOI-776 b	2458785.82746 $\pm$ 0.00076	8.2466106 $\pm$ 0.0000065	This Work
TOI-776 c	2458785.82779 $\pm$ 0.00078	8.246636 $\pm$ 0.000025	This Work
V1298 Tau b	2459481.09023 <sup>+0.00129</sup> <sub>-0.00132</sub>	24.1315 <sup>+0.0033</sup> <sub>-0.0034</sub>	Feinstein et al. (2022)
WASP-107 b	2457515.672118 $\pm$ 0.000075	5.72148926 $\pm$ 0.00000085	Kokori et al. (2023)
WASP-11 b	2456646.984401 $\pm$ 0.00007	3.72247944 $\pm$ 0.00000012	This Work
WASP-17 b	2457569.98347 $\pm$ 0.00012	3.73548545 $\pm$ 0.00000026	Kokori et al. (2023)
WASP-29 b	2457866.07613 $\pm$ 0.00011	3.92271183 $\pm$ 0.00000031	Kokori et al. (2023)
WASP-39 b	2456888.031327 $\pm$ 0.000076	4.05528002 $\pm$ 0.00000025	This Work
WASP-69 b	2457269.01313 $\pm$ 0.00025	3.86813822 $\pm$ 0.00000038	This Work
WASP-80 b	2456726.71745864 $\pm$ 0.000042	3.067852123 $\pm$ 0.000000068	This Work

**Table 4.** The *TESS* targets which display signs of transit timing variations.

<b>System</b>	<b>TIC</b>	<b><i>TESS</i> Magnitude</b>
GJ 3470 b	TIC19028197	10.2479 $\pm$ 0.007
HD 189733 b	TIC256364928	6.8481 $\pm$ 0.006
HD 209458 b	TIC420814525	7.1274 $\pm$ 0.006
HD 97658 b	TIC82308728	6.9859 $\pm$ 0.006
KELT-20 b	TIC69679391	7.5522 $\pm$ 0.006
TOI-1201 b	TIC29960110	10.9473 $\pm$ 0.007
TOI-674 b	TIC158588995	11.8764 $\pm$ 0.007
WASP-29 b	TIC183537452	10.2499 $\pm$ 0.006
WASP-69 b	TIC248853232	8.8628 $\pm$ 0.006

## 5.2 LINKS AND IMPLICATIONS

Please refer to Section 6.1.2 in Chapter 6 to understand how this paper has contributed towards the exoplanet community.

# CHAPTER 6: DISCUSSION AND CONCLUSIONS

## 6.1 DISCUSSION

### 6.1.1 PAPER-BY-PAPER ANALYSIS

In this work, we contribute towards characterising various exoplanets using ground and space-based facilities. We present the results through three original papers, with each focusing on a different analysis technique.

Lowson et al. (2023b) aimed to characterise the atmosphere of the ultra-hot Jupiter KELT-9b, using archival data observed from the high-resolution TRES instrument attached to the 1.5 reflector at the Fred Lawrence Whipple Observatory (FLWO). From the TRES observations, we were able to identify strong detections of H $\alpha$  ( $4\sigma$ ), Fe I ( $6\sigma$ ), Fe II ( $6\sigma$ ), and Mg I ( $4\sigma$ ) in the photosphere of KELT-9b using CCF maps. The atmospheric detection of KELT-9b additionally enabled us to constrain the mass values of  $M_\star = 1.91 \pm 0.68 M_\odot$  for KELT-9 and  $M_p = 2.31 \pm 0.89 M_J$  for KELT-9b, which is within a  $1\sigma$  agreement of previously published mass calculations for this system. We also present a toy model to describe the peculiar transit ‘W’-shaped transit observed in the H $\alpha$  band. H $\alpha$  is a known secondary tracer for atmosphere escape. The model accommodates for the ‘W’-shape by assuming an ellipsoidal

opaque tail of escaping material projecting towards the direction of the observer, however, the energy required to maintain the  $n = 2$  excitation rate for  $\text{H}\alpha$  beyond the exosphere of KELT-9b is a challenge. This work enabled us to successfully characterise an exoplanet through its atmosphere, with the detected species providing insight into the chemical dynamics of the planet and physical constraints on its true mass. For example, our ionised detections of Fe I and Fe II reiterate the large temperature values that have previously been evaluated for KELT-9b, given the large temperature required to ionise iron. Additionally, since  $\text{H}\alpha$  is a known secondary tracer for atmosphere escape, it's likely the atmosphere is undergoing evaporation.

In Lawson et al. (2023a), we identified and confirmed two exoplanet candidates using *TESS* and *CHEOPS*, orbiting the adolescent K-star HIP 113103, and by extension, constrain their orbital parameters. While the transits for HIP 113103 b and HIP 113103 c were initially detected using *TESS* Sector 1 and Sector 28, ground-based transit follow up through the TFOP network, improved photometric cadence using *CHEOPS*, and analysing the spectroscopic baseline of HIP 113103 were all additional observations required to confirm HIP 113103 b and HIP 113103 c as exoplanets. By combining these datasets and fitting them with a global model, HIP 113103 b and HIP 113103 c were classified to be short-period sub-Neptunes ( $P_b = 7.610303^{+0.000018}_{-0.000018}$  days,  $R_{p,b} = 1.829^{+0.096}_{-0.067} R_p$ ;  $P_c = 14.245648^{+0.000019}_{-0.000019}$  days,  $R_{p,c} = 2.40^{+0.10}_{-0.08} R_p$ ) with the inner planet residing in the sub-Neptune radius gap. Assuming that HIP 113103 b has a smaller atmosphere with a higher metallicity due to its radius compared to HIP 113103 c, we perform *JWST*, *HST*, and *Twinkle* atmospheric simulations of both planets to determine if a metallicity discrepancy could be recovered and thus provide insight into atmospheric mass loss

for HIP 113103 b. Our results indicate that a discrepancy would be difficult to recover due to the predicted large uncertainties associated with our simulations. This work enabled us to identify two new sub-Neptunes through a combination of ground and space-based facilities, primarily using photometric analysis.

In the final paper, Lawson et al. (prep), we aim to review the status and ephemerides of all targets currently planned for observation with the upcoming *Twinkle Space Mission*, for which UniSQ is a founding member. This was explored for the *Twinkle Space Mission* using the publicly available *TESS* photometry to update the ephemerides for various targets, while also monitoring for TTV signals. Our total sample included 50 targets with 46 of them already observed with *TESS*. We used the *TESS* data to improve the ephemerides for all our targets, including 28 targets that previously had their ephemerides constrained from *TESS* Sectors 1 to 44 through the ExoClock project. Our TTV analysis recovered known multi-planet systems while also identifying oscillations for targets currently classified as single-planet systems. The *Twinkle* targets not observed with *TESS* in conjunction with all long-period targets will be monitored with photometry from a global network of ground-based facilities accessible to the survey members. This work will enable optimal scheduling for the exosolar component of the *Twinkle* survey, maximising scientific output.

#### 6.1.2 SYNTHESIS, CONTRIBUTIONS, AND SIGNIFICANCE

Although the goals in each paper vary, they enable us to answer our candidature science case of how to characterise exoplanets using ground and space-based facilities. Additionally, all targets are observed using the primary transit

technique, but are explored with different instrumentation. This enables data analysis of exoplanets from both high-resolution spectroscopy and photometry. As outlined in Chapter 2, observing a planet-star interaction with different instrumentation reveals different properties, therefore expanding our overall understanding of exoplanet systems. While the exoplanets analysed vary in size, none reflect Solar System analogues, with all orbital periods closer to their host star than Mercury to our Sun. The short-period nature of these systems also result in strong planet-star orbital interactions, and throughout each paper we take advantage of these interactions to constrain numerous physical properties.

Each paper presented has made new contributions within the exoplanet community. The atmosphere detections of KELT-9b from FLWO's 1.5 m reflector remains the smallest telescope published to achieve such a feat. HRS CCF analysis is usually conducted on data gathered from large, costly ground-based observatories like the VLT, which are relatively scarce and subject to high demand, resulting in limited access and competition for observation time. By showcasing the feasibility of this technique with readily accessible meter-class facilities, particularly for ultra-hot Jupiters like KELT-9b, it holds the potential to expedite advancements within the field. The detection of H $\alpha$  from the 1.5 m reflector is also an important achievement, as it is a secondary tracer for atmosphere escape that is observable in the optical. Primary tracers such as Ly $\alpha$  (absorbing in the UV) and He I  $\lambda$ 10830 (absorbing in NIR) are only accessible to detect on limited facilities (with UV observations only achievable from space), which makes an optical detection of H $\alpha$  a valuable alternative to assist in identifying targets that may be experiencing atmosphere escape.

In Lawson et al. (2023a), we successfully observed two exoplanet candidates orbiting the adolescent K-star HIP 113103, representing the first identification and confirmation of exoplanets within this system. The discovery of exoplanets around bright, adolescent stars like HIP 113103 offers a unique opportunity to gain insights into the evolution of exoplanet atmospheres during their early stages, particularly for short-period planets. Notably, HIP 113103 b is situated within the sub-Neptune radius gap and is accompanied by HIP 113103 c, an outer planetary companion of a similar size. While it is unclear if HIP 113103 b has an atmosphere, its existence within the radius gap combined with the adolescent age of HIP 113103 makes this a valuable system for future *JWST* observations which could help provide insight on the atmosphere evolution of this sub-class.

The ephemerides refinement conducted in from Lawson et al. (prep) plays a pivotal role in our aim to maximise survey efficiency and mission planning for the *Twinkle Space Mission*. Such analysis is an ongoing necessity, as all exoplanetary systems are subject to long-term orbital decay, which can substantially impact the accuracy of predicted transit times. Additionally, our work includes TTV analysis, revealing short-term oscillations for some single-planet system targets. In the broader context of exoplanetary research, our work not only refines the orbital parameters crucial for mission planning but also underscores the dynamical complexity of exoplanetary systems. The identification of short-term TTV oscillations in single-planet systems reveal the potential existence of additional exoplanets, and if confirmed, would contribute towards expanding our catalog of multi-planet systems. This expansion could play a crucial role in advancing our understanding of orbital dynamics and diversity of exoplanetary architectures.

### 6.1.3 FUTURE DIRECTIONS

Each paper not only showcases our contributions towards the exoplanet community, but also serves as an opportunity for further in-depth analysis of the observed systems. We will be exploring the HIP 113103 system in greater detail beyond the scope of Lawson et al. (2023a), using awarded time with ESPRESSO on the VLT. These additional observations will be used to constrain the orbital obliquities of HIP 113103 b and HIP 113103 c, which will provide insight on the formation past of the HIP 113103 system. We will also use these observations to search for atmospheric signals. Ongoing work, as part of Lawson et al. (prep), includes observations for targets not observed with *TESS* using the ground-based network available to the *Twinkle* science team. We are also anticipating additional targets for ephemeris refinement and TTV monitoring, as the team is currently finalising additional priority targets for the exosolar component of the survey.

## 6.2 CONCLUSIONS

Throughout this candidature, we contribute towards characterising exoplanets using a diverse range of analysis techniques, both from ground and space-based facilities. Such techniques include, but were not limited to, atmosphere characterisation, atmospheric retrieval simulations, exoplanet confirmation, TTV analysis, and constraining orbital parameters from spectroscopic and/or photometric observations. Outcomes of this analysis confirm two sub-Neptunes around HIP 113103, detect the atmosphere of KELT-9b on the smallest metre-class telescope to date, and prepare exoplanet targets for exosolar survey of the forthcoming *Twinkle Space Mission*. These findings demonstrate that

we can retrieve a plethora of information about an exoplanet from primary transits, while also offering additional opportunities for further exploration within the broader exoplanet research community.

## REFERENCES

Note that the references presented here are for chapters 1, 2 and 6 and appendix A. References for the papers included in chapters 3 to 5 are included in the references sections of the papers.

Agol, E. & Fabrycky, D. C. (2018). Transit-Timing and Duration Variations for the Discovery and Characterization of Exoplanets. In H. J. Deeg & J. A. Belmonte (Eds.), *Handbook of Exoplanets* (pp.7).

Alonso, R. (2018). Characterization of Exoplanets: Secondary Eclipses. In H. J. Deeg & J. A. Belmonte (Eds.), *Handbook of Exoplanets* (pp.40).

Alvarez, P., Rodríguez Espinosa, J. M., & Sánchez, F. (1998). The Gran Telescopio Canarias (GTC) project. *New A Rev.*, 42(6-8), 553–556.

Bakos, G. Á. (2018). The HATNet and HATSouth Exoplanet Surveys. In H. J. Deeg & J. A. Belmonte (Eds.), *Handbook of Exoplanets* (pp. 111).

Bakos, G. Á., Noyes, R. W., Kovács, G., et al. (2007). HAT-P-1b: A Large-Radius, Low-Density Exoplanet Transiting One Member of a Stellar Binary. *The Astrophysical Journal*, 656(1), 552–559.

Barge, P., Baglin, A., Auvergne, M., et al. (2008). Transiting exoplanets from the CoRoT space mission. I. CoRoT-Exo-1b: a low-density short-period planet around a G0V star. *A&A*, 482(3), L17–L20.

Barman, T. S., Macintosh, B., Konopacky, Q. M., & Marois, C. (2011). Clouds and Chemistry in the Atmosphere of Extrasolar Planet HR8799b. *The Astrophysical Journal*, 733(1), 65.

- Becker, J. C., Vanderburg, A., Adams, F. C., et al. (2015). WASP-47: A Hot Jupiter System with Two Additional Planets Discovered by K2. *The Astrophysical Journal Letters*, 812(2), L18.
- Benz, W., Broeg, C., Fortier, A., et al. (2021). The CHEOPS mission. *Experimental Astronomy*, 51(1), 109–151.
- Biddle, L. I., Pearson, K. A., Crossfield, I. J. M., et al. (2014). Warm ice giant GJ 3470b - II. Revised planetary and stellar parameters from optical to near-infrared transit photometry. *Monthly Notices of the Royal Astronomical Society*, 443(2), 1810–1820.
- Birkby, J. L. (2018). Exoplanet Atmospheres at High Spectral Resolution. *arXiv e-prints*, (pp. arXiv:1806.04617).
- Boley, A. C., Granados Contreras, A. P., & Gladman, B. (2016). The In Situ Formation of Giant Planets at Short Orbital Periods. *The Astrophysical Journal Letters*, 817(2), L17.
- Borucki, W. J., Koch, D., Basri, G., et al. (2010). Kepler Planet-Detection Mission: Introduction and First Results. *Science*, 327(5968), 977.
- Bouchy, F., Pont, F., Santos, N. C., et al. (2004). Two new “very hot Jupiters” among the OGLE transiting candidates. *A&A*, 421, L13–L16.
- Bouchy, F., Udry, S., Mayor, M., et al. (2005). ELODIE metallicity-biased search for transiting Hot Jupiters. II. A very hot Jupiter transiting the bright K star HD 189733. *A&A*, 444(1), L15–L19.
- Bouma, L. G., Palumbo, E. K., & Hillenbrand, L. A. (2023). The Empirical Limits of Gyrochronology. *arXiv e-prints*, (pp. arXiv:2303.08830).
- Brogi, M., de Kok, R. J., Birkby, J. L., et al. (2014). Carbon monoxide and water vapor in the atmosphere of the non-transiting exoplanet HD 179949 b. *A&A*, 565, A124.

- Brogi, M., Line, M., Bean, J., et al. (2017). A Framework to Combine Low- and High-resolution Spectroscopy for the Atmospheres of Transiting Exoplanets. *The Astrophysical Journal Letters*, 839(1), 1–7.
- Brogi, M., Snellen, I. A. G., de Kok, R. J., et al. (2012). The signature of orbital motion from the dayside of the planet  $\tau$  Boötis b. *Nature*, 486(7404), 502–504.
- Bryant, E. M., Bayliss, D., & Van Eylen, V. (2023). The occurrence rate of giant planets orbiting low-mass stars with TESS. *Monthly Notices of the Royal Astronomical Society*, 521(3), 3663–3681.
- Butler, R. P., Marcy, G. W., Fischer, D. A., et al. (1999). Evidence for Multiple Companions to  $\nu$  Andromedae. *The Astrophysical Journal*, 526(2), 916–927.
- Butler, R. P., Vogt, S. S., Marcy, G. W., et al. (2004). A Neptune-Mass Planet Orbiting the Nearby M Dwarf GJ 436. *The Astrophysical Journal*, 617(1), 580–588.
- Catala, C. & Plato Team (2006). PLATO: Planetary Transits and Oscillations of Stars. In M. Fridlund, A. Baglin, J. Lochard, & L. Conroy (Eds.), *The CoRoT Mission Pre-Launch Status - Stellar Seismology and Planet Finding*, volume 1306 of *ESA Special Publication* (pp. 497–502).
- Charbonneau, D., Allen, L. E., Megeath, S. T., et al. (2005). Detection of Thermal Emission from an Extrasolar Planet. *The Astrophysical Journal*, 626(1), 523–529.
- Charbonneau, D., Brown, T. M., Latham, D. W., & Mayor, M. (2000). Detection of Planetary Transits Across a Sun-like Star. *The Astrophysical Journal Letters*, 529(1), L45–L48.
- Cheng, E. S., Hill, R. J., MacKenty, J. W., et al. (2000). Widefield camera 3 for the Hubble Space Telescope. In J. B. Breckinridge & P. Jakobsen (Eds.),

*UV, Optical, and IR Space Telescopes and Instruments*, volume 4013 of *Society of Photo-Optical Instrumentation Engineers (SPIE) Conference Series* (pp. 367–373).

Crossfield, I. J. M., Waalkes, W., Newton, E. R., et al. (2019). A Super-Earth and Sub-Neptune Transiting the Late-type M Dwarf LP 791-18. *The Astrophysical Journal Letters*, 883(1), L16.

Dawson, R. I. & Johnson, J. A. (2018). Origins of Hot Jupiters. *ARA&A*, 56, 175–221.

Deeg, H. J. & Alonso, R. (2018). Transit Photometry as an Exoplanet Discovery Method. In H. J. Deeg & J. A. Belmonte (Eds.), *Handbook of Exoplanets* (pp. 117).

Deleuil, M., Bonomo, A. S., Ferraz-Mello, S., et al. (2012). Transiting exoplanets from the CoRoT space mission. XX. CoRoT-20b: A very high density, high eccentricity transiting giant planet. *A&A*, 538, A145.

Deleuil, M. & Fridlund, M. (2018). CoRoT: The First Space-Based Transit Survey to Explore the Close-in Planet Population. In H. J. Deeg & J. A. Belmonte (Eds.), *Handbook of Exoplanets* (pp.79).

Delrez, L., Santerne, A., Almenara, J. M., et al. (2016). WASP-121 b: a hot Jupiter close to tidal disruption transiting an active F star. *Monthly Notices of the Royal Astronomical Society*, 458(4), 4025–4043.

Deming, D. & Knutson, H. A. (2020). Highlights of exoplanetary science from Spitzer. *Nature Astronomy*, 4, 453–466.

Deming, D., Louie, D., & Sheets, H. (2019). How to Characterize the Atmosphere of a Transiting Exoplanet. *PASP*, 131(995), 013001.

Deming, L. D. & Seager, S. (2017). Illusion and reality in the atmospheres of exoplanets. *Journal of Geophysical Research (Planets)*, 122(1), 53–75.

Díaz, M. R., Jenkins, J. S., Feng, F., et al. (2020). The Magellan/PFS Exoplanet Search: a 55-d period dense Neptune transiting the bright ( $V = 8.6$ )

- star HD 95338. *Monthly Notices of the Royal Astronomical Society*, 496(4), 4330–4341.
- Dittmann, J. A., Irwin, J. M., Charbonneau, D., et al. (2017). A temperate rocky super-Earth transiting a nearby cool star. *Nature*, 544(7650), 333–336.
- Fischer, D. A., Howard, A. W., Laughlin, G. P., et al. (2014). Exoplanet Detection Techniques. In H. Beuther, R. S. Klessen, C. P. Dullemond, & T. Henning (Eds.), *Protostars and Planets VI* (pp. 715).
- Fortney, J. J., Dawson, R. I., & Komacek, T. D. (2021). Hot Jupiters: Origins, Structure, Atmospheres. *Journal of Geophysical Research (Planets)*, 126(3), e06629.
- Fortney, J. J., Lodders, K., Marley, M. S., & Freedman, R. S. (2008). A Unified Theory for the Atmospheres of the Hot and Very Hot Jupiters: Two Classes of Irradiated Atmospheres. *The Astrophysical Journal*, 678(2), 1419–1435.
- Fressin, F., Torres, G., Charbonneau, D., et al. (2013). The False Positive Rate of Kepler and the Occurrence of Planets. *The Astrophysical Journal*, 766(2), 81.
- Fulton, B. J., Petigura, E. A., Howard, A. W., et al. (2017). The California-Kepler Survey. III. A Gap in the Radius Distribution of Small Planets. *Astronomical Journal*, 154(3), 109.
- Gan, T., Soubkiou, A., Wang, S. X., et al. (2022). TESS discovery of a sub-Neptune orbiting a mid-M dwarf TOI-2136. *Monthly Notices of the Royal Astronomical Society*, 514(3), 4120–4139.
- Gardner, J. P., Mather, J. C., Clampin, M., et al. (2006). The James Webb Space Telescope. *Space Sci. Rev.*, 123(4), 485–606.
- Gaudi, B. S., Seager, S., Mennesson, B., et al. (2020). The Habitable Exoplanet Observatory (HabEx) Mission Concept Study Final Report. *arXiv e-prints*, (pp. arXiv:2001.06683).

- Gibson, S. R., Howard, A. W., Marcy, G. W., et al. (2016). KPF: Keck Planet Finder. In C. J. Evans, L. Simard, & H. Takami (Eds.), *Ground-based and Airborne Instrumentation for Astronomy VI*, volume 9908 of *Society of Photo-Optical Instrumentation Engineers (SPIE) Conference Series* (pp. 990870).
- Gillon, M., Triaud, A. H. M. J., Demory, B.-O., et al. (2017). Seven temperate terrestrial planets around the nearby ultracool dwarf star TRAPPIST-1. *Nature*, 542(7642), 456–460.
- Ginzburg, S., Schlichting, H. E., & Sari, R. (2018). Core-powered mass-loss and the radius distribution of small exoplanets. *Monthly Notices of the Royal Astronomical Society*, 476(1), 759–765.
- Greene, T. P., Bell, T. J., Ducrot, E., et al. (2023). Thermal emission from the Earth-sized exoplanet TRAPPIST-1 b using JWST. *Nature*, 618(7963), 39–42.
- Günther, M. N., Pozuelos, F. J., Dittmann, J. A., et al. (2019). A super-Earth and two sub-Neptunes transiting the nearby and quiet M dwarf TOI-270. *Nature Astronomy*, 3, 1099–1108.
- Hellier, C., Anderson, D. R., Collier Cameron, A., et al. (2009). An orbital period of 0.94 days for the hot-Jupiter planet WASP-18b. *Nature*, 460(7259), 1098–1100.
- Hellier, C., Anderson, D. R., Collier Cameron, A., et al. (2011). WASP-43b: the closest-orbiting hot Jupiter. *A&A*, 535, L7.
- Henry, G. W., Marcy, G. W., Butler, R. P., & Vogt, S. S. (2000). A Transiting “51 Peg-like” Planet. *The Astrophysical Journal Letters*, 529(1), L41–L44.
- Holman, M. J. & Murray, N. W. (2005). The Use of Transit Timing to Detect Terrestrial-Mass Extrasolar Planets. *Science*, 307(5713), 1288–1291.
- Howard, A. W., Marcy, G. W., Bryson, S. T., et al. (2012). Planet Occurrence within 0.25 AU of Solar-type Stars from Kepler. *ApJS*, 201(2), 15.

- Howell, S. B., Sobeck, C., Haas, M., et al. (2014). The K2 Mission: Characterization and Early Results. *PASP*, 126(938), 398.
- Johnson, J. A., Aller, K. M., Howard, A. W., & Crepp, J. R. (2010). Giant Planet Occurrence in the Stellar Mass-Metallicity Plane. *PASP*, 122(894), 905.
- Johnson, J. A., Gazak, J. Z., Apps, K., et al. (2012). Characterizing the Cool KOIs. II. The M Dwarf KOI-254 and Its Hot Jupiter. *Astronomical Journal*, 143(5), 111.
- Kempton, E. M. R., Zhang, M., Bean, J. L., et al. (2023). A reflective, metal-rich atmosphere for GJ 1214b from its JWST phase curve. *Nature*, 620(7972), 67–71.
- Kite, E. S., Fegley, Bruce, J., Schaefer, L., & Ford, E. B. (2020). Atmosphere Origins for Exoplanet Sub-Neptunes. *The Astrophysical Journal*, 891(2), 111.
- Konopacky, Q. M., Barman, T. S., Macintosh, B. A., & Marois, C. (2013). Detection of Carbon Monoxide and Water Absorption Lines in an Exoplanet Atmosphere. *Science*, 339(6126), 1398–1401.
- Kunimoto, M. & Matthews, J. M. (2020). Searching the Entirety of Kepler Data. II. Occurrence Rate Estimates for FGK Stars. *Astronomical Journal*, 159(6), 248.
- Lin, D. N. C., Bodenheimer, P., & Richardson, D. C. (1996). Orbital migration of the planetary companion of  $\gamma$  1 Pegasi to its present location. *Nature*, 380(6575), 606–607.
- Lopez, E. D., Fortney, J. J., & Miller, N. (2012). How Thermal Evolution and Mass-loss Sculpt Populations of Super-Earths and Sub-Neptunes: Application to the Kepler-11 System and Beyond. *The Astrophysical Journal*, 761(1), 59.

- Lovis, C. & Fischer, D. (2010). Radial Velocity Techniques for Exoplanets. In S. Seager (Ed.), *Exoplanets* (pp. 27–53).
- Lowson, N., Wright, D. J., Huang, C. X., & Zhou, G. (in prep.). Ground-based preparation for the twinkle space mission.
- Lowson, N., Zhou, G., Huang, C. X., et al. (2023a). Two mini-Neptunes Transiting the Adolescent K-star HIP 113103 Confirmed with TESS and CHEOPS. *Monthly Notices of the Royal Astronomical Society*.
- Lowson, N., Zhou, G., Wright, D. J., et al. (2023b). Multiepoch Detections of the Extended Atmosphere and Transmission Spectra of KELT-9b with a 1.5 m Telescope. *Astronomical Journal*, 165(3), 101.
- Lustig-Yaeger, J., Fu, G., May, E. M., et al. (2023). A JWST transmission spectrum of the nearby Earth-sized exoplanet LHS 475 b. *Nature Astronomy*, 7, 1317–1328.
- Maciejewski, G., Dimitrov, D., Fernández, M., et al. (2016). Departure from the constant-period ephemeris for the transiting exoplanet WASP-12. *A&A*, 588, L6.
- Madhusudhan, N. (2019). Exoplanetary Atmospheres: Key Insights, Challenges, and Prospects. *ARA&A*, 57, 617–663.
- Madhusudhan, N., Sarkar, S., Constantinou, S., et al. (2023). Carbon-bearing Molecules in a Possible Hycean Atmosphere. *The Astrophysical Journal Letters*, 956(1), L13.
- Maxted, P. F. L., Anderson, D. R., Collier Cameron, A., et al. (2011). WASP-41b: A Transiting Hot Jupiter Planet Orbiting a Magnetically Active G8V Star. *PASP*, 123(903), 547.
- Mayor, M. & Queloz, D. (1995). A Jupiter-mass companion to a solar-type star. *Nature*, 378(6555), 355–359.

Mordasini, C., Alibert, Y., & Benz, W. (2009). Extrasolar planet population synthesis. I. Method, formation tracks, and mass-distance distribution. *A&A*, 501(3), 1139–1160.

Nascimbeni, V., Piotto, G., Bedin, L. R., & Damasso, M. (2011). TASTE: The Asiago Search for Transit timing variations of Exoplanets. I. Overview and improved parameters for HAT-P-3b and HAT-P-14b. *A&A*, 527, A85.

National Academies of Sciences, E. & Medicine (2023). *Pathways to Discovery in Astronomy and Astrophysics for the 2020s*. Washington, DC: The National Academies Press.

Nava, C., López-Morales, M., Mortier, A., et al. (2022). K2-79b and K2-222b: Mass Measurements of Two Small Exoplanets with Periods beyond 10 days that Overlap with Periodic Magnetic Activity Signals. *Astronomical Journal*, 163(2), 41.

Nikolov, N., Sing, D. K., Fortney, J. J., et al. (2018). An absolute sodium abundance for a cloud-free ‘hot Saturn’ exoplanet. *Nature*, 557(7706), 526–529.

Owen, J. E. & Jackson, A. P. (2012). Planetary evaporation by UV & X-ray radiation: basic hydrodynamics. *Monthly Notices of the Royal Astronomical Society*, 425(4), 2931–2947.

Pepe, F., Cristiani, S., Rebolo, R., et al. (2021). ESPRESSO at VLT. On-sky performance and first results. *A&A*, 645, A96.

Pepe, F., Lovis, C., Ségransan, D., et al. (2011). The HARPS search for Earth-like planets in the habitable zone. I. Very low-mass planets around <ASTROBJ>HD 20794</ASTROBJ>, <ASTROBJ>HD 85512</ASTROBJ>, and <ASTROBJ>HD 192310</ASTROBJ>. *A&A*, 534, A58.

Pepe, F., Mayor, M., Rupprecht, G., et al. (2002). HARPS: ESO’s coming planet searcher. Chasing exoplanets with the La Silla 3.6-m telescope. *The Messenger*, 110, 9–14.

- Pepper, J., Pogge, R. W., DePoy, D. L., et al. (2007). The Kilodegree Extremely Little Telescope (KELT): A Small Robotic Telescope for Large-Area Synoptic Surveys. *PASP*, 119(858), 923–935.
- Petigura, E. A., Marcy, G. W., Winn, J. N., et al. (2018). The California-Kepler Survey. IV. Metal-rich Stars Host a Greater Diversity of Planets. *Astronomical Journal*, 155(2), 89.
- Pollacco, D. L., Skillen, I., Collier Cameron, A., et al. (2006). The WASP Project and the SuperWASP Cameras. *PASP*, 118(848), 1407–1418.
- Queloz, D., Mayor, M., Weber, L., et al. (2000). The CORALIE survey for southern extra-solar planets. I. A planet orbiting the star Gliese 86. *A&A*, 354, 99–102.
- Rabus, M., Deeg, H. J., Alonso, R., et al. (2009). Transit timing analysis of the exoplanets TrES-1 and TrES-2. *A&A*, 508(2), 1011–1020.
- Redfield, S., Endl, M., Cochran, W. D., & Koesterke, L. (2008). Sodium Absorption from the Exoplanetary Atmosphere of HD 189733b Detected in the Optical Transmission Spectrum. *The Astrophysical Journal Letters*, 673(1), L87.
- Ricker, G. R., Winn, J. N., Vanderspek, R., et al. (2015). Transiting Exoplanet Survey Satellite (TESS). *Journal of Astronomical Telescopes, Instruments, and Systems*, 1, 1–10.
- Schwab, C., Rakich, A., Gong, Q., et al. (2016). Design of NEID, an extreme precision Doppler spectrograph for WIYN. In C. J. Evans, L. Simard, & H. Takami (Eds.), *Ground-based and Airborne Instrumentation for Astronomy VI*, volume 9908 of *Society of Photo-Optical Instrumentation Engineers (SPIE) Conference Series* (pp. 99087H).
- Seager, S. & Mallén-Ornelas, G. (2003). A Unique Solution of Planet and Star Parameters from an Extrasolar Planet Transit Light Curve. *The Astrophysical Journal*, 585(2), 1038–1055.

- Sedaghati, E., Boffin, H. M. J., MacDonald, R. J., et al. (2017). Detection of titanium oxide in the atmosphere of a hot Jupiter. *Nature*, 549(7671), 238–241.
- Snellen, I. A. G., Albrecht, S., de Mooij, E. J. W., & Le Poole, R. S. (2008). Ground-based detection of sodium in the transmission spectrum of exoplanet HD 209458b. *A&A*, 487(1), 357–362.
- Southworth, J., Dominik, M., Jørgensen, U. G., et al. (2011). A much lower density for the transiting extrasolar planet WASP-7. *A&A*, 527, A8.
- Tessenyi, M., Savini, G., Tinetti, G., et al. (2017). TWINKLE - A Low Earth Orbit Visible and Infrared Exoplanet Spectroscopy Observatory. In *Revista Mexicana de Astronomía y Astrofísica Conference Series*, volume 49 of *Revista Mexicana de Astronomía y Astrofísica Conference Series* (pp. 148–148).
- Tinetti, G., Drossart, P., Eccleston, P., et al. (2016). The science of ARIEL (Atmospheric Remote-sensing Infrared Exoplanet Large-survey). In Proc. SPIE, volume 9904 of *Society of Photo-Optical Instrumentation Engineers (SPIE) Conference Series* (pp. 1–10).
- Triaud, A. H. M. J. (2018). The Rossiter-McLaughlin Effect in Exoplanet Research. In H. J. Deeg & J. A. Belmonte (Eds.), *Handbook of Exoplanets* (pp.2).
- Trilling, D. E., Benz, W., Guillot, T., et al. (1998). Orbital Evolution and Migration of Giant Planets: Modeling Extrasolar Planets. *The Astrophysical Journal*, 500(1), 428–439.
- Tsai, S.-M., Lee, E. K. H., Powell, D., et al. (2023). Photochemically produced SO<sub>2</sub> in the atmosphere of WASP-39b. *Nature*, 617(7961), 483–487.
- van den Bergh, S. (1985). Astronomy with the Hubble space telescope. *JRASC*, 79, 134–142.
- Vidal-Madjar, A., Lecavelier des Etangs, A., Désert, J. M., et al. (2003). An extended upper atmosphere around the extrasolar planet HD209458b. *Nature*, 422(6928), 143–146.

- Vogt, S. S., Allen, S. L., Bigelow, B. C., et al. (1994). HIRES: the high-resolution echelle spectrometer on the Keck 10-m Telescope. In D. L. Crawford & E. R. Craine (Eds.), *Instrumentation in Astronomy VIII*, volume 2198 of *Society of Photo-Optical Instrumentation Engineers (SPIE) Conference Series* (pp. 362).
- Wiedemann, G. (1996). Science with the VLT: high-resolution infrared spectroscopy. *The Messenger*, 86, 24–30.
- Wiedemann, G. R. (1998). CRIRES: cryogenic high-resolution infrared echelle spectrograph for the VLT. In A. M. Fowler (Ed.), *Infrared Astronomical Instrumentation*, volume 3354 of *Society of Photo-Optical Instrumentation Engineers (SPIE) Conference Series* (pp. 599–605).
- Wilson, D. M., Gillon, M., Hellier, C., et al. (2008). WASP-4b: A 12th Magnitude Transiting Hot Jupiter in the Southern Hemisphere. *The Astrophysical Journal Letters*, 675(2), L113.
- Winn, J. N. & Fabrycky, D. C. (2015). The Occurrence and Architecture of Exoplanetary Systems. *ARA&A*, 53, 409–447.
- Wu, Y. & Murray, N. (2003). Planet Migration and Binary Companions: The Case of HD 80606b. *The Astrophysical Journal*, 589(1), 605–614.
- Wytttenbach, A., Ehrenreich, D., Lovis, C., et al. (2015). Spectrally resolved detection of sodium in the atmosphere of HD 189733b with the HARPS spectrograph. *A&A*, 577, A62.
- Zhao, L. L., Fischer, D. A., Ford, E. B., et al. (2022). The EXPRES Stellar Signals Project II. State of the Field in Disentangling Photospheric Velocities. *Astronomical Journal*, 163(4), 171.
- Zieba, S., Kreidberg, L., Ducrot, E., et al. (2023). No thick carbon dioxide atmosphere on the rocky exoplanet TRAPPIST-1 c. *Nature*, 620(7975), 746–749.

# APPENDIX A: OTHER PUBLISHED WORKS.

In addition to the three publications presented in Chapters 3, 4, and 5, I have also contributed towards additional publications via co-authorship in the areas of exoplanetary science and inclusively. The title, authorship, and abstract of these works are presented below.

## A.1 EVIDENCE FOR LOW-LEVEL DYNAMICAL EXCITATION IN NEAR-RESONANT EXOPLANET SYSTEMS

M. Rice, X. Wang, S. Wang, A. Shporer, K. Barkaoui, R. Brahm, K. Collins, A. Jordán, N. Lawson, R. P. Butler, J. D. Crane, S. Shectman, J. Teske, and I. Thompson 2023. **Evidence for Low-Level Dynamical Excitation in Near-Resonant Exoplanet Systems.** Submitted for publication in *Astronomical Journal*, *The geometries of near-resonant planetary systems offer a relatively pristine window into the initial conditions of exoplanet systems. Given that near-resonant systems have likely experienced minimal dynamical disruptions, the spin-orbit orientations of these systems inform the typical outcomes of quiescent planet formation, as well as the primordial stellar obliquity distribution. However, few measurements have been made to constrain the spin-orbit ori-*

entations of near-resonant systems. We present a Rossiter-McLaughlin measurement of the near-resonant TOI-2202 b warm Jupiter, obtained using the Carnegie Planet Finder Spectrograph (PFS) on the 6.5m Magellan Clay Telescope. This is the eighth result from the Stellar Obliquities in Long-period Exoplanet Systems (SOLES) survey. We derive a sky-projected 2D spin-orbit angle  $\lambda = 26^{+12}_{-15}^\circ$  and a 3D spin-orbit angle  $\psi = 31^{+13}_{-11}^\circ$  finding that TOI-2202 b is the most highly misaligned near-resonant Jovian exoplanet with a 3D spin-orbit constraint to date. Incorporating the full census of spin-orbit measurements for near-resonant systems, we demonstrate that the current census of near-resonant systems with period ratios  $P_2/P_1 \leq 4$  is generally consistent with a quiescent formation pathway, with some room for low-level ( $\lesssim 20^\circ$ ) primordial protoplanetary disk misalignments or post-disk spin-orbit excitation. Our result constitutes the first population-wide analysis of spin-orbit geometries for near-resonant planetary systems.

## A.2 CHARACTERISING A WORLD WITHIN THE HOT NEPTUNE DESERT: TRANSIT OBSERVATIONS OF LTT 9779 B WITH *HST* WFC3

B. Edwards, Q. Changeat, A. Tsiaras, A. Allan, P. Behr, S. R. Hagey, M. D. Himes, S. Ma, K. G. Stassun, L. Thomas, A. Thompson, A. Boley, L. Booth, J. Bouwman, K. France, N. Lawson, A. Meech, C. L. Phillips, A. A. Vidotto, K. Hou Yip, M. Bieger, A. Gressier, E. Janin, I. Jiang, P. Leonardi, S. Sarkar, N. Skaf, J. Taylor, M. Yang, and D. Ward-Thompson 2023. **Characterising a World Within the Hot Neptune Desert: Transit Observations of LTT 9779 b with *HST* WFC3.** *Astronomical Journal* 166(4), *We present*

*an atmospheric analysis of LTT 9779 b, a rare planet situated in the hot Neptune desert, that has been observed with HST WFC3 G102 and G141. The combined transmission spectrum, which covers 0.8 – 1.6  $\mu\text{m}$ , shows a gradual increase in transit depth with wavelength. Our preferred atmospheric model shows evidence for  $\text{H}_2\text{O}$ ,  $\text{CO}_2$  and FeH with a significance of  $3.1\sigma$ ,  $2.4\sigma$  and  $2.1\sigma$ , respectively. In an attempt to constrain the rate of atmospheric escape for this planet, we search for the 1.083  $\mu\text{m}$  Helium line in the G102 data but find no evidence of excess absorption that would indicate an escaping atmosphere using this tracer. We refine the orbital ephemerides of LTT 9779 b using our HST data and observations from TESS, searching for evidence of orbital decay or apsidal precession, which is not found. The phase-curve observation of LTT 9779 b with JWST NIRISS should provide deeper insights into the atmosphere of this planet and the expected atmospheric escape might be detected with further observations concentrated on other tracers such as Lyman- $\alpha$ .*

### A.3 INVISIBLE WOMEN: GENDER REPRESENTATION IN HIGH SCHOOL SCIENCE COURSES ACROSS AUSTRALIA

K. Ross, S. Galaudage, T. Clark, N. Lowson, A. Battisti, H. Adam, A. K. Ross, and N. Sweaney 2023. **Invisible Women: Gender Representation in High School Science Courses Across Australia.** SAGE Australian Journal of Education, *The visibility of female role models in science is vital for engaging and retaining women in scientific fields. In this study we analyse four senior secondary science courses delivered across the states and territories in Australia: Biology, Chemistry, Environmental Science, and Physics. We compared male and female representation within the science courses by examining the mentions of male and female scientists along with the context of their inclusions in the syl-*

*labuses. We find a clear gender bias with only one unique mention of a female scientist. We also find a clear Eurocentric focus and narrow representation of scientists. This bias will contribute to the continuing low engagement of women in scientific fields. We outline possible solutions to address this issue, including the accreditation of scientific discoveries to include female scientists and explicit discussion of structural barriers preventing the participation and progression of women in STEM.*

#### A.4 A MINI-NEPTUNE FROM *TESS* AND *CHEOPS* AROUND THE 120 MYR OLD AB DOR MEMBER HIP 94235

G. Zhou, C. P. Wirth, C. X. Huang, A. Venner, K. Franson, S. N. Quinn, L. G. Bouma, A. L. Kraus, A. W. Mann, E. R. Newton, D. Dragomir, A. Heitzmann, N. Lawson, S. T. Douglas, M. Battley, E. Gillen, A. Triaud, D. W. Latham, S. B. Howell, J. D. Hartman, B. M. Tofflemire, R. A. Wittenmyer, B. P. Bowler, J. Horner, S. R. Kane, J. Kielkopf, P. Plavchan, D. J. Wright, B. C. Addison, M. W. Mengel, J. Okumura, G. Ricker, R. Vanderspek, S. Seager, J. M. Jenkins, J. N. Winn, T. Daylan, M. Fausnaugh, and M. Kunimoto 2022. **A Mini-Neptune from *TESS* and *CHEOPS* Around the 120 Myr Old AB Dor member HIP 94235.** *Astronomical Journal* 163(6), *The Transiting Exoplanet Survey Satellite (TESS) mission has enabled discoveries of the brightest transiting planet systems around young stars. These systems are the benchmarks for testing theories of planetary evolution. We report the discovery of a mini-Neptune transiting a bright star in the AB Doradus moving group. HIP 94235 (TOI-4399, TIC 464646604) is a  $V_{mag} = 8.31$  G-dwarf hosting a  $3.00^{+0.32}_{-0.28} R_{\oplus}$  mini-Neptune in a 7.7 day period orbit. HIP 94235 is part of the AB Doradus moving group, one of the youngest and closest associations. Due to*

*its youth, the host star exhibits significant photometric spot modulation, lithium absorption, and X-ray emission. Three 0.06% transits were observed during Sector 27 of the TESS Extended Mission, though these transit signals are dwarfed by the 2% peak-to-peak photometric variability exhibited by the host star. Follow-up observations with the Characterising Exoplanet Satellite confirmed the transit signal and prevented the erosion of the transit ephemeris. HIP 94235 is part of a 50 au G-M binary system. We make use of diffraction limited observations spanning 11 yr, and astrometric accelerations from Hipparcos and Gaia, to constrain the orbit of HIP 94235 B. HIP 94235 is one of the tightest stellar binaries to host an inner planet. As part of a growing sample of bright, young planet systems, HIP 94235 b is ideal for follow-up transit observations, such as those that investigate the evaporative processes driven by high-energy radiation that may sculpt the valleys and deserts in the Neptune population.*

## A.5 TWINKLE: A SMALL SATELLITE SPECTROSCOPY MISSION FOR THE NEXT PHASE OF EXOPLANET SCIENCE

I. Stotesbury, B. Edwards, J. Lavigne, V. Pesquita, J. J. Veilleux, P. Windred, A. Al-Refaie, L. Bradley, S. Ma, G. Savini, G. Tinetti, T. Birnstiel, S. Dodson-Robinson, B. Ercolano, D. Feliz, S. Gaudi, N. Hernitschek, D. Holdsworth, I. Jiang, M. Griffin, N. Lawson, K. Molaverdikhani, H. Neilson, C. Phillips, T. Preibisch, S. Sarkar, K. G. Stassun, D. Ward-Thompson, D. Wright, M. Yang, L. Yeh, J. Zhou, R. Archer, Y. Barrathwaj Raman Mohan, M. Joshua, M. Tessenyi, J. Tennyson, and B. Wilcock 2022. **Twinkle: a small satellite spectroscopy mission for the next phase of exoplanet science.** SPIE 12180 (1218033), *With a focus on off-the-shelf components, Twinkle is the first in a series of cost competitive small satellites managed and financed by Blue Skies*

*Space Ltd. The satellite is based on a high-heritage Airbus platform that will carry a 0.45 m telescope and a spectrometer which will provide simultaneous wavelength coverage from 0.5 – 4.5  $\mu$ m. The spacecraft prime is Airbus Stevenage while the telescope is being developed by Airbus Toulouse and the spectrometer by ABB Canada. Scheduled to begin scientific operations in 2025, Twinkle will sit in a thermally-stable, sun-synchronous, low-Earth orbit. The mission has a designed operation lifetime of at least seven years and, during the first three years of operation, will conduct two large-scale survey programmes: one focused on Solar System objects and the other dedicated to extrasolar targets. Here we present an overview of the architecture of the mission, refinements in the design approach, and some of the key science themes of the extrasolar survey.*

## A.6 AROUND THE HYBRID CONFERENCE WORLD IN THE COVID-19 ERA

V. A. Moss, L. Balaguer-Nuñez, K. Bolejko, L. Burtscher, A. Carr, E. M. Di Teodoro, B. Gregory, E. Hanko, A. S. Hill, A. Hughes, L. Kaper, E. F. Kerri-son, F. J. Lockman, N. Lowson, and A. R. H. Stevens, 2022. **Around the hybrid conference world in the COVID-19 era.** *Nature Astronomy* 6(1105-1109), *In-person and online conferences each have their benefits, with hybrid conferences intended to blend the best of both worlds. But do hybrid conferences fulfil the promise? Fifteen attendees across three global conferences share their collective experiences.*

## A.7 TOI-1842B: A TRANSITING WARM SATURN UNDERGOING RE-INFLATION AROUND AN EVOLVING SUBGIANT

R. A. Wittenmyer, J. T. Clark, T. Trifonov, B. C. Addison, D. J. Wright, K. G. Stassun, J. Horner, N. Lawson, J. Kielkopf, S. R. Kane, P. Plavchan, A. Shporer, H. Zhang, B. P. Bowler, M. W. Mengel, J. Okumura, M. Rabus, M. C. Johnson, D. Harbeck, R. Tronsgaard, L. A. Buchhave, K. A. Collins, K. I. Collins, T. Gan, E. L. N. Jensen, S. B. Howell, E. Furlan, C. L. Gnilka, K. V. Lester, R. A. Matson, N. J. Scott, G. R. Ricker, R. Vanderspek, D. W. Latham, S. Seager, J. N. Winn, J. M. Jenkins, A. Rudat, E. V. Quintana, D. R. Rodriguez, D. A. Caldwell, S. N. Quinn, Z. Essack, and L. G. Bouma, 2022. **TOI-1842b: A Transiting Warm Saturn Undergoing Re-Inflation around an Evolving Subgiant.** *Astronomical Journal* 163(2), *The imminent launch of space telescopes designed to probe the atmospheres of exoplanets has prompted new efforts to prioritize the thousands of transiting planet candidates for follow-up characterization. We report the detection and confirmation of TOI-1842b, a warm Saturn identified by TESS and confirmed with ground-based observations from MINERVA-Australis, NRES, and the Las Cumbres Observatory Global Telescope. This planet has a radius of  $1.04_{0.05}^{+0.06} R_J$ , a mass of  $0.214_{0.038}^{+0.040} M_J$ , an orbital period of  $9.5739_{0.0001}^{+0.0002}$  days, and an extremely low density ( $\rho = 0.252 \pm 0.091 \text{ g cm}^{-3}$ ). TOI-1842b has among the best known combinations of large atmospheric scale height (893 km) and host-star brightness ( $J = 8.747 \text{ mag}$ ), making it an attractive target for atmospheric characterization. As the host star is beginning to evolve off the main sequence, TOI-1842b presents an excellent opportunity to test models of gas giant reinflation. The primary transit duration of only 4.3 hr also makes TOI-1842b an easily-schedulable tar-*

*get for further ground-based atmospheric characterization.*

This page intentionally left blank.